Pairing correlations in 206Pb+ 118Sn transfer reactions

Diklić, Josipa

University of Zagreb

FACULTY OF SCIENCE

Josipa Diklić

Pairing correlations in ^{206}Pb+ ^{118}Sn transfer reactions

DOCTORAL DISSERTATION

Zagreb, 2023

Sveučilište u Zagrebu

PRIRODOSLOVNO-MATEMATIČKI FAKULTET

Josipa Diklić

Korelacije sparivanja nukleona u reakcijama prijenosa ^{206}Pb+ ^{118}Sn

DOKTORSKI RAD

Mentor: Dr. sc. Suzana Szilner

Zagreb, 2023

"You know, sometimes to get perspective, I like to think about a spaceman on a star, incredibly far away. And our problems don't matter to him because we're just a distant point of light."

Michael Scott (The Office)

Supervisor

Dr. Suzana Szilner obtained B. Sc. and M. Sc. degree at the University of Zagreb, and the PhD thesis in double-supervised thesis by University L. Pasteur in Strasbourg and University of Zagreb. She was postdoctoral fellow at the Laboratori Nazionali di Legnaro. She was employed at Ruđer Bošković Institute, Zagreb, as research associate in 2003. She is senior scientist since 2014, tenured senior scientist since 2018, and head of the Nuclear physics laboratory since 2016. Dr. Szilner was the principal investigator of several Croatian Science Foundation or Ministry of Science and Education projects. She participated, as collaborator, or as the member of the Project Management Board or as the work-package leader, in several European projects (within FP7 and HORIZON2020). She is included in the activities of the Croatian scientific center of excellence for Advanced Materials and Sensors.

Dr. Szilner participated in different management and organizational activities at her home institution (member of the Board of governors, member of Scientific Council). She also participated in the organizational and scientific activities at EU (Scientific Steering Committee of the European Nuclear Science and Applications Research within ENSAR2 project, the Long Range Plan of the Nuclear Physics European Collaboration Committee). She was co-chair of several international conferences, and started the successful series of Nuclear Structure and Dynamics conferences.

Dr. Szilner participated to more than 70 nuclear physics experiments at different accelerator facilities in Europe, where she was a spokesperson of more than 15 experimental research projects. These research activities, according to Web of Science Core Collection, resulted in 261 publications, 4970 citations, h-index = 42, with several letters and one high cited topical review.

University of Zagreb
Faculty of Science
Department of Physics

Doctoral Thesis

Pairing correlations in ^{206}Pb+ ^{118}Sn transfer reactions

Josipa Diklić
Ruđer Bošković Institute, Zagreb

The ^{206}Pb+ ^{118}Sn reaction was measured by employing the new generation spectrometer PRISMA which makes it possible to measure the heavy-ion transfer reaction with high efficiency and good ion identification even at very low bombing energies. The measurements have been performed at the INFN-LNL accelerator complex, by using the heavy ^{206}Pb ion beam, at three different bombarding energies and by detecting the lighter reaction fragments in PRISMA at different angles and magnetic settings.

The most important results of this experiment can be categorized into two main groups. The study of the dynamics, where at the highest measured energy the transition from quasi-elastic to deep inelastic regimes was followed. The second group of results concerns the search for the signatures of the nucleon-nucleon correlations.

The dynamics was studied through the behavior of the differential and total cross sections, the energy distributions for different transfer channels, and their comparison with the theoretical calculations. In particular, from the dependence of the Q-value distributions on the scattering angle, the evolution from the quasi-elastic to the deep inelastic regime was evidenced.

Nucleon-nucleon correlations were studied by the construction of the transfer probabilities as a function of the distances of the closest approach. The probabilities of different one-nucleon transfer channels have been compared with those of the two-nucleon transfers. By comparing their absolute values the enhancement factors have been extracted. The results were also compared with the GRAZING code calculations.

(143 pages, 98 references, 65 figures, 28 tables, original in English)

Keywords: the ^{206}Pb+ ^{118}Sn system, heavy-ion collisions, multinucleon transfer reactions, magnetic spectrometer, nucleon-nucleon correlations, differential and total cross sections

Supervisor: Dr. sc. Suzana Szilner, Ruđer Bošković Institute, Zagreb

Reviewers:
1. Prof. dr. sc. Matko Milin, University of Zagreb
2. Prof. dr. sc. Tamara Nikšić, University of Zagreb
3. Dr. sc. Suzana Szilner, Ruđer Bošković Institute, Zagreb

Thesis accepted: 2023

Prošireni sažetak

Reakcije koje proučavamo u ovom doktoratu nazivaju se reakcijama prijenosa mnogo nukleona (MNT). One uključujući razmjenu jednog, dva ili više nukleona između jezgre projektila i jezgre mete. MNT reakcije nalaze se između kvazi-elastičnog i duboko neelastičnog režima, u smislu trajanja reakcije, gubitka kinetičke energije i broja razmijenjenih čestica. Ovakve reakcije posebno su zanimljive iz dva razloga. Prvi razlog je zato što ove reakcije pružaju uvid u dinamiku same reakcije i kako se ona razvija od kvazi-elastičnog do duboko neelastičnog režima. Drugi razlog je mogućnost istovremenog promatranja raznih kanala prijenosa nukleona, što nam daje mogućnost proučavanja korelacije među nukleonima. Upravo su za te dvije teme vezani i glavni rezultati ovog doktorata.

Sustav koji je promatran u ovom doktoratu je ^{206}Pb+^{118}Sn. Takav sustav ima otvorene kanale ogoljavanja i pobiranja neutrona, kao i ogoljavanja i pobiranje protona s dodatnim prijenosima neutrona na višim energijama. Zbog toga je dobar kandidat za proučavanje kako dinamike reakcije tako i korelacija među nukleonima. Za identifikaciju produkata reakcije korišten je magnetski spektrometar PRISMA na postrojenju INFN-LNL u Italiji. PRISMA je namještena da detektira lakše partnere u reakciji (produkte reakcije sličnih meti). Eksperiment je rađen na tri energije snopa (E_{lab} = 1200 MeV, 1090 MeV i 1035 MeV), od iznad barijere do ispod nje, a PRISMA je postavljen na dva različita kuta detekcije ($\theta_{lab} = 35°$ i 25°) kako bi se proučavale široke kutne raspodjele. Sama PRISMA ima kutnu prihvatljivost od oko 10°, što nam je omogućilo da na energiji poviše barijere (1200 MeV) promatramo razvoj reakcije na širokom rasponu kuteva od 20°. Tri različite energije snopa, a posebno najniža energija omogućili su nam da promatramo korelacije među neutronima. Kako bi se osigurala dobra razlučivost lakih produkata reakcije (produkti reakcije slični meti) koje ulaze u PRISMA korištena je inverzna kinematička konfiguracija, u kojoj je korišten teški snop ^{206}Pb na metu ^{118}Sn. Sama kinematika reakcije

te odabrani postav PRISMA-e omogućili su ulazak i teških partnera reakcije (produkti reakcije slični snopu) što je omogućilo dodatnu kontrolu uvjeta. Za normalizaciju intenziteta snopa koristili su se silicijski monitor detektori, koji su detektirali samo elastično raspršenje.

Prvi korak u analizi je bila kalibracija svih detektora, čime se omogućilo dobivanje fizikalnih veličina. Identifikaciju događaja postižemo rekonstrukcijom putanja koristeći jednadžbe gibanja iona u magnetskim elementima te mjerene parametre poput ulaznih položaja, položaja na fokalnoj ravnini, vremena proleta, gubitka energije i ukupne kinetičke energije. Rezultati rekonstrukcije uključuju polumjer zakrivljenosti unutar dipola, ukupnu duljinu puta, energiju oslobođenu u ionizacijskoj komori i domet iona unutar nje. Atomski broj (Z) dobivamo mjerenjem gubitka energije ili dometa iona u ionizacijskoj komori, te ukupne energije. Najintenzivnija raspodjela događaja pripada izotopima kositra, pri čemu je ^{118}Sn najprisutniji, a ostale linije identificiramo s pomoću Bethe-Bloch formule. Konačna rezolucija atomskog broja s je $\sim 1/68$. Za svaki element potrebno je identificirati nabojna stanja, što činimo koristeći ($\rho\beta - E$) matricu, gdje vrijedi sljedeća ovisnost ($E \sim qB\rho v$). Nakon toga, maseni brojevi se dobiju množenjem A/q vrijednosti s identificiranim q. Konstruirani su maseni spektri od nekoliko protonski kanala, točnije od (+2p) do (-3p) za najvišu energiju snopa (1200 MeV), od (+2p) do (-2p) za srednju energiju (1090 MeV) te samo neutronski kanali (0p) za najnižu energiju (1035 MeV). Postignuta je jako dobra masena rezolucija od $\sim 1/210$.

Nakon što smo identificirali sve kanale prijenosa, na najvišoj energiji snopa, promatrali smo evoluciju reakcije svakog od njih. Kako bi vizualizirali evoluciju MNT reakcija, rađeni su Wilczynski dijagrami, koji prikazuju odnos između Q-vrijednosti ili ukupnog gubitka kinetičke energije i kuta raspršenja. U svim promatranim kanalima uočeni su događaji s velikim gubitcima energije. Takvi događaji se na višim kutevima, u sustavu centra mase (stražnji kutevi), pomiču prema višim gubicima energije. To jest, uočeno je da je područje koje odgovara Q-vrijednosti za prijelaz iz osnovnog u osnovno stanje (Q_0) sve manje popunjeno kako se pomičemo prema stražnjim kutevima. Promatranjem projekcije na Q-vrijednost vidimo da se vrh distribucije za neutronske kanale nalazi na (Q_0), dok je za protonske, posebno za ogoljavanje protona te pobiranje dva protona s dodatnim prijenosima neutrona, distribucija pomiče prema višim gubicima energije. Osim evolucije dinamike, u reakciji ^{206}Pb+^{118}Sn, dobiveni su i podaci o diferencijalnim (DCS) te ukupnim

udarnim presjecima (TCS) za različite reakcijske kanale. Odgovarajući udarni presjeci uspoređeni su s teorijskim izračunima provedenim s pomoću GRAZING koda. Utvrđeno je općenito dobro slaganje za kanale prijenosa neutrona, kao i za kanale ogoljavanje jednog i dva te pobiranje jednog protona. Teorija daje manje vrijednosti nego podaci u kanalima koji uključuju prijenos mnogo nukleona, što ukazuje na to da su uključeni složeniji procesi za dane izotope.

Korelacije među nukleonima proučavane su iz ovisnosti vjerojatnosti prijenosa nukleona kao funkcije udaljenosti najbližeg pristupa. Vjerojatnost prijenosa nukleona definirana je kao omjer udarnog prijesjeka u određenom kanalu prijenosa te udarnog presjeka u elastičnom+ neelastičnom kanalu. Za neutronske kanale koristili smo dio raspodjele koji odgovara elastičnom dijelu Q-vrijednosti. Za protonske kanale integrirali smo cijelu raspodjelu Q-vrijednosti. Integracija se radila u koraku od jednog stupnja za svaki kanal prijenosa. Udaljenost najbližeg pristupa definirana je s energijom snopa i kutom detekcije, što nam omogućuje da kombiniramo različite energije i kuteve detekcije. Vjerojatnosti kanala prijenosa jednog nukleona uspoređivane su s onima za transfer dva nukleona. Usporedbom njihovih apsolutnih vrijednosti izdvojeni su faktori pojačanja EF ($P_2 = EF * P_1$). Uočeno je da faktora pojačanja, za prijenos para neutrona te para protona, nema ili je jako mali EF≈ 1. Rezultati su također uspoređeni s izračunima s pomoću GRAZING koda. Račun jako dobro opisuje eksperimentalne podatke za kanale prijenosa neutrona, kako u nagibu tako i u apsolutnoj vrijednosti. Slični zaključci dobiveni su i za protonske kanale, ali zbog nedovoljne statistike nismo bili u mogućnosti promatrati protonske kanale na najnižim energija koje su bitne kod definiranja nagiba pravca.

Svakako bi bilo dobro usporediti podatke i s nekim drugim mikroskopskim računima koji uzimaju u obzir efekte kao što su duboko neelastične doprinosi, doprinosi od sekundarnih procesa kao sto je neutronska evaporacija, te doprinos koreliranih nukleona u diferencijalnim i ukupnim udarnim presjecima.

Contents

1 Introduction

1.1 Heavy-ion reactions close to the Coulomb barrier

In heavy-ion reactions, very complex quantum mechanical processes take place, which depend on both the structures of the colliding nuclei and reaction dynamics. At bombarding energies $\leq$ 10 MeV/nucleon, which is the case in this thesis, the behavior of nuclear reactions can be described based on the impact parameter (b), which determines the closeness of the projectile and the target nucleus in the collision, as illustrated in Figure 1.1.

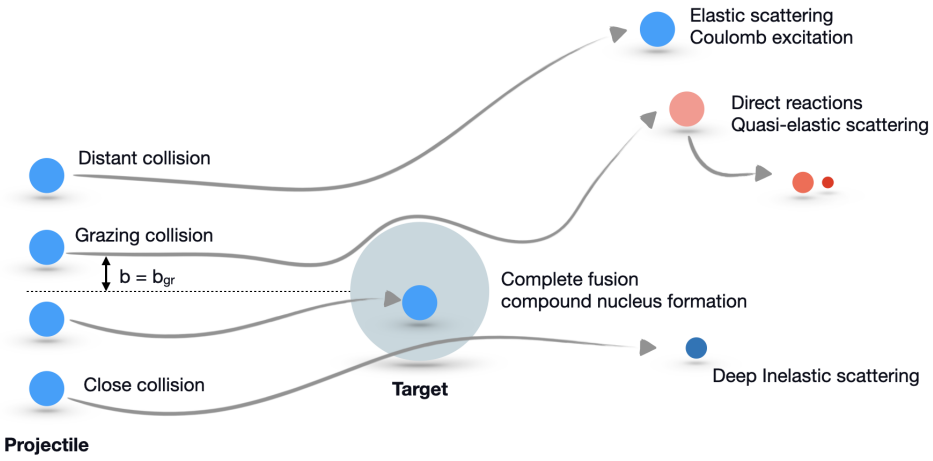

Figure 1.1: Schematic layout of different types of reactions between heavy ions at bombarding energies close to the Coulomb barrier according to different impact parameter b.

For impact parameters larger than grazing one b_{gr}, reactions such as elastic scattering and Coulomb excitation occur. The elastic scattering is fundamental to the study of the

interaction potential between the two nuclei. For example, the deviation of the elastic cross section from the Rutherford cross section indicates the occurrence of competing reaction channels, ranging from Coulomb excitation of collective degrees of freedom to transfer and other complex channels. The cross section for elastic scattering depends on both the energy and the scattering angle, and its determination is the basis for the correct treatment of any scattering process. In quasi-elastic (QE) reactions, which occur at a slightly larger impact parameter b, there are very small changes between the initial and final states of the nuclei. In the final state, there is not a significant population of the high excitation energies, and only a few nucleons may be involved in the transfer.

As the impact parameter becomes smaller in a collision, more degrees of freedom become involved. This type of collision can lead to deep inelastic scattering, a process in which large kinetic energy loss occurs. These energy loss can result in the excitation of fragments and the exchange of many nucleons between the colliding nuclei.

In this doctoral thesis, the reactions that fall somewhere in between quasi elastic and deep inelastic, where impact parameter is comparable to the grazing one, will be studied. Such reactions are referred to as Multi-Nucleon Transfer (MNT) reactions. In MNT reactions, one, two, or more nucleons are exchanged between the projectile and the target nuclei. These reactions occupy an intermediate position between quasi-elastic and deep inelastic reactions also in terms of reaction time, loss of kinetic energy, and number of exchange particles. They are discussed in more detail in section 1.2.

Certain fundamental aspects of heavy-ion reactions can be understood by examining the interaction potential between the colliding nuclei, denoted as $V(r)$. This potential encompasses three fundamental components: the Coulomb repulsion term $V_c(r)$, the short-range nuclear attraction term $V_n(r)$, and the centrifugal potential term $V_l(r)$.

Let's consider a specific reaction, namely $a + A \rightarrow b + B$. To describe the nuclear interaction, one employs a realistic expression using the Woods-Saxon potential. This potential is characterized by parameters such as the depth V_0, the diffusion parameter a, and the radii R_i.

For the sake of simplicity, let's focus on head-on collisions (with orbital angular momentum $L_b = 0$, which are related to the impact parameter $L_b = b\sqrt{2ME_{\mathrm{cm}}}$) and consider cases where the masses of the two nuclei are relatively small (i.e., $A_a \cdot A_A < 23400$). Under these conditions, the potential exhibits a maximum known as the Coulomb barrier, which

occurs at a specific distance r_c where partial derivation of $V(r)$ is 0.

However, in heavier systems, the dominant Coulomb repulsion exceeds the attractive force, so that the Coulomb barrier vanishes as in the case in the system studied here. In this thesis, the reaction being studied involves two nuclei with a product of their masses, $A_{Pb} \cdot A_{Sn}$, approximately equal to 24300, so for system like this, the Coulomb barrier fades away even for low values of the orbital angular momentum, and in fact even for the central collision.

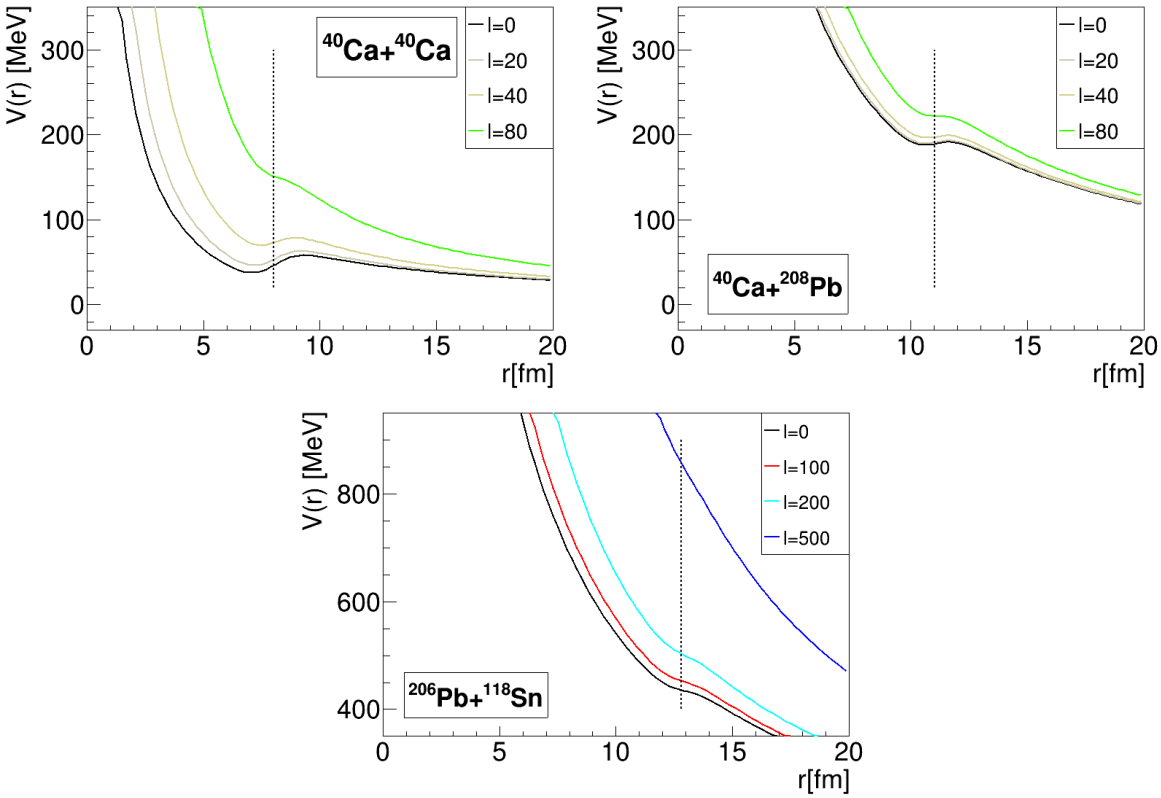

Figure 1.2: The effective potential for the ^{40}Ca+^{40}Ca, ^{40}Ca + ^{208}Pb, and ^{206}Pb + ^{118}Sn system is shown for various angular momenta, as indicated on the curves. It is observed that at low values of angular momentum (l), the Coulomb barrier is beyond the combined nuclear radii, as indicated by a dashed line. Also, as the system becomes heavier, the barrier starts to fade away.

This behavior is illustrated in Figure 1.2, for the ^{40}Ca+^{40}Ca, ^{40}Ca + ^{208}Pb, and ^{206}Pb + ^{118}Sn systems. It can be observed that the barrier vanishes for trajectories associated with large partial waves. If E_{cm} is the fixed bombarding energy, the increases of impact parameters b leads to higher angular momenta $L_b = \hbar l$, i.e. more peripheral collisions. For sufficiently large l, the centrifugal potential becomes exceptionally steep, preventing the formation of a barrier even with the maximum nuclear attraction. Also for the heavier systems, like ^{206}Pb + ^{118}Sn, as we reach an angular momentum of $l = 500$, which is

typically expected for the beam energy around the barrier (calculated using the Bass formula), the concept of a "barrier" becomes no longer applicable.

This effect can be experimentally observed in two-dimensional spectra, such as the total kinetic energy loss (TKEL) plotted against the scattering angle, where different behaviors are observed for systems of different masses (see Figure 1.4). If lighter systems with lower L_b, whose energy is close to the barrier, are compared with heavier systems, it can be seen that the events with larger energy losses tend to bend to larger scattering angles. In the next chapter, we will examine this behavior in more detail.

1.2 Multi-Nucleon Transfer (MNT) reactions

Heavy-ion MNT reactions at energies near the Coulomb barrier form a bridge between quasi-elastic (QE) and deep inelastic (DIC) processes where the evolution of the reaction is largely influenced by the underlying nuclear structure, providing an opportunity to explore specific properties such as single particle degrees of freedom, surface vibrations, and pair transfer modes, but also how dynamics evolves from QE to DIC regime.

The evolution can be illustrated by a two-dimensional matrix of the Q-value (or alternatively total kinetic energy loss (TKEL) or kinetic energy of the incoming ion) in relation to the scattering angle, known as a Wilczynski plot [1](more in Chapter 4.5.1).

Insight into the complex mechanisms at play during multinucleon transfer reactions has been provided by Wilczynski plots from previous experiments, where the different type of reactions can be distinguished. As an example, the results from the ^{64}Ni+^{238}U, ^{40}Ar+^{208}Pb, and ^{46,48,50}Ti+^{208}Pb systems are presented [2–4]. The study of the evolution in different systems and under different experimental conditions is important for enhancing our understanding of these phenomena. The ^{64}Ni+^{238}U system was investigated at the Laboratori Nazionali di Leganro (LNL) using a time-of-flight magnetic spectrometer. Similarly, the ^{40}Ar+^{208}Pb experiment was conducted at LNL, with the PRISMA magnetic spectrometer. ^{46,48,50}Ti+^{208}Pb systems were studied with a magnetic spectrograph and a gas filled focal-plane detector at the Argonne National Laboratory ATLAS facility. The population of multinucleon transfer channels was examined in each system at energies around the Coulomb barrier. Figure 1.3 displays the Wilczynski plots for the indicated transfer channels for ^{64}Ni+^{238}U (top-left), ^{40}Ar+^{208}Pb (top-right), and

^{48}Ti+^{208}Pb (bottom) systems. Different behavior is observed in each system. In the ^{64}Ni+^{238}U, the events with large energy losses are focused on the same angles as QE components, around the grazing angle. On the other hand, in ^{48}Ti+^{208}Pb, one can notice larger energy losses at more forward angles. Although both systems were measured in a wide angular range of approximately $\Delta\theta_{cm} \approx 70°$, the distribution appears to be more "bent" towards forward angles for the ^{48}Ti+^{208}Pb system. This observation can be explained by the larger beam energy compared to the Coulomb barrier (Bass formula). Specifically, the ^{64}Ni+^{238}U system was measured with a beam energy 15% higher than the Coulomb barrier, while the ^{48}Ti+^{208}Pb system was measured with a beam energy 25% higher. The increase in beam energy results in larger energy losses. The bending effect in the ^{48}Ti+^{208}Pb system is clearly evident in the differential cross sections (projection of Wilczynski plot on angle axis), where quasi-elastic and deep inelastic components are visible. The quasi-elastic component shows a Gaussian-like angular distribution centered around the grazing angle. On the other hand, the deep inelastic component exhibits a rise at forward angles.

The ^{40}Ar+^{208}Pb system was measured at a smaller angular range of approximately $\Delta\theta_{cm} \approx 20°$ with a beam energy 30% higher than the Coulomb barrier, and similar behavior, as in the ^{64}Ni+^{238}U system, is visible. For the few nucleon transfers and neutron transfers, most of the yield is concentrated close to the grazing angle, and the large energy loss tails do not strongly influence the measured cross section. However, for the more complex transfer channels, particularly those involving the pick-up of protons, large energy losses have been observed, which are clearly visible in the ^{41}K channel (see figure 1.3). When differential cross sections have been constructed for relatively low energy losses (up to $\approx$ 20 MeV), a typical Gauss-like angular distribution has been obtained. In contrast, angular distributions connected with the large energy loss tails turned out to be rather flat.

Distributions of these three different systems indicate that events in the deep-inelastic regime are around or at more forward angles than the grazing angle [5, 6]. But, on the other hand, as we move to more heavier systems, different observations can be made.

The Wilczynski plots for different systems, from lighter to heavier, extracted from the GSI data [5] are displayed in Fig. 1.4. In all systems the DIC components showed up as large energy loss tails. The trends of the tails extending to lower TKE (total kinetic energy)

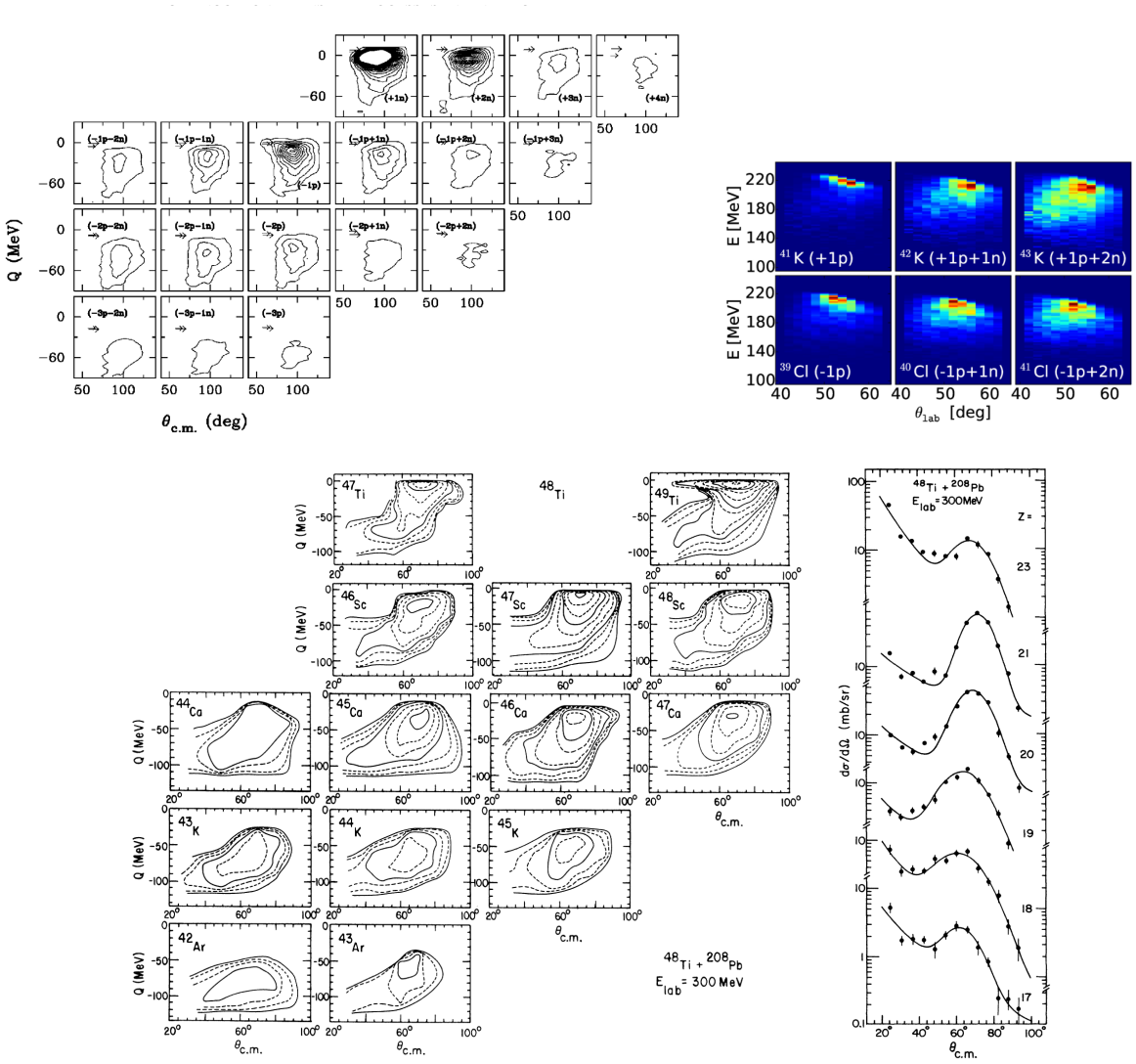

Figure 1.3: Wilczynski plots for indicated transfer channels for ^{64}Ni+^{238}U (top-left)[2], ^{40}Ar+^{208}Pb (top-right)[3] and ^{48}Ti+^{208}Pb (bottom) [4] systems. Angular distributions for ^{48}Ti+^{208}Pb, obtained for integration of all isotopes and excitation energies (bottom-right)[4].

are mainly determined by the product of the atomic numbers of the projectile and target Z_pZ_t. As this product increases, the reaction evolves from an "orbiting" configuration (top panels) where the two nuclei remain in contact for quite some time, and rotate in a di-nuclear configuration where many nucleons are exchanged, to an intermediate "focusing" configuration (bottom left panel) where they remain in contact for a shorter time and then scatter over a limited angular range, to a "repulsive" configuration (bottom right panel) where the Coulomb field is so strong that the nuclei cannot come into contact. This repulsion is related to the disappearance of the Coulomb barrier, i.e. disappearance of the "pocket" in the interaction potential for heavy systems, even for head-on collisions ($l = 0$), as depicted in Figure 1.2. It is important to note that in the measurement presented in

Fig. 1.4, only Z identification has been performed, but the trend is clearly visible. For us, the Xe+Au case will be very relevant due to its similar mass as the system studied in this thesis. The Wilczynski plot clearly demonstrates that for this rather heavy system, the large energy losses occur at the grazing angle, a phenomenon known as angular focusing. In this reaction, a cross-section ridge moves down in energy at an almost constant angle. This angular focusing can be understood as a balance between repulsive and attractive forces.

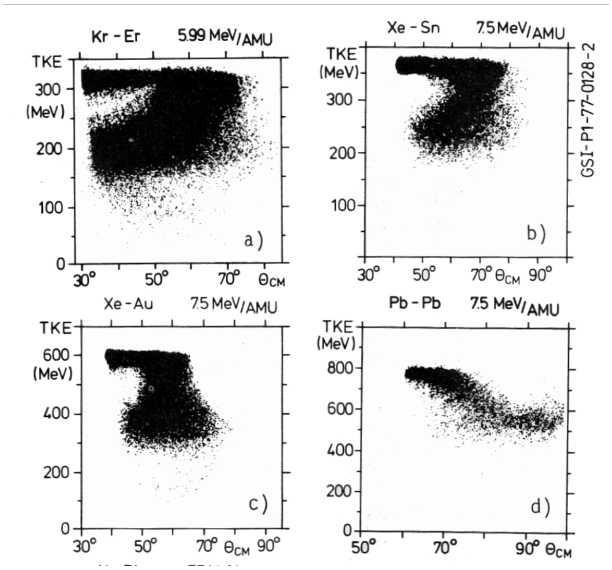

Figure 1.4: Wilczynski plots for the indicated systems are presented. Figure is taken from Refs.[5].

Over the past four decades, a lot was learned about MNT reactions, but a particular interest in such reactions has recently intensified. This renewed interest was driven by two main factors. Firstly, the recognition of these reactions as a valuable tool for producing exotic, heavy and neutron-rich nuclei. Secondly, the successful implementation of large solid angle magnetic spectrometers, which enable efficient identification of multinucleon transfer products. This led to the acquisition of not only insights into the evolution of reactions but also high-quality data on the total cross sections, angular and energy distributions of various reaction channels.

As an example, Figure 1.5 illustrates the total cross sections for different systems: the ^{40}Ar, ^{40}Ca and ^{58}Ni projectile on ^{208}Pb target [3], a heavy ^{197}Au + ^{130}Te system [7], and a system with a radioactive beam ^{94}Rb + ^{208}Pb [8]. The figure also includes GRAZING calculations [9] (see more in Chapter 1.2.1). Due to ^{208}Pb being a doubly magic nucleus,

calculations can be performed more reliably. For reactions with ^{58}Ni and ^{40}Ca projectiles, the available channels are limited to proton stripping and neutron pick-up channels, whereas the ^{40}Ar + ^{208}Pb reaction allows for both neutron and proton stripping and pick-up channels. In the ^{197}Au + ^{130}Te and ^{94}Rb + ^{208}Pb systems, only neutron transfer channels had been extracted. In general, while GRAZING describes well pure neutron transfer channels and one-proton transfer channels, it underestimates experimental data for channels involving the transfer of multiple protons, as depicted in the total cross sections shown in Figure 1.5.

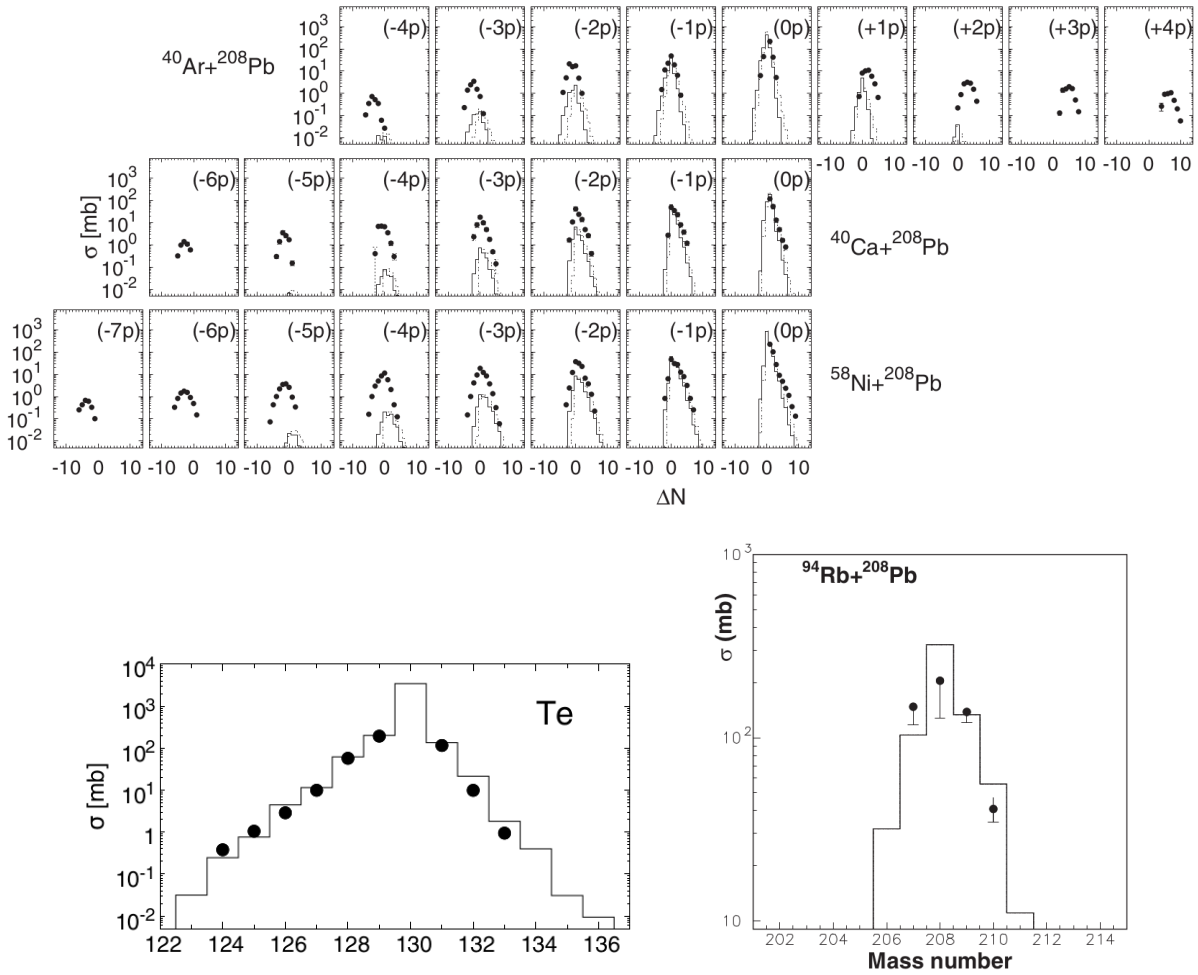

Figure 1.5: Experimental total cross sections for the ^{40}Ar, ^{40}Ca and ^{58}Ni + ^{208}Pb (top) [3], ^{197}Au+^{130}Te (bottom-left) [7], and ^{94}Rb + ^{208}Pb (bottom-right) [8] (points) are shown together with GRAZING [9] calculations (histogram).

The channels involving the transfer of multiple protons and neutrons can be better described using the Complex Wentzel-Kramers-Brillouin (CWKB) model, which allows for the inclusion of additional degrees of freedom. In figure 1.6 total cross sections for system

^{58}Ni + ^{208}Pb (points) is shown again but this time together with CWKB calculations (histograms). The calculations presented in the top row only consider single nucleon transfer modes, while those in the middle row include a pair mode as well. The pair mode includes the fact that pairs of nucleons can be correlated and that nucleon transfers are influenced by that. In the bottom row, evaporation effects are also taken into account. Inclusion of the pair mode along with the transfer of individual nucleons, leads to an improved description of the data, in particular in the proton sector. This suggests that pair modes may play a significant role as an additional degree of freedom in the transfer process. These results demonstrate that multinucleon transfer reactions near the Coulomb barrier, can serve also as a valuable tool for studying nucleon-nucleon correlation properties.

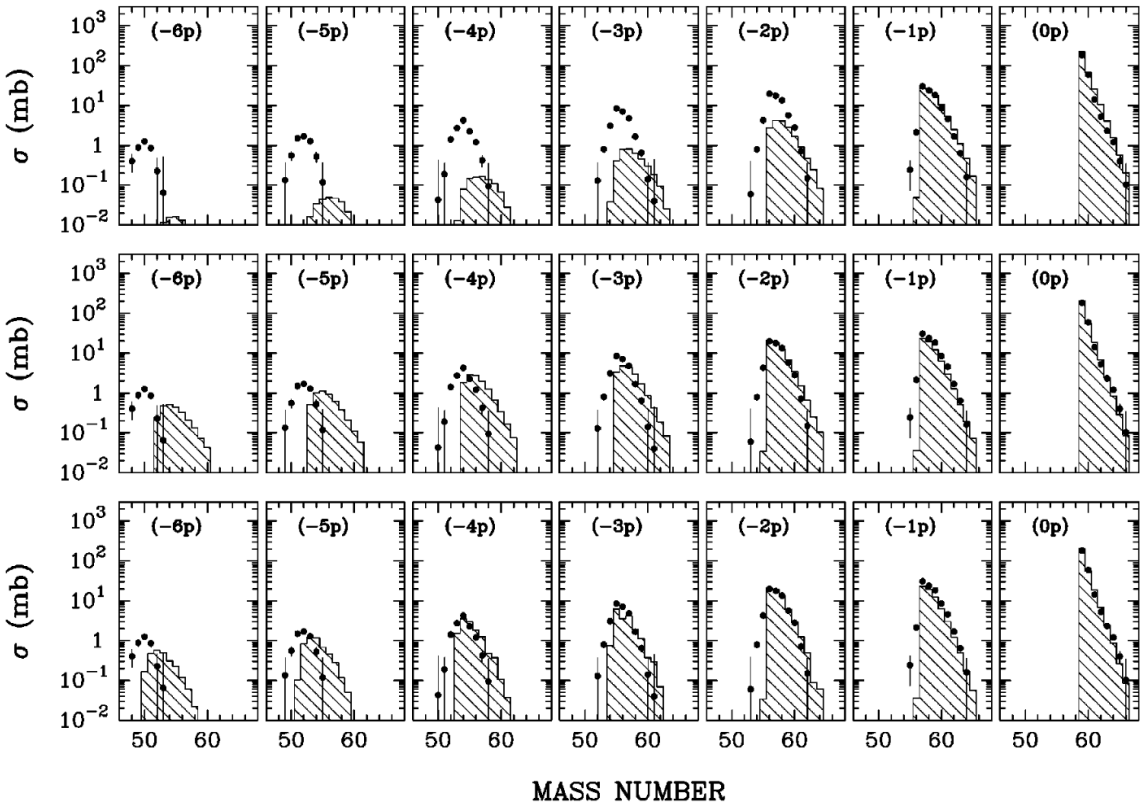

Figure 1.6: Total cross sections for system ^{58}Ni + ^{208}Pb (points) is shown together with theoretical CWKB calculations (histograms); the results of calculations taking into account independent particle transfers (top row), the addition of pair modes for neutrons and protons (middle) and neutron evaporation (bottom). Figure is taken from Ref. [10].

1.2.1 The theoretical description of MNT reactions

In this chapter the importance of form factors and optimum Q-value consideration in the study of MNT reactions will be discussed. Additionally, semi-classical models such as GRAZING, will be briefly explained in this section. Furthermore, the Time-Dependent Hartree-Fock theory (TDHF) will also be introduced, as well as other models that are currently used to describe the transfer process within a dynamic approach.

Form factors and optimum Q-value

The MNT reactions in the heavy ion systems are governed by form factors which contain information of colliding nuclei and the dynamics. MNT are also governed by the optimum Q-value, which contains information about the balance of the internal and binding energy in the phase space of colliding nuclei.

The form factors determine the relative strength of different channels. They are represented by the matrix element between initial and final states in the transfer process:

$$f_{\beta\gamma}(\vec{k},\vec{r}) = \left\langle \omega_\beta \left| V_\gamma - U_\gamma \right| \psi_\gamma \right\rangle, \tag{1.1}$$

where $\vec{r}$ represents the center of mass distance, $\vec{k}$ the transfer momentum, $\langle\omega_\beta|$ constitute a dual basis introduced to overcome the problem of the non-orthogonality of the vectors $|\psi_\gamma\rangle$, U is the nuclear potential and V is the coupling interaction.

For the transfer process, the form factor depends not only on the distance between the two nuclei but also on the momentum transfer $\vec{\kappa}$. At large distances, utilizing the parametrization from Ref.[11] , the form factor can be expressed as follows:

$$f^{\text{tran}}_{\beta\gamma}(0,r) \propto \frac{e^{-\kappa_{a'_1} r}}{\kappa_{a'_1} r}. \tag{1.2}$$

Here, the coefficient $\kappa_{a'_1}$ incorporates the binding energy of the single-particle state a'_1 involved in the transition, and primarily governs the asymptotic behavior of the transfer form factor. At large distances, this component predominates over the nuclear part of the inelastic form factor.

For inelastic excitation, the form factor can be expressed as the derivative of the average potential of the entrance and exit channels $U(r)$ with respect to r, multiplied by a

deformation parameter β_λ that characterizes the state's collectivity:

$$f_{\beta\gamma}^{\text{inel}}(r) = \beta_\lambda \frac{\partial U(r)}{\partial r}. \tag{1.3}$$

The dependence of the cross-section on the Q-value is important because such observation may allow one to determine which transfer channels are open and which are closed in a certain reaction at a given beam energy.

The probability of transition from the entrance channel α to channel β, in direct processes where two nuclei do not overlap, can be written in the following form:

$$P_{\beta\alpha} = \sqrt{\frac{1}{16\pi\hbar^2 \left|\ddot{r_0}\right| \kappa_{a_1'}}} \left| f_{\beta\alpha}(0, r_0) \right|^2 g\left(Q_{\beta\alpha}\right). \tag{1.4}$$

Here, $\ddot{r}_0$ represents the radial acceleration at the distance of closest approach r_0 for the grazing partial waves, and the cut-off function g(Q) is defined as:

$$g(Q) = \exp\left[-\frac{(Q - Q_{opt})^2}{\hbar^2 \ddot{r_0} \kappa_{a_1'}} \right]. \tag{1.5}$$

The optimum value of Q, denoted as Q_{opt} is:

$$Q_{opt} = \left(\frac{Z_d}{Z_A} - \frac{Z_d}{Z_b} \right) E_b + \left(\frac{m_d}{m_b} - \frac{m_d}{m_A} \right) (E - E_b) + \frac{m_d \ddot{r}_0}{m_a + m_A} (R_A m_b - R_a m_B). \tag{1.6}$$

Here, we examine the system $A + a \rightarrow B + b$, where E_b represents the Coulomb barrier, and m_d and Z_d denote the mass and charge of the transferred particle, respectively. These quantities are defined as positive for stripping reactions, negative for pick-up reactions, and zero for inelastic scattering. It is important to note that this equation is valid when the trajectories of the colliding nuclei smoothly match around the turning point where the contribution from the form factor peaks. This approximation holds true when the number of nucleons transferred is limited to a few units. The bombarding energy dependence of the cut-off function is contained in the $\ddot{r}_0$ term that defines its width (inversely proportional to the collision time).

Let's examine as an example the ^{58}Ni + ^{208}Pb reaction [12]. Figure 1.7 illustrates the Q-value considerations. The adiabatic cut-off function $g(Q)$ is also shown for both one-particle and two-particle transfer channels.

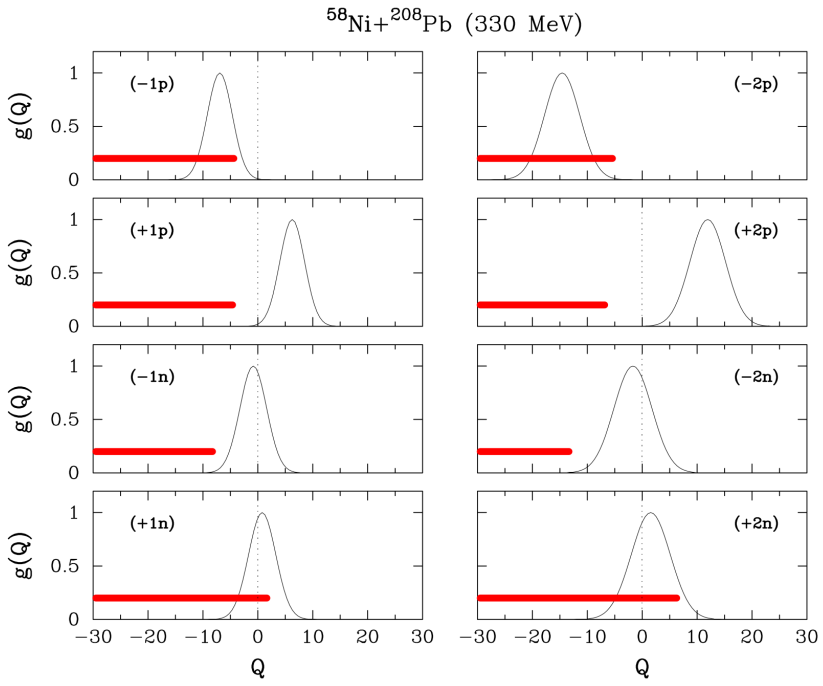

Figure 1.7: The adiabatic cut-off functions for one- and two-neutron and proton transfer channels in the reaction ^{58}Ni + ^{208}Pb. The energy is indicated by the corresponding Q-value in MeV. The horizontal red lines in the figure represent the positions of all possible transitions for the given channels. Figure is taken from Ref. [12].

In the same figure, horizontal lines are used to indicate the potential transitions for all channels. It is evident that only the channels with Q values below the bell-shaped curve are allowed to occur. Consequently, the only viable transfers in this specific system are neutron pick-up and proton stripping. All other channels are hindered due to optimal Q-value considerations. Furthermore, the figure reveals that in certain channels, particularly two-proton stripping, but also one-proton striping and two-neutron pick-up, the transition may occur at higher excitation energies in the final fragments. By reducing the bombarding energy, the collision time is increased, and the Q-value window becomes narrower. As a results, the average number of transferred nucleons decreases. Conversely, increasing the bombarding energy results in closer collisions and the average number of transferred nucleons increases.

This situation is true for most combinations of projectile and target when using stable beams. In a collision process involving a light projectile and a heavy target, the balance of Q-values for proton and neutron striping and pick-up channels is mostly controlled by the lighter partner. With neutron-rich projectiles, channels for proton pick-up and neutron stripping also open up, facilitating the population of neutron-rich heavy fragments.

The GRAZING code

The theory with which we will compare our results is the theoretical model [13, 14] implemented in the GRAZING code [9]. The GRAZING code was developed by A. Winther to explain the behavior of inelastic scattering and nucleon transfer during grazing collisions of heavy ions. This semi-classical model combines the classical motion of the colliding nuclei along their trajectories in the entrance and exit channels, along with quantum calculations to determine the probabilities of exciting collective states and transferring nucleons. It assumes that inelastic excitation of nuclei, as well as neutron and proton transfers, are independent of each other and primarily occur at the closest distance of approach between the colliding nuclei (referred to as the "turning point" in elastic scattering). The cross sections are calculated by summing over the impact parameters b, which are related to the angular moments of relative motion $L_b = b\sqrt{2ME_c m}$. The model effectively describes processes involving the transfer of a few nucleons with relatively small loss of kinetic energy.

The GRAZING constructs the probability for a given transition, which is characterized by several observables such as the excitation energy E_i^*, number of neutrons N_i, number of protons Z_i, and so on, for the reaction products. This probability is not directly obtained by solving the semi-classical system of coupled equations but instead, it is derived by introducing a characteristic function $P(E_{\rm a}^* E_A^* N_{\rm a}, Z_{\rm a}, \ldots)$.

This probability is obtained through an integral involving a characteristic function. Skipping the detailed explanation, it is worth mentioning that the transition probabilities are calculated based on classical trajectories that are self-consistently constructed to ensure compatibility with the various quantities defining the final states. To describe the relative motion and calculate the inelastic form factors, GRAZING utilizes the Akyüz-Winther parametrization for the nuclear ion-ion potential:

$$U_{aA}^N = -16\pi\gamma a \frac{R_{\rm a} R_A}{R_{\rm a} + R_A} \left[\frac{1}{1 + {\rm e}^{(r - R_{\rm a} - R_A)/a}}\right]. \tag{1.7}$$

Here, the nuclear radii are given by:

$$R_i = \left(1.20 A_i^{1/3} - 0.09\right) \quad \text{fm}. \tag{1.8}$$

The diffusion parameter is:

$$\frac{1}{a} = 1.17\left(1+0.53\left(A_{\mathrm{a}}^{-1/3}+A_{A}^{-1/3}\right)\right) \quad \mathrm{fm}^{-1}. \tag{1.9}$$

And the surface tension is:

$$\gamma = -0.95\left[1-1.8\frac{(N_{\mathrm{a}}-Z_{\mathrm{a}})\,(N_A-Z_A)}{A_{\mathrm{a}}A_A}\right] \quad \mathrm{MeVfm}^{-2}. \tag{1.10}$$

In the above expressions, A_i represents the mass number, while Z_i and N_i denote the charge and neutron number, respectively. For the Coulomb interaction, the model employs the expression for two point charges. This parametrization was used for calculation of the interaction potentials for different systems in figure 1.2.

The GRAZING model's predictions have been effectively validated by comparing them to various experimental data sets, such as the ones from the ^{58}Ni + ^{124}Sn reaction (shown in Figure 1.8 and 1.9). This particular reaction has been extensively examined experimentaly and theoreticaly by the Argonne group [12, 15, 16]. For numerous channels different processes have been measured across different bombarding energies, including differential and total cross sections for the elastic scattering (first panel of the Fig. 1.8), the differential cross sections of the transfer channels (last three panels of Fig. 1.8, the excitation function of evaporation residues and of the deep inelastic components, and fission products (1.9).

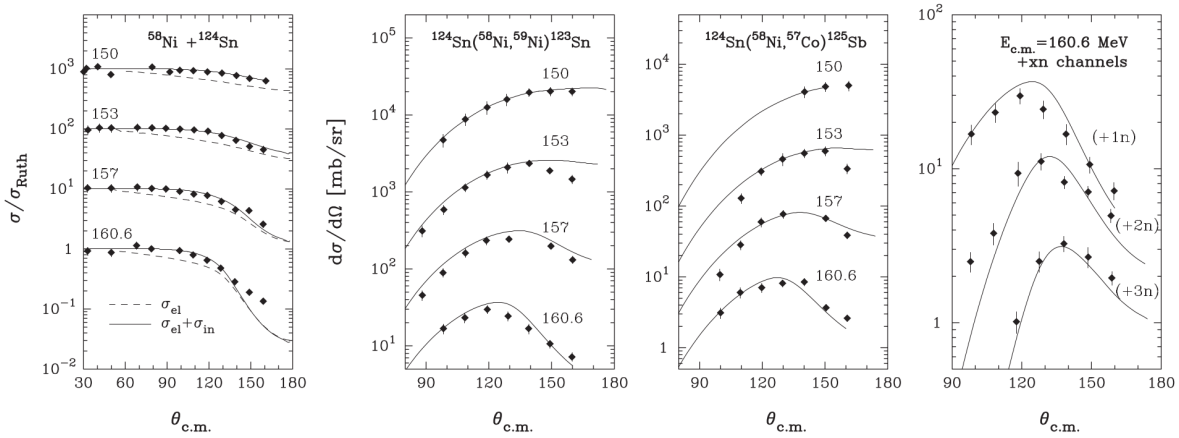

Figure 1.8: Experimental center-of-mass angular distributions (points) for elastic plus inelastic and different multineutron transfer channels and ones calculated with GRAZING (solid and dash lines). The label in each frame indicates the center-of-mass bombarding energy in MeV. Figure is taken from Ref. [12].

GRAZING describes well the elastic, and differential cross sections of the transfer channels. The model is also able to estimate well the capture cross section in the reaction shown in Figure 1.9. The good agreement with the data could be obtained only after performing a summation over the deep inelastic components with the evaporation residue and fission ones.

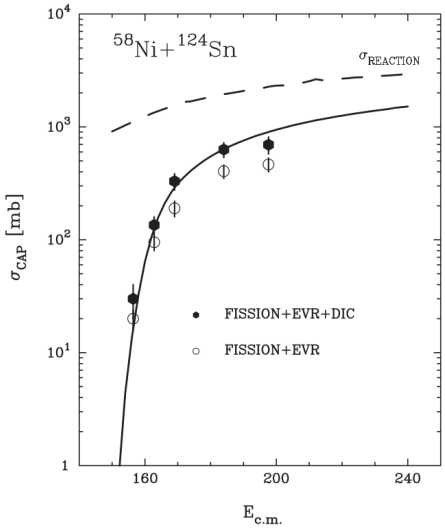

Figure 1.9: Experimental (points) and GRAZING calculations (curves) for different reaction channels in the ^{58}Ni+^{124}Sn system. The dashed line represents the total reaction cross section, while the solid line is the sum of evaporation residue (EVR), fission, and deep inelastic (DIC) cross sections, accounting for for the capture cross section. Figure is taken from Ref. [12].

Different theoretical approaches to MNT reactions

Another semi-classical method used to describe transfer reactions is the CWKB model. The complex Wentzel-Kramers-Brillouin (CWKB) was first introduced in nuclear physics by Knoll and Schaffer in 1973 [17], and it has been effectively employed in the study of MNT reactions in heavy ion systems [18, 19].

The CWKB calculations use one-particle transfer form factors constructed from the single-particle wavefunctions of the states involved in the transition. Because of that CWKB calculations can be more precise but also more time-consuming. The calculation of multi-nucleon transfer channels follows a multi-step mechanism, similar to GRAZING, but with the option to explicitly include pair transfer modes. This calculations used the WKB approximation [20] to determine the radial wave functions and compute the initial transfer amplitudes. In this approach, the real part of the optical potential is derived from an empirical potential as in Ref. [21], while the imaginary part is obtained through microscopic

calculations [22, 23].

Figure 1.10 presents the comparison between GRAZING and CWKB models for the ^{40}Ca, ^{58}Ni + ^{208}Pb reactions. As shown in Figure 1.10, these two calculations give similar results, and both are well-matched with experimental data, at least for the one-nucleon transfer. While GRAZING describes slightly better the distribution at more forward angles, the CWKB method better describes the distribution at more backward angles.

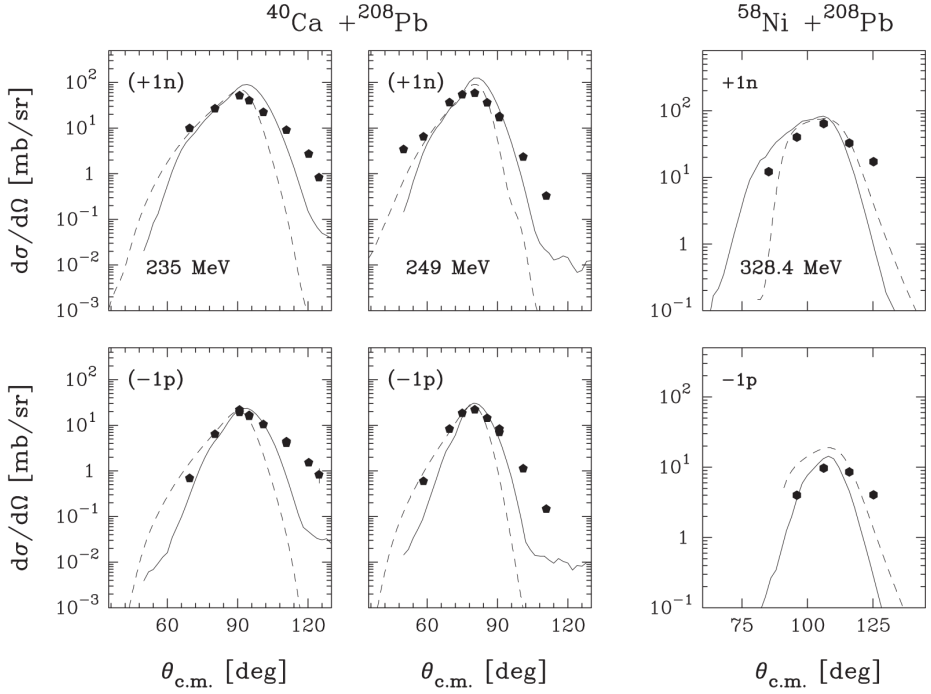

Figure 1.10: Center-of-mass angular distributions for different transfer channels, for two systems and for different bombarding energy, calculated with GRAZING (dash curve) and CWKB (solid curve) and experimental data (points). Figure is taken from Ref. [12].

While the semi-classical models describe well successive transfer processes at peripheral collisions it misses deep-inelastic components at small impact parameters. On the other hand, Time-dependent Hartree-Fock (TDHF) deals with the individual wave functions of nucleons, encompassing not only dynamical effects like nucleon transfer and internal excitation but also naturally incorporating structural effects such as shell effects and shape evolution into the description. Combining TDHF with a statistical compound-nucleus deexcitation model, GEMINI++, it became possible to compute the secondary cross sections after deexcitation processes. Such methods are highly computationally demanding, and some additional effects, like pairing interactions, have only been introduced recently with the advancement of computational technology.

More recently, TDHF was applied to investigate various nuclear reactions, including multinucleon transfer reactions [24–27], some of which involve pairing correlations. In a recent paper [28], the TDHF+GEMINI method was introduced, which allows for the evaluation of production cross sections for secondary products, such as neutron evaporation, in heavy ion reactions. The importance of secondary products has been noticed before; for example, in the ^{58}Ni+^{208}Pb system [10], it was important to include secondary processes (neutron evaporation) for a better description of the data (see Figure 1.6). The method combines the microscopic description of reaction dynamics using the time-dependent Hartree-Fock (TDHF) theory with the extraction of production probabilities, total angular momenta, and excitation energies from the TDHF wave function. The secondary deexcitation processes, including particle evaporation and fission, are then described using the GEMINI++ compound-nucleus deexcitation model. The method is applied to several specific reactions with available experimental cross-section data. As an example in figure 1.11 the results for the ^{58}Ni+^{208}Pb and the ^{136}Xe+^{198}Pt systems are shown. The red dots represent the experimental data, while green histograms are GRAZING calculations with evaporation effect included, red histograms are TDHF calculations and the blue lines are TDHF+GEMINI calculations. The population of transfer channels is determined by Q-value consideration, as described in section 1.2.1. So while in the ^{58}Ni+^{208}Pb system, due to Q-value consideration, neutron pickup and proton stripping are favored, in ^{136}Xe+^{198}Pt system one expects transfer of neutrons and protons toward both directions.

When examining the primary and secondary reaction products, the significant impact of deexcitation processes become evident. Remarkably, the TDHF+GEMINI model describes well the measurements for proton-stripping channels (-xp), capturing both the magnitude and central values of the cross sections for the secondary products. However, in proton-pickup channels (+xp), there is an overestimation of the magnitude of the cross-section, while the central values are well matched with the data. This particular discrepancy is mostly visible in the ^{136}Xe+^{198}Pt reaction.

Although by including deexcitation effects dominated by neutron evaporation, the cross sections calculated by TDHF+GEMINI align more closely with experimental data, discrepancies remain, particularly in multiproton transfer processes. This suggests the need for a description beyond the standard self-consistent mean-field theory to accurately capture multinucleon transfer processes in low-energy heavy ion reactions.

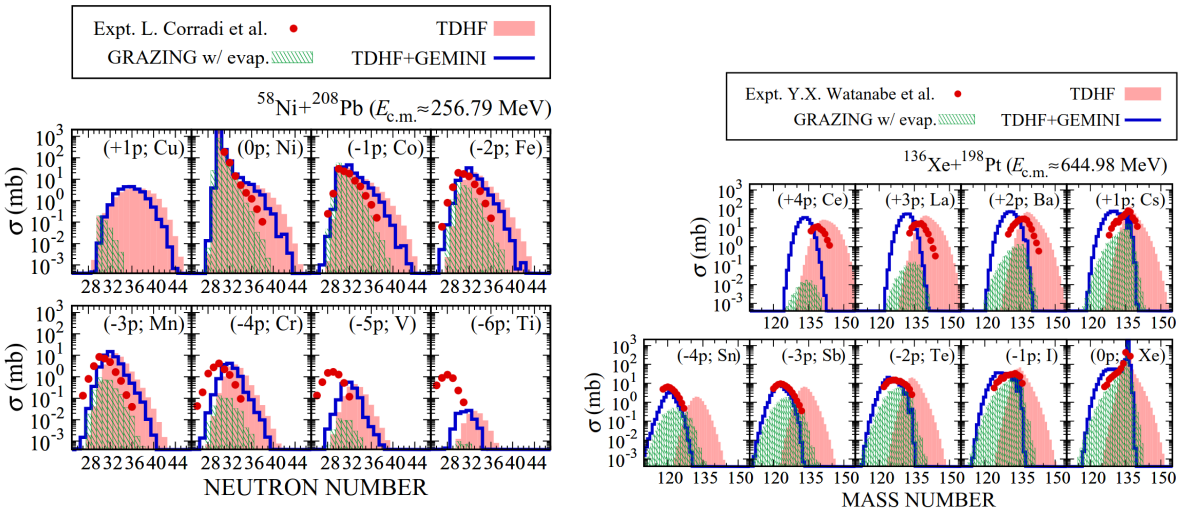

Figure 1.11: Figure is taken from Ref. [28].

Beside TDHF, various other models have been developed to describe damped collisions in nuclear physics. A dynamical model based on Langevin-type equations was developed to analyze deep-inelastic scattering, fusion-fission reactions, and collisions induced by heavy and light ions [29–34]. This model considers important degrees of freedom such as the distance between nuclear centers, surface deformations, and mass asymmetry. The Langevin-type equations successfully describe angular, energy, and mass distributions of reaction products in deep-inelastic scattering and multinucleon transfer reactions near the Coulomb barrier.

Also, the DiNuclear System (DNS) model study the dynamics of damped collisions between heavy nuclei and tries to explain complete fusion and quasifission [35–47]. The DNS model has also been extended to study transfer reactions and the population of neutron-rich nuclei.

Recently, the improved Quantum Molecular Dynamics (ImQMD) model, an extension of the Quantum Molecular Dynamics model was used in intermediate energy heavy-ion collisions [48–52]. The ImQMD model tracks the evolution of a nuclear reaction through the coordinates and momenta of each nucleon. It was applied to describe fusion reactions near the Coulomb barrier and the production of superheavy fragments in heavy-ion collisions, such as ^{238}U + ^{238}U [35–37].

All these models provide valuable insights into the dynamics of damped collisions and contribute to our understanding of various nuclear phenomena, including fusion, quasifission, transfer reactions, and the production of exotic and neutron-rich nuclei.

1.3 Nucleon-nucleon correlations

More than half a century ago, Bohr, Mottelson, and Pines introduced the concept of pairing correlations within atomic nuclei. These correlations imply that the binding energy of a nucleon pair is expected to be smaller than twice the binding energy of a single nucleon. This is due to the fact that the breaking of the pair requires additional energy. In the following sections, a discussion of various experimental results that provide evidence for the presence of pairing correlations in nuclei will be explored.

One of the earliest indications of pairing phenomena emerged from a systematic study of binding energies, where the observation of even-odd staggering provided valuable evidence. Figure 1.12 illustrates experimental evidence of this phenomenon, displaying the neutron binding energy (B_n) for various isotopes of Ca, Sn, and Pb [53]. If pairing correlations exist, we would expect nuclei with an even number of neutrons to exhibit stronger binding energy (B_n), as clearly seen in the data. Thus, for odd mass numbers (A), the binding energy given by the relation: $E_{\text{bind}}(A) < \frac{1}{2}\left(E_{\text{bind}}(A-1) + E_{\text{bind}}(A+1)\right)$. The dependence of the neutron separation energy (B_n) on the neutron number N for different isotopes suggests the presence of pairing correlations in nuclei with even neutron numbers:

$$B_n(N,Z) = M(N-1,Z) + m_n - M(N,Z) = E_{\text{bind}}(N,Z) - E_{\text{bind}}(N-1,Z). \qquad (1.11)$$

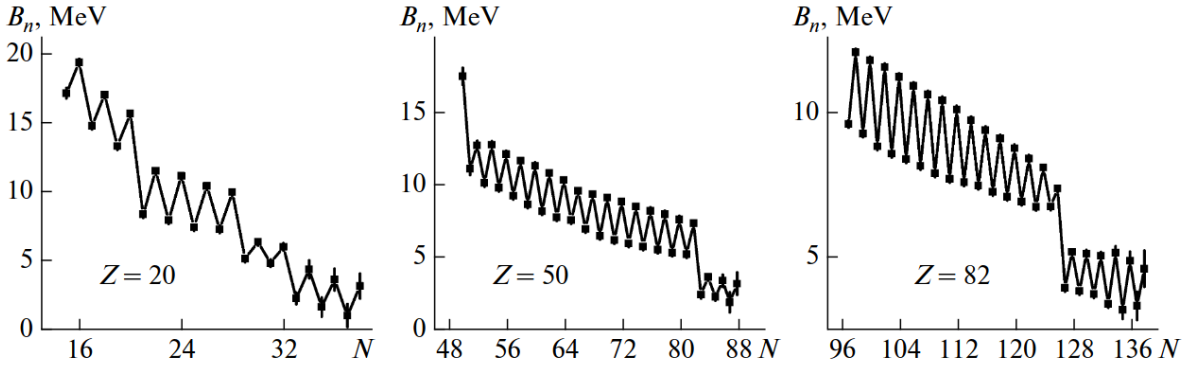

Figure 1.12: The even-odd staggering effect. Dependence of the neutron binding energy (B_n) on the neutron number N in the Ca, Sn, and Pb isotopic chain [53, 54].

Another evidence is the tendency of nucleons to form bound pairs with total momentum $J = 0$, which is observed in experiments where the ground states of more than 800 known

even–even nuclei have total momentum $J^P = 0^+$.

In addition, the pairing is manifested through the energy gap between ground and first excited state in even-even nuclei. An energy gap is around 1-2 MeV, while for double magic nuclei such as ^{40}Ca, it is even larger than 3 MeV, which is much higher than for even-odd nuclei. For example (Figure 1.13), the first excited state in ^{42}Ca and ^{44}Ca is $>$ 1 MeV, while the first excited state in ^{43}Ca and ^{45}Ca is < 0.4 MeV. This larger energy gap in even-even nuclei can be explained by considering that nucleon pair has to be split apart to form the first excited state.

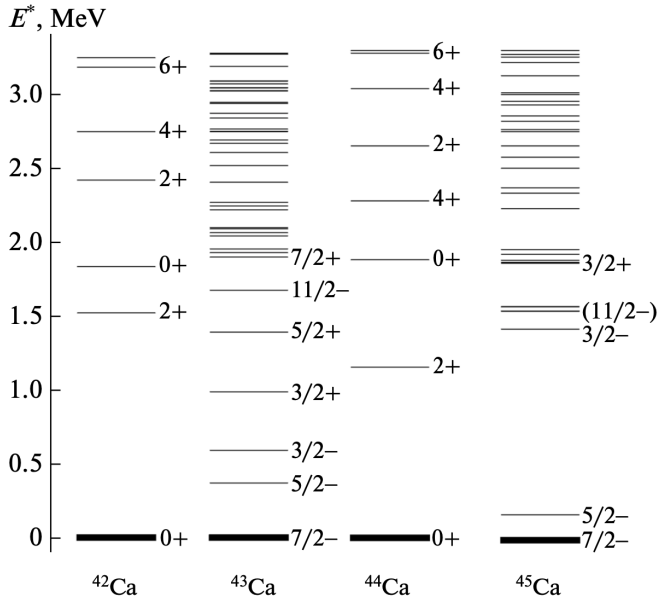

Figure 1.13: Spectra of the excited states of $^{42-45}$Ca isotopes [54].

Furthermore, the evidence of pairing can also be seen by studying moments of inertia, which are shown in Figure 1.14 for even-even nuclei. One can observe that the experimental values fall between the theoretical models of a rigid body and those with irrotational character. The data is described well by the theoretical model (Cranking) which includes the pairing contribution.

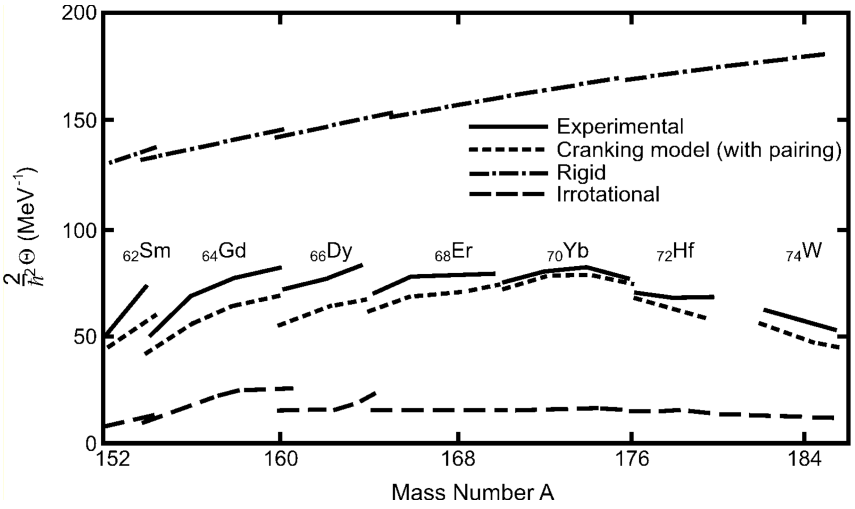

Figure 1.14: Comparison of experimental results and theoretical calculations of the moment of inertia (Rigid rotor, Cranking and Irrotational flow model) for different even-even nuclei [55].

1.3.1 NN correlations in MNT reactions

In addition to static manifestations of pairing, it is also possible to observe the dynamic effect of the pairing in reactions. The MNT reactions have a great advantage as they enable the simultaneous observation of different exit channels. The comparison of single-nucleon transfer channels with channels involving the transfer of two nucleons are a valuable tool for investigating nucleon-nucleon correlations induced by the pairing interaction [56–59]. Different experiments in the past have aimed to extract enhancement coefficients, which represent the ratio of actual transfer cross-sections to model predictions using uncorrelated states. After pioneering studies of two-neutron transfers with triton beams, the availability of various heavy ions as projectiles, especially the ^{14}C, ^{18}O, ^{22}Ne beams, and heavier ions, increase interest in experimental and theoretical study of two-nucleon transfer reactions [60, 61]. Subsequently, two-proton transfer reactions, initially investigated using the (^{3}He, n) reaction [62], have been studied with slightly heavier projectiles such as ^{14}C and ^{16}O [63–66]. More recent research has focused on employing much heavier projectiles, including the isotopes of Sn [67], and even heavier ones such as Xe [68, 69], Gd [70], W [71], and, more recently, beams of Pb [72, 73]. However, these studies suffer from limitations, as they mainly focus on inclusive cross-sections at energies above the Coulomb barrier where more complex processes take place. Despite these challenges, recent microscopic calculations have offered compelling insights, successfully describing pairing correlations and showing good agreement with experimental data [74–77].

Transfer reaction data, measured around the barrier, is often represented via the transfer probability (P_{tr}), defined as the ratio of the transfer yield over the quasi-elastic one,

$$P_{tr} = \frac{d\sigma_{tr}}{d\sigma_{el}}. \tag{1.12}$$

expressed as a function of the distance of closest approach (d) for Coulomb trajectories:

$$d = \frac{Z_t Z_p e^2}{2E_{cm}} \left(1 + \frac{1}{\sin(\theta_{cm}/2)}\right), \tag{1.13}$$

or alternativly with reduced distance (d_0),

$$d_0 = \frac{d}{A_1^{1/3} + A_2^{1/3}} \tag{1.14}$$

(where Z_t and Z_p are atomic numbers of the target and projectile, while E_{cm} and $\sin(\theta_{cm})$ are the beam energy and angle of detection, respectively).

The probabilities for one and two neutron transfer channels were recently obtained, at the LNL-INFN facility, for ^{96}Zr+^{40}Ca [74] and ^{116}Sn+^{60}Ni [75, 76] systems, and results are shown in figure 1.15 together with theoretical calculations. Both reactions were measured in inverse kinematics with the bombarding energy ranging from the Coulomb barrier to far below it. Despite the significantly smaller cross sections compared to higher energies, the low bombarding energy ensures that the transfer processes are mainly direct ones. Recoils were identified with the large magnetic spectrometer PRISMA. Experimental transfer probabilities were extracted for one and two neutron pick-up channels for the lighter partner. In addition, semi-classical calculations are provided for both systems.

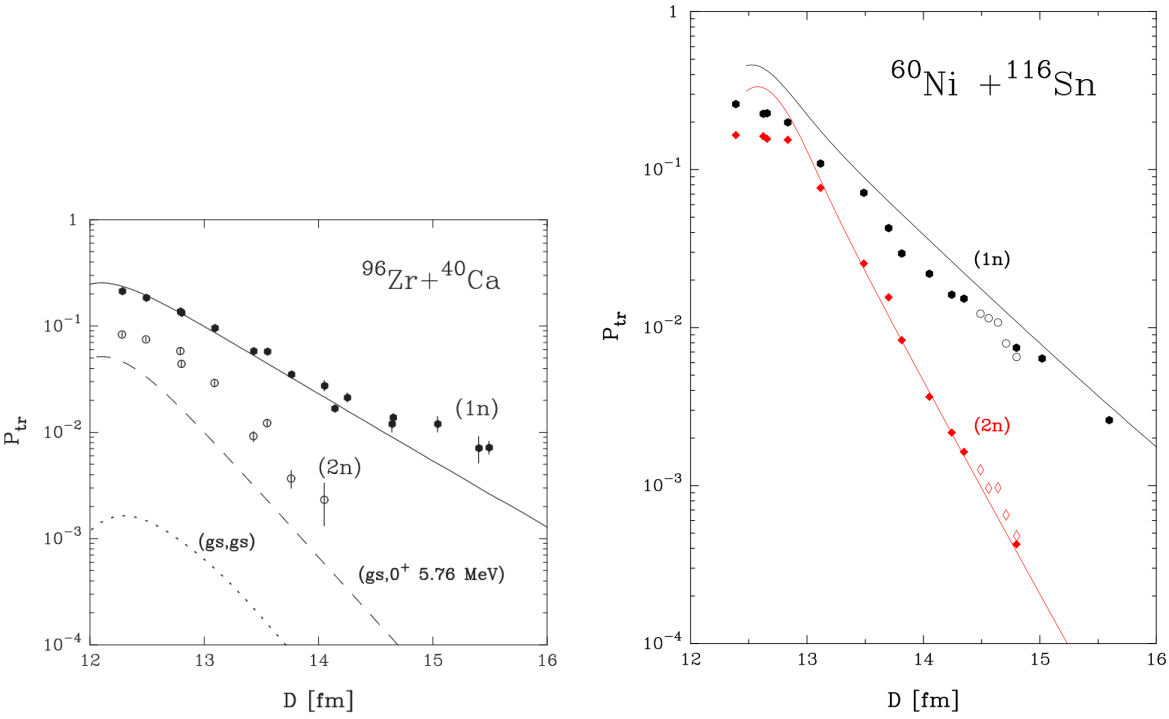

Figure 1.15: Experimental transfer probability (P_{tr}) vs. distance of closest approch (D) for ^{96}Zr+^{40}Ca (left) and ^{60}Ni+^{116}Sn (right) systems together with theoretical calculations.
Left: The full line represents the inclusive transfer probability for one-neutron transfer, the dotted line the ground-to-ground state transition for the two-neutron transfer, and the dashed line the transition to the 0^+ excited state at 5.76 MeV in ^{42}Ca.
Right: Open symbols correspond to the results from the angular distribution in direct kinematics while solid symbols refer to the excitation function measurement performed in inverse kinematics. The full lines represent microscopically calculated transfer probabilities for one- (black) and two-neutron (red) pickup. Figures are taken from Ref. [74, 76].

The transfer probabilities were calculated from the amplitude as the sum of probability

of each final channel. The probability for a given transfer channel is proportional to the square of the form factor times a term (adiabatic cut-off function described in Chapter 1.2.1) that depends on the optimum Q-value of the reaction:

$$P_\beta(\ell) = \sum_{m_1', m_1} \left| c_\beta(\ell) \right|^2 \sim [f_{\lambda 0}(D_l) g(Q_{opt})]^2. \tag{1.15}$$

For the one-neutron transfer channel, the inclusive cross section can be obtained by summing up all the contributions coming from the single particle transitions.

To calculate the amplitude for the transfer of two nucleons one has to perturbatively solve the well-known system of semi-classical coupled equations up to the second-order DWBA approximation:

$$c_\beta(\ell) = \left(c_\beta\right)_{(1)} + \left(c_\beta\right)_{\text{ort}} + \left(c_\beta\right)_{\text{succ}} \approx \left(c_\beta\right)_{\text{succ}}, \tag{1.16}$$

where the first term describes the simultaneous transfer of the pair of nucleons, the second term arises from the non-orthogonality of the channel vectors, and the last term describes the successive process via an intermediate channel. In calculations for two-nucleon transfer, only transitions to 0^+ states are included. Due to cancellation of the orthogonal and simultaneous part, only the successive term was used.

The transfer probability for a specific single-particle transition, is calculated from Equation 1.15.

The single-particle states used to calculate the (1n) transfer cross section cover a complete shell below the Fermi level for ^{96}Zr and a complete shell above for ^{40}Ca, with spectroscopic factors set to one, are shown as an example for the ^{96}Zr + ^{40}Ca in Fig. 1.16. The calculated total transfer probability is shown in Figure 1.15 with a full line.

The agreement between calculated results and the experimental data is very good, both in terms of magnitude and slope, which is expected since the one-neutron transfer form factors incorporate experimental single-particle energies. The calculations for (1n) are plotted in Fig. 1.15 with the full black lines. It can be concluded that the calculation describe well the experimental data in the whole range of d, indicating the correctness of the chosen set of single particle levels.

The transfer of two neutrons, as discussed above, was applied, only to the $J = 0^+$ states. The ground-state wave function for ^{94}Zr is obtained from a BCS calculation (described in Chapter 1.3.2) by adopting the single-particle states and a state-independent pairing

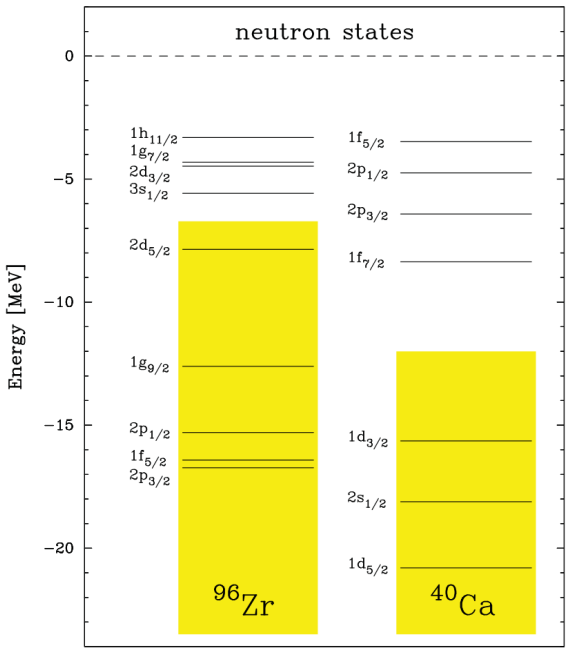

Figure 1.16: Neutron single-particle levels in ^{96}Zr and ^{40}Ca which are used in BCS calculation. Figure is taken from Ref. [74].

interaction $G = 0.218$. A pairing gap of $\Delta = 0.746$ MeV is achieved with a Fermi energy of 7.6523 MeV.

For the description of ^{42}Ca, the two-body interaction is added as a perturbation to the single particle states. The model includes only a two-particle configuration coupled to 0^+. The resulting 0^+ states are located at energies of 0, 5.76, 9.10, and 11.96 MeV. In Fig. 1.15 on the left panel (^{96}Zr and ^{40}Ca), the calculated probability for (2n) for the ground-ground state transition only is shown with a dotted line. Clearly, the total transfer strength does not receive enough contribution from this transition only. Because of that, the contribution from the transition to the 0^+ state at 5.76 MeV in ^{42}Ca is added. The calculation, with the higher 0^+ state at 5.76 MeV included, represented by a dashed line, described the data much better.

On the other hand, for the well Q-value matched ^{60}Ni+^{116}Sn system, only the ground to ground state transition was included in the successive approximation. One can observe a very good agreement between the experimental points and theory (full red line) both in magnitude and slope. This indicate that the two-neutron transfer channel in this system primarily populates the ground state.

This fact was checked in additional particle-gamma coincidence experiment (empty points

in Figure 1.15). The γ spectra corresponding to the inelastic, one, and two-neutron transfer channels were extracted, and it was demonstrated that for two-neutron transfer channel approximately 76% of the total strength goes to ground-to-ground state transition. The probabilities for pure neutron transfers align well with previous results (full points in Figure 1.15).

Also, for the ^{94}Zr+^{42}Ca reaction, γ-fragment coincidences were measured [78], and the level schemes for ^{42}Ca and ^{94}Zr nuclei were constructed. An analysis of the strength distribution reveals that the transfer probability for the transition to the excited 0^+ state in ^{42}Ca, whose wave function is dominated by the two neutrons in the $2p_{3/2}$ shell, is much larger than the ground-state one. By considering only transitions to the 0^+ states, the experimental cross section was still under-predicted by a factor of $\sim$3. This was attributed to transitions to states with large angular momentum and states of non-natural parity, suggesting the need to consider more complex two-particle correlations in the transfer process.

An interesting and almost unexplored issue is whether and to what extent the effect of nucleon-nucleon correlations in the evolution of the reaction is modified in the presence of high Coulomb fields. In fact, in the collision among very heavy ions, the population of final states with high excitation and angular momenta and/or multi-step processes may significantly change the transfer strength of the ground to ground state transitions. Because of that the ^{206}Pb+ ^{118}Sn, heavy asymmetric semi-magic system, were studied in this thesis.

The system, ^{206}Pb+^{118}Sn, has already been studied previously [79–81]. The authors of Ref. [79–81] extracted the enhancement by comparing (1n) and (2n) channels. This measurements were performed by using the particle-gamma coincidence detecting techniques.

In that measurement the cross-section for two-neutron transfer was obtained through the excitation of the low-lying 2^+ state in Sn (and without γ-decay feeding), with Pb in the ground state. This was then compared to the transfer to the strongest one-neutron transfer transitions in ^{205}Pb + ^{119}Sn. The experimental result for the transfer probabilities, $P_{\rm tr}(d_0)$, are shown in Figure 1.17, together with the semi-classical model predictions. Significant enhancements, $EF \gtrsim 900$, have been extracted.

In our experiment, we chose a different setup and we measured in a larger range of the distance of closest approach (d), up to the larger distances which correspond to energies

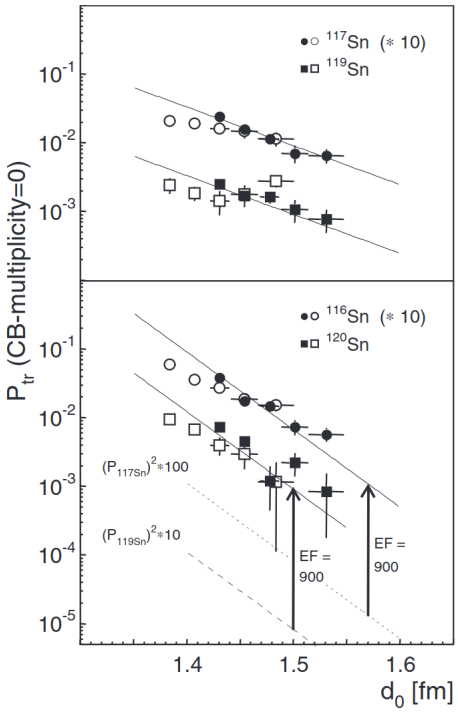

Figure 1.17: The one-neutron (up) and two-neutron (down) transfer probabilities in ^{206}Pb + ^{118}Sn collisions as a function of the parameter d_0. Filled symbols refer to a bombarding energy of 5.14 MeV/u, while open symbols represent 5.32 MeV/u. The nuclei are identified by their characteristic γ-transitions. In the lower part of the figure, the squared values of the calculated and measured one-neutron transfer probabilities are drawn as broken lines. The shift observed between the square of the one-neutron transfer probability and the corresponding two-neutron transfer probability defines the enhancement factor EF.[56, 79, 81]

below the barrier. Whereas in the previous experiment they had particle-gamma coincidences, in our case we only have particle identification. What we wanted to obtain from the experiment is the enhancement factor (EF), which includes the transitions from the ground state to the ground state in both one-particle and two-particle transfer reactions (inclusive cross-sections). On the other hand, the isolated events observed in the previous experiment accounted for only a minor portion of the total inclusive cross-section for two-particle transfers. Consequently, this makes direct comparison of the results challenging. We assumed that the transition from ground state to ground state is dominant at energies below the barrier for both heavy and light partners, especially at energies far below the barrier (larger d). In fact, one expects that the Q-value spectra will become narrower, with centroids closer and closer to the ground-to-ground states.

In contrast to the large EF value obtained, in the ^{208}Pb + ^{144}Sm reaction, which was performed using the magnetic spectrometer [82], revealed significantly different enhance-

ments. For neutrons the enhancement was not observed, $EF \approx 1$, while for protons it was $EF \approx 8$. In these considerations, one also has to take into account the different structure of participating nuclei. Some of them are close to the neutron magic numbers, while the other have open neutron channels.

1.3.2 Theory of pairing correlation

Cooper pairs are the building blocks of pairing correlations in fermionic many-body systems. In particular, the nuclear superfluidity can be studied quantitatively. To achieve this one must be able to predict absolute differential cross sections using information about nuclear structure and dynamics, which can be directly compared with experimental observations [83].

In the transfer of two nucleons in heavy ion reactions, they can be transferred successively ("one after the other") or simultaneously (as a "pair"). Since the correlation length (see later) can be larger than the sum of the target and projectile radii [56], regardless of the fact that successive process is dominant, nucleons can be correlated.

The pairing correlations can be accurately described theoretically with models which are derived from the Bardeen-Cooper-Schrieffer (BCS) theory. In the BSC theory [84], the wave function for even-even nuclei is given by:

$$|\mathrm{BCS}\rangle = \prod_{k>0} \left(u_k + v_k a_k^+ a_k^+\right) |0\rangle. \tag{1.17}$$

For each state $k > 0$ in the configuration space, there exists a "conjugate" state $\bar{k} < 0$, and $(k, \bar{k})$ generates the whole single-particle space. The operator a^+ is a raising operator. Parameters v_k^2 and u_k^2 represent the probability of occupation of certain pairs $(k, \bar{k})$:

$$\left.\begin{matrix} u_k^2 \\ v_k^2 \end{matrix}\right\} = \frac{1}{2}\left[1 \pm \frac{\epsilon_k - \lambda}{\sqrt{(\epsilon_k - \lambda)^2 + \Delta^2}}\right]. \tag{1.18}$$

If a constant residual interaction is assumed, the following Hamiltonian is obtained:

$$H = \sum_{k>0} \varepsilon_k a_k^+ a_k - G \sum_{kk'>0} a_k^+ a_{\bar{k}}^+ a_{\bar{k}'} a_{k'}. \tag{1.19}$$

The parameter G represent the pairing strength, which can be determined by adjusting the calculated pairing gaps Δ to empirical pairing gaps:

$$\frac{2}{G} = \sum_{k>0} \frac{1}{\sqrt{(\epsilon_k - \lambda)^2 + \Delta^2}}. \tag{1.20}$$

In the absence of pairing ($G \to 0$), the energy gap becomes zero ($\Delta = 0$) and the probability

for occupied levels is $v_k^2 = 1$, while for unoccupied levels it is $u_k^2 = 0$. Therefore, a step function can be formed by v_k. When pairing exists ($G \neq 0$), the energy gap does not vanish ($\Delta \neq 0$) and v_k assumes a distributional form (see figure 1.18).

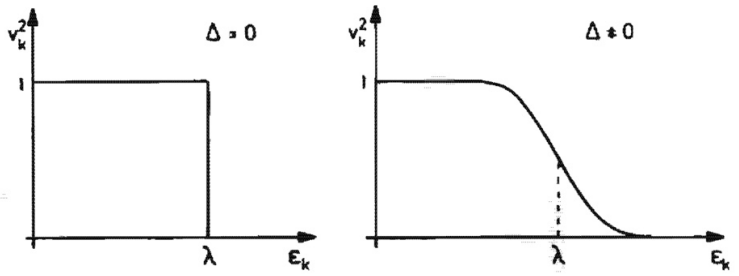

Figure 1.18: The occupation probability for interacting and non-interacting case.[84]

In figure 1.19 distributions of nucleons ($2 \leq n \leq 26$) over the five orbitals are shown. one can observe that with an increasing number of nucleons, the distribution function becomes less step-function-like.

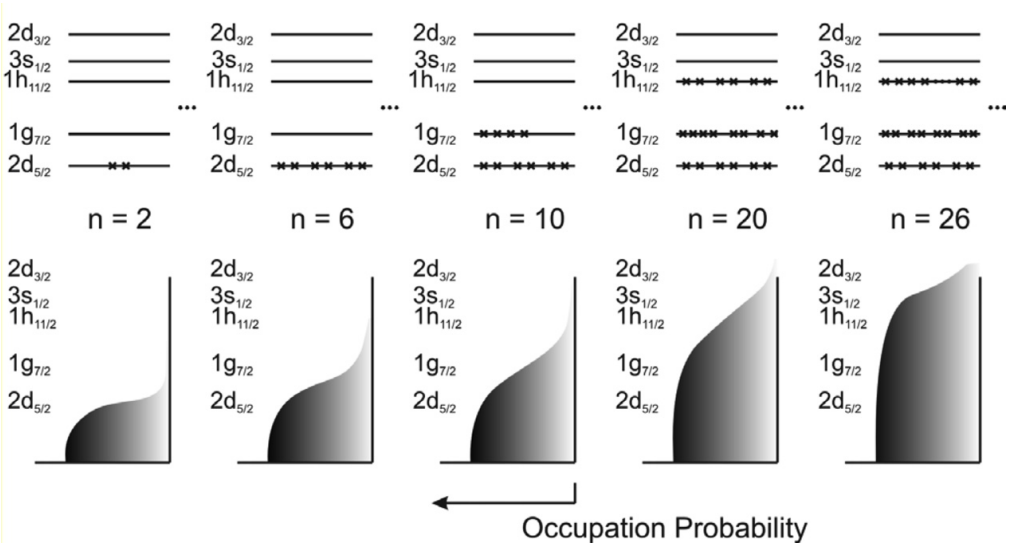

Figure 1.19: The occupation probability for different numbers of the nucleon.[55]

In the special case, where there is a single j-shell all ϵ_k are the same thus all v_k are the same as well, the gap is given as a function of the particles:

$$\Delta = G \cdot \sqrt{\frac{N}{2}\left(\Omega - \frac{N}{2}\right)}, \tag{1.21}$$

where Ω is the maximum number of pairs in one shell.

The binding energy of the pairs ($\approx 2\Delta$) is maximum when the orbital is half filled ($N = \Omega$). In this case $2\Delta = G\Omega$.

In more complicated cases where there are n-particles with seniority ν (the number of unpaired nucleons), in the shell j the general expression for the spectrum of the pairing Hamiltonian is given:

$$E_v(n) - E_0(n) = \frac{G}{4}\nu(2\Omega - \nu + 2). \tag{1.22}$$

It can be observed that the energy difference remains independent of n. In figure 1.20, the spectrum for a pure pairing force (G set to 0.25) within the $h_{11/2}$ orbital is shown, with seniority values of $\nu = 0$, $\nu = 2$, $\nu = 4$, and $\nu = 6$, as a function of the particle number n.

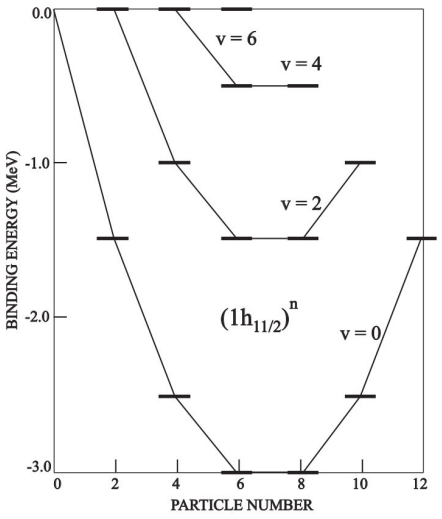

Figure 1.20: Spectrum for a pure pairing force (G set to 0.25) within the $h_{11/2}$ orbital with seniority $\nu = 0$, $\nu = 2$, $\nu = 4$, and $\nu = 6$ as a function of the particle number n [84].

The authors of the Ref. [77] have proposed a method by which the correlation length can be deduced from experimental data. They compared the transfer probabilities for one and two neutron transfer and observed where they have similar values. They used the following distance of closest approach to extract the correlation length of the Cooper pair ξ:

$$\xi = \frac{\hbar v}{\pi \Delta}. \tag{1.23}$$

This prescription was applied for the ^{60}Ni+^{116}Sn system where the correlation length was estimated to be $\xi \approx 13.5$ fm. The obtained value is about 30 percent larger than the sum of radii (calculated using standard formula $R_i = 1.2 \cdot (A^{1/3} - 0.9)$ fm), which indicates that

the two nucleons are correlated at relatively large distances.

By using the Eq. 1.23, and by, including the Δ which correspond to ^{206}Pb and ^{118}Sn nuclei [85], we estimated the correlation length of $\xi \approx 15$ fm. This of course will have to be compared with the transfer probabilities in the ^{206}Pb+^{118}Sn system, where we will search for region in distances of closest approach where P_{tr}(1n) is close to P_{tr}(2n). The study of ^{206}Pb+^{118}Sn system could provide key insights into nucleon correlations, offering a clearer picture of nuclear interactions in heavy-ion collisions.

2 The ^{206}Pb+^{118}Sn experiment

The ^{206}Pb+^{118}Sn system was selected for the purpose of investigating pairing correlations through the measurement of the excitation function both above and below the barrier. Additionally, the choice was influenced by Q-value considerations, which enable the simultaneous population of ±n and ±p channels. This allows for the observation of the dynamics' evolution by examining the differential and total cross sections, as well as the energy distribution for the lighter partner. Lighter reaction products were detected and identified by the large acceptance magnetic spectrometer PRISMA [86].

The inverse kinematic configuration was chosen because the target-like recoils entering PRISMA should have sufficient kinetic energy to be detected with a good resolution. As an example in Fig. 2.1 the result of GRAZING calculations are shown for beam energy 1200 MeV in the laboratory system (that is 687 MeV in the center of mass system), for the (+1n) channel in inverse (top) and direct (bottom) kinematics for light (red) and heavy (black) partner. On the left side one can observe that the the angular distributions in the inverse kinematics are more focused, so more statistics can be obtained. This is particularly important when we want to observe channels with a small cross-section, such as the channel of pick-up and stripping of two nucleons, which will be especially interesting for studying pairing correlations. The cross-sections of these channels further decrease at energies below the barrier. On the right side calculated kinetic energies are shown. One can observe that, at the grazing angle, in inverse kinematics (which is at ∼35°) with $E_{kin} \sim 6.1$ MeV per nucleon, while in the direct kinematics, at the grazing angle (which is at ∼72°), we have $E_{kin} \sim 2.4$ MeV per nucleon. The higher kinetic energy of the reaction products is particularly important in heavy systems, like the one we are studying in this thesis, where it is more difficult to achieve good resolution of the final mass spectra.

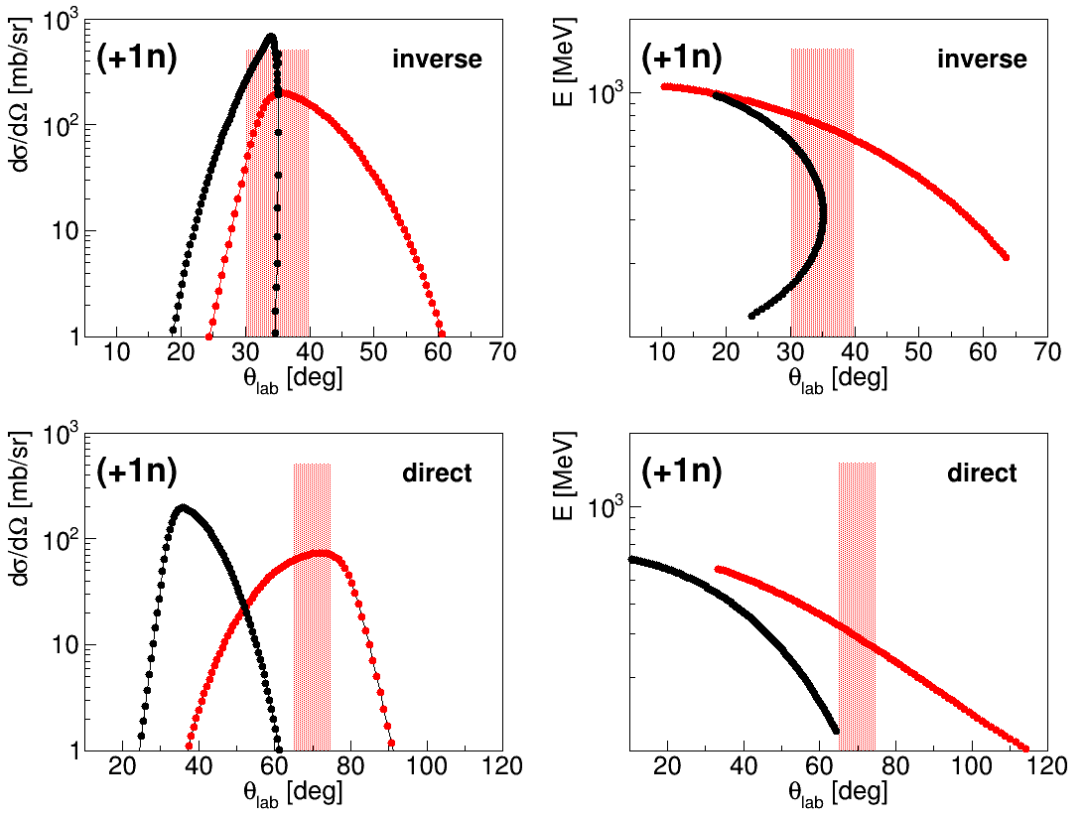

Figure 2.1: GRAZING calculations for inverse (top) and direct (bottom) kinematics for the light (^{119}Sn) partner in red and the heavy (^{205}Pb) partner in black, for $E_{lab} = 1200$ MeV ($E_{cm} = 687$ MeV). The left side shows the angular distributions, while the right side shows the calculated kinetic energies. The shaded part indicates the angular acceptance of PRISMA.

In this experiment, the 2-pnA ^{206}Pb beam was used for the first time at the INFN-LNL facility, which was also the heaviest beam used at LNL up to that time (later in 2021, the ^{208}Pb beam was used). The beam was delivered by the PIAVE positive ion injector, followed by the ALPI post-accelerator of the LNL, onto a 200 μg/cm^2 (2-mm strip) ^{118}Sn target. Measurements were performed for an excitation function at three different bombarding energies, $E_{\rm lab} = 1200$, 1090, and 1035 MeV, which corresponds to the 5.8-5.0 MeV per nucleon. For the highest energy, PRISMA was first placed close to the grazing angle at $\theta_{\rm lab} = 35°$ and then at 25°.

For the lower bombarding energies, the PRISMA angle was fixed at 25° because below the barrier the angular distributions of the transfer channel peak at forward angles in the laboratory frame (backward angles in the center of mass reference frame). In Figure 2.2 GRAZING calculations for (+1n) channel are shown for different beam energies (1200, 1090 and 1035 MeV). PRISMA acceptance is marked for two different angle configurations

used in experiment (θ_{lab}=25° and 35°). It can be concluded that the distribution becomes flatter and the peak moves to the forward angles when decreasing the beam energy.
At the highest energy, we chose two angles that allowed us to observe the evolution of the reaction and the transition from the quasi-elastic to deep inelastic regime. Also, due to the shape of the angular distribution at the highest energy (shown in Figure 2.2), we were able to obtain total cross-sections by integrating angular distributions. Lower energies, especially those below the barrier, were of particular interest as they are suitable for studying pairing correlations.
Inside the scattering chamber sliding seal two silicon surface barrier type monitor detectors were placed at $\theta_{\text{lab}} = 48°$ and 58°. The monitors were used to detect Rutherford scattered Sn ions for relative normalization between different runs and to control the beam conditions during the measurements.

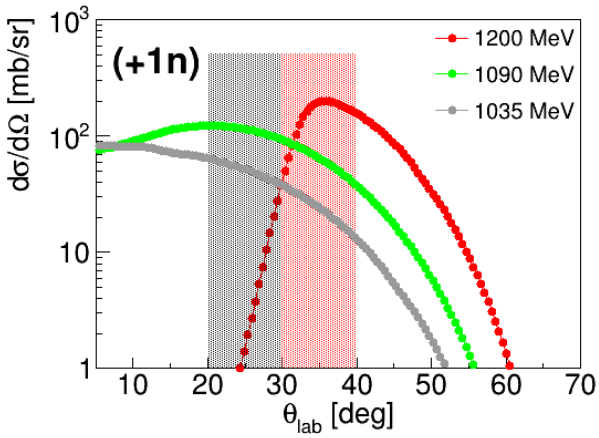

Figure 2.2: GRAZING calculations of angular distributions for the light (^{119}Sn) partner for different beam enegries 1200 (in red), 1090 (in green) and 1035 MeV (in gray). The shaded parts indicate the angular acceptance of PRISMA.

The kinematics of the reaction is shown in Fig. 2.3 for the highest measured energy, E_{lab}= 1200 MeV along with the calculated Rutherford scattering for both fragments. One observes the events both at high β, corresponding to the target-like ions, and at lower β, corresponding to the beam-like ions. The kinematics of the reaction and the chosen geometry of the experiment led to the fact that some of the beam-like ions also entered the spectrometer, which can be used to monitor the experiment. It can be observed that the events involving beam-like ions bend towards an angle close to 35°, which is the limiting angle for Pb determined by the kinematics. Comprehensive control of the kinematic conditions was important for monitoring the beam energy and the set magnetic

field of the spectrometer.

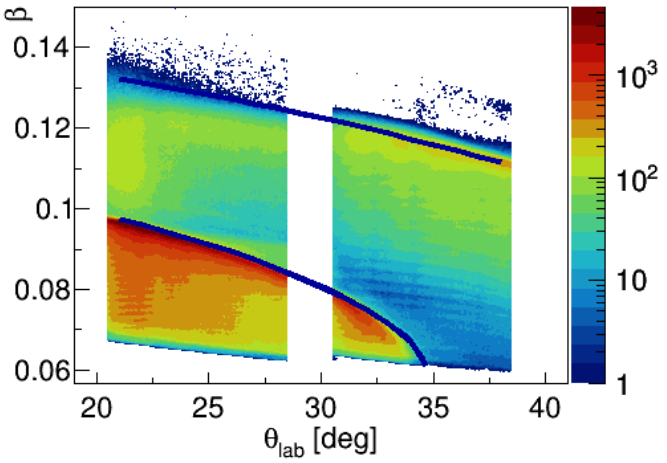

Figure 2.3: Matrix of velocity ($\beta = v/c$) vs in-plane scattering angle (θ_{lab}), obtained by merging the measurements performed with the two PRISMA angular and magnetic settings for $E = 1200$ MeV. The events at large and low β correspond to Sn-like and Pb-like ions, respectively. The blue curves correspond to the calculated Rutherford scattering for both fragments.

Further details about the components of the experimental setup and each detector will be discussed in the following chapter.

3 Experimentl apparatus

In this chapter, we will discuss the experimental apparatus, specifically concentrating on the PRISMA detectors: Micro Channel Plate (MCP), Multi-Wire Parallel Plate Avalanche Counter (MWPPAC), Ionization Chamber (IC), and the optical elements. These were used for ion (Z), mass (A) and charge state (Q) identification, as well as for kinetic energy calculation of the reaction products.

3.1 The PRISMA spectrometer

PRISMA is a large acceptance magnetic spectrometer, designed for the detection of low-energy, medium-mass reaction products (5-20 MeV/A) in heavy-ion collisions around the Coulomb barrier. The name PRISMA is inspired by the functionality of an optical prism, which splits white light into its constituent wavelengths. Similarly, PRISMA sorts incoming ions based on their magnetic rigidity.

PRISMA covers a wide solid angle of 80 msr. It is capable of measuring the mass of ions with $30 < A < 200$ u, achieving a resolution of $\Delta A/A < 1/300$. The energy resolution, determined via Time of Flight (TOF), is $\Delta E/E < 1/1000$, and the charge resolution is approximately $\Delta Z/Z \sim 1/80$. This spectrometer can handle an event frequency of up to 100 kHz. Figure 3.1 illustrates the schematic layout of the magnetic spectrometer PRISMA along with the corresponding photo, when PRISMA was coupled to the CLARA γ array.

Detection is carried out using MCP (Microchannel Plate) detector [87], MWPPAC (Multi-Wire Parallel Plate Avalanche Counter) detector [88], ionization chambers (IC) [88] and two magnetic elements to focus and disperse (quadruple singlet and dipole magnet). A set-up like this enables the determination of ion positions (X,Y) at the entrance and the

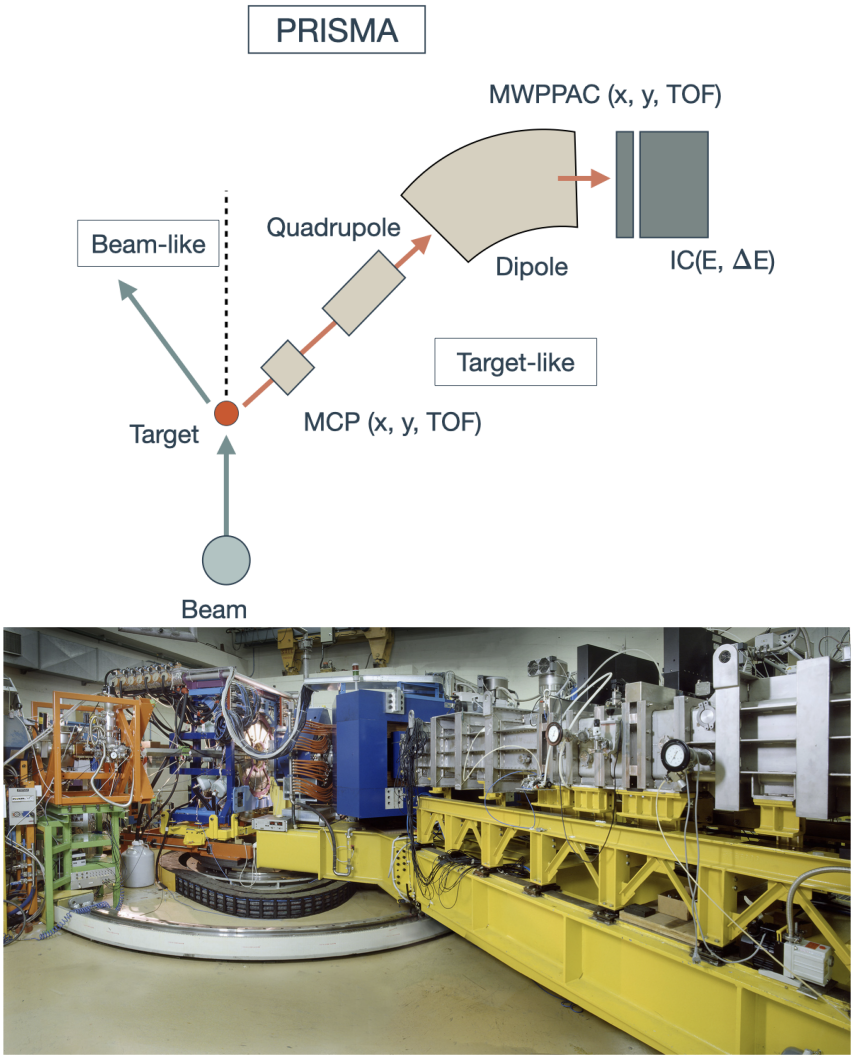

Figure 3.1: Schematic layout (top) and corresponding photo (bottom) of the PRISMA magnetic spectrometer when was coupled to CLARA γ array. The position of the detectors (MCP, MWPPAC and IC) in PRISMA and the physical quantities obtained with them, as well as the position of the magnets (quadrupole and dipole) are indicated in schematic layout.

focal plane, time of flight ($TOF = t_{MCP} - t_{PPAC}$), kinetic energy (E), and energy loss (ΔE). After the event-by-event trajectory reconstruction, it is possible to identify the atomic number Z, charge state q and mass number A of each reaction product.

3.1.1 Micro Channel Plate (MCP)

The entrance detector of PRISMA, a Micro-Channel Plate (MCP) detector, is positioned 25 cm away from the target. It's used to provide information for the timing and position of particles in both the X and Y directions, going along and across the dispersion plane. The position at PRISMA, the schematic layout, and a photo of the detector can be seen

in Fig. 3.2.

It is positioned between the target and the quadrupole magnet of PRISMA, and it covers the whole solid angle of the spectrometer.

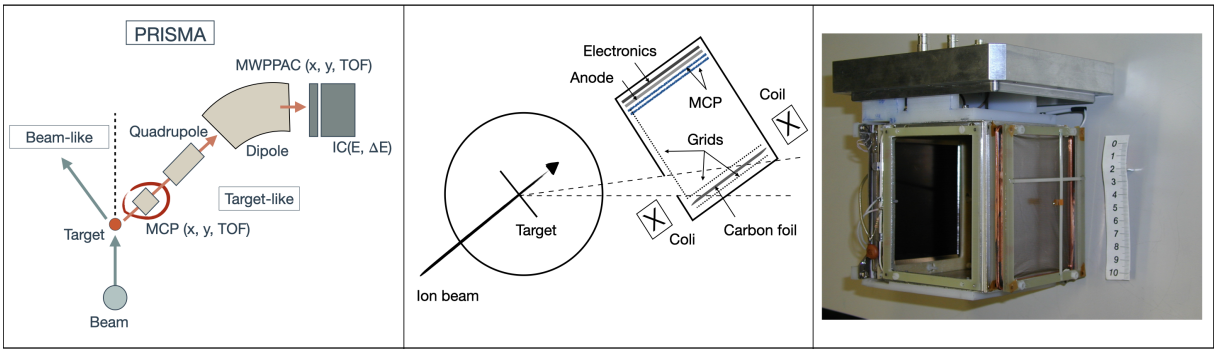

Figure 3.2: The position at PRISMA (left), schematic layout (center), and photo (right) of the MCP detector. At the schematic layout, parts of detector are denoted: carbon foil, two MCPs, anode, electronics and two external coils.

The large detection area (80x100 mm^2) functions as an electron multiplier network. As reaction products traverse the 20 $\mu g/cm^2$ thin charged carbon foil, ionization prompts a cascade of secondary electrons that get amplified and detected by a sensitive anode. Spatially sensitive anodes detect the generated charge, providing x_{MCP} and y_{MCP} coordinates at a given time. A magnetic field, applied by an external coil (120 Gauss) positioned midway between the carbon foil and the MCP, is used to preserve position information. This field aligns parallel to the accelerating electric field. The broad detection area, combined with high spatial (1 mm) and timing (approximately 300 ps) precision, complemented by a high event recording frequency, ensures detection efficiency of heavy ions up to 100%. Because it can handle a high number of counts the detector could be installed close to the target, where there is normally a very high background due to d-electrons, X-rays and light charged particles.

3.1.2 Optical elements

Optical elements include the quadrupole singlet and the dipole magnet, used to focus and disperse the trajectories of reaction products.

The quadrupole magnet, positioned 50 cm away from the target, focuses the reaction products into the vertical direction (Y) and defocuses in horizontal direction (X).

Placed 60 cm from the exit window of the quadrupole, the dipole magnet guides the

trajectories of the reaction products into the focal plane detectors based on their magnetic rigidity. The dipole magnet itself is characterized by a bending angle of 60 degrees for the central trajectory, a bending radius (radius of curvature) of 1.2 m for trajectories along the optical axis, the maximum magnetic field of 1 T, and a maximum magnetic rigidity ($B\rho$) of 1.2 Tm.

3.1.3 Multiwire Parallel-Plate Avalanche Counter (MWPPAC)

The MWPPAC is a gas detector with extensive dimensions measuring 100x13 cm^2. With the MWPPAC, it becomes possible to measure both the position of ions on the focal plane, as well as the time t_{PPAC}. The Time of Flight (TOF) is determined as the time difference between the sections of the MWPPAC (start) and the delayed signal from the MCP (stop). The choice of using the MCP detector as the stop and the MWPPAC as a start detector aims to increase the signal-to-noise ratio. The signals need to be calibrated to obtain accurate timing information in nanoseconds (as described in 4.1.3).
In Figure 3.3, one can see the MWPPAC detector's position in PRISMA (left), its schematic layout (center), and a photo (right).

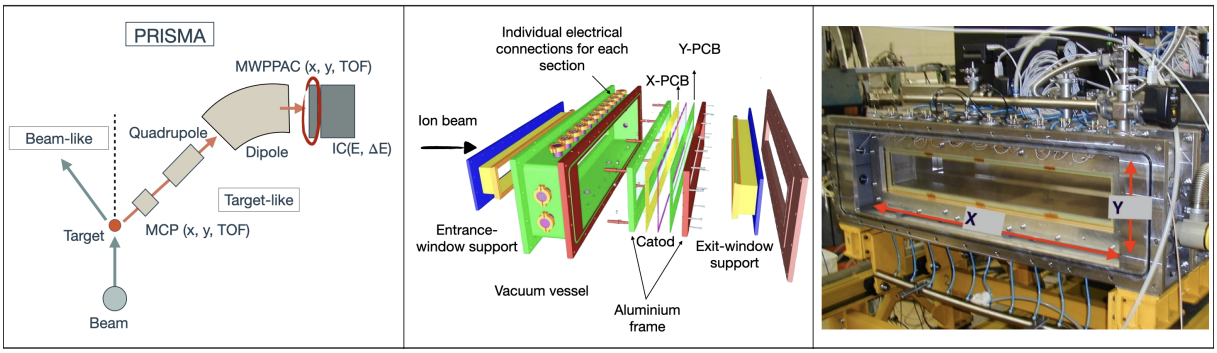

Figure 3.3: The position at PRISMA (left), schematic layout (center), and photo (right) of MWPPAC detector. At the schematic layout, parts of detector are labeled: entrance window, vacuum vessel, aluminum frames, aluminum X printed-circuit board, Y printed-circuit board, cathode, exit window, individual electrical connections for each section

The MWPPAC detector is an avalanche counter type of detector, where a high voltage is applied across the electrodes, which creates an electric field in the detector. When a charged particle passes through the detector, it produces a burst of electrons. These electrons are accelerated by the electric field and produce an avalanche of secondary electrons.

The MWPPAC detector consists of three electrodes: a central cathode for timing and signal reconstruction, also two grounded position anodes in the X (horizontal) and Y (vertical) planes. The OR of the cathode signals is used as a master trigger for the data acquisition system. The horizontal length of the detector is divided into 10 sections so that each section contains 100 anode wires spaced 1 mm apart. The vertical axis is made of a single section over the entire length (1 m) with a 1 mm wire step, in groups of two with a 2 mm position resolution. Each section has a three-electrode structure: a central cathode polarized at high voltage (500-600 V) for timing and two orthogonal wire planes, placed at ground potential at 2.4 mm from the cathode, which provides X and Y position information. The whole detector volume is in the active gas (isobutane C_4H_{10}), with pressures of about 7–8 mbar. This detector has a resolution of 1 mm for x_{PPAC}, 2 mm for y_{PPAC}, ≈350 ps for t_{PPAC}, and counting rates as high as 100 kHz.

3.1.4 Ionization Chamber (IC)

The focal plane MWPPAC detector is followed by an Ionization Chamber (IC), 72 cm downstream of the MWPPAC. It is used to measure the kinetic energy of the ions and their energy loss. The volume of the detector is 100×13×120 cm^3 (width×height×depth, respectively). It is divided into 40 anode pads, 10 sections in the horizontal direction and 4 in the depth of the chamber.

The figure Fig.3.4 shows the position in PRISMA (left), a schematic layout (center) and a photo (right) of the IC.

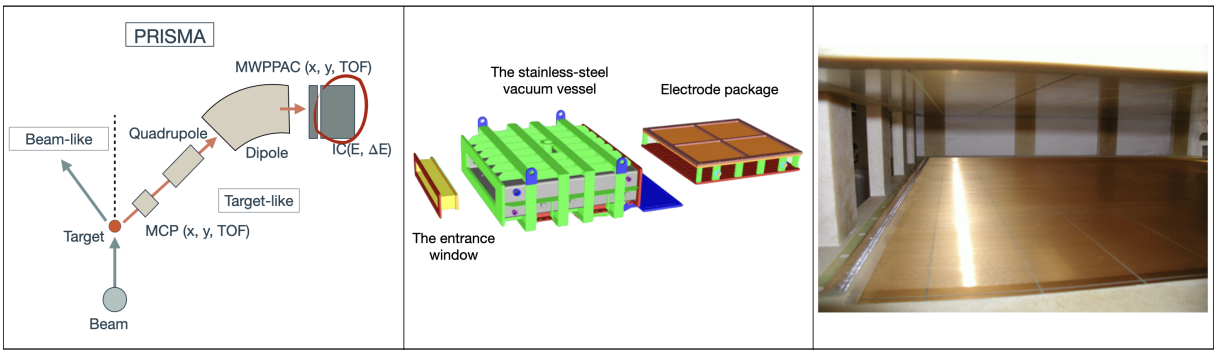

Figure 3.4: The position at PRISMA (left), schematic layout (center), and photo (right) of the ionizaton chamber. At the schematic layout, parts of detector are denoted: electrode package, the stainless-steel vacuum vessel and the entrance window.

IC operate in transverse mode, where the electric field in the chamber is perpendicular

to the direction of the charged particles. The charged particles pass through the chamber and ionize the gas, producing electron-ion pairs. The amount of electrons is proportional to the energy of the particle.

In this experiment, the IC was operated with freon CF_4, but methane CH_4 can also be used. The stopping power of freon and long depth of IC make it possible to stop target-like ions at relatively low working pressures (35-40 mbar). The low pressure is important to reduce the stress on the entrance window, which is designed for a working pressure of up to 100 mbar. At left and right edges of IC, additional veto pads are place in order to exclude ions which were not fully stopped (i.e. their kinetic energy would not be correctly reconstructed). The total energy (E) is reconstructed as a sum of all energy losses in pads of the IC depth, while the energy loss (ΔE) is taken as a sum of loss in the first, or in the first and second pads.

The large dimension of the IC, the possibility to combine subsections in different ways, the selection of the gas and the adjustment of the gas pressure allow the identification of ions that differ in their kinetic energy by more than 20%. By optimizing all these parameters, not only a good Z resolution but also an energy resolution of $\sim$1-2 MeV could be achieved.

In the next chapter, the process of deriving physical quantities from the collected data will be explained. The data analysis procedures will be detailed, including the calibration of each detector and the outlining of steps for extracting ion identification from data. Lastly, the construction of mass spectra for each reaction product will be described.

4 Data analysis

In this chapter, the steps of the data analysis are presented, from the raw data to the final spectra of physical quantities. Calibration of position and TOF, trajectory reconstruction, and identification of nuclear charge and atomic charge state are described.

4.1 Calibration of PRISMA detectors

4.1.1 MCP calibration

The correct calibration of the MCP detector is necessary to obtain the correct position information (x, y) of the incoming ion. Figure 4.1 on the left displays the matrix of raw positions (Y vs. X) on the MCP as provided by an acquisition system. The five reference points are marked with numbers from 0 to 4. These marks are visible due to the OR of the cathode signals of MWPPAC being used as a master trigger for the data acquisition system.

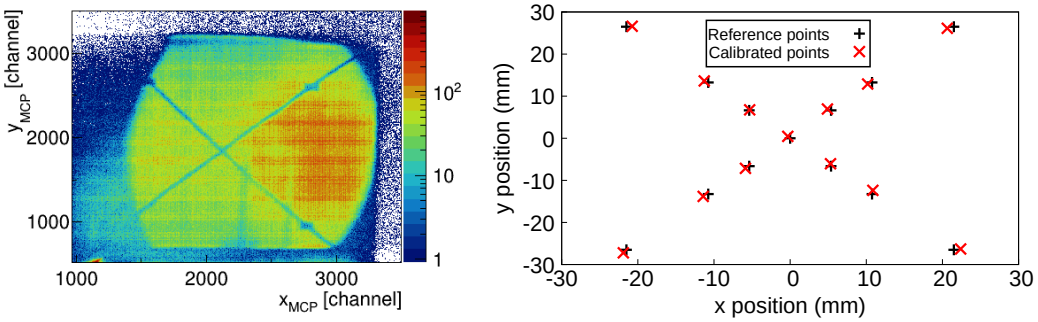

Figure 4.1: Matrix of the y vs. x position of MCP detector given in raw format, in channels (left) and calibration plot with reference and calibrated points (right).

The calibration procedure is performed with a calibration of the X and Y coordinates to

account for possible deformations of the surface, using the matrix method described in Ref. [87]. The final matching can be seen on the right side of Fig. 4.1.

The final plot of the calibrated MCP in Cartesian coordinates is shown on the left side of Fig .4.2. After spatial calibration, the coordinates can be converted to angular ones. The angular coordinates are important to construct angular distributions of the reaction products. The final plot of the calibrated MCP in spherical angles (θ, ϕ) is shown on the right side of Fig. 4.2.

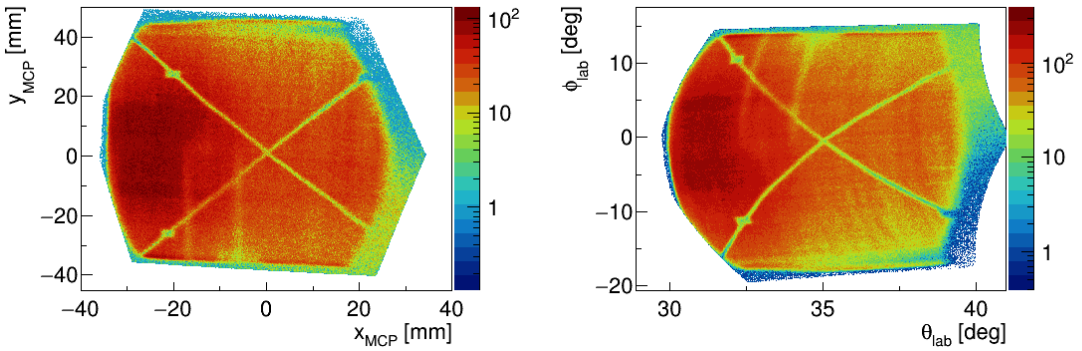

Figure 4.2: Matrices of the calibrated MCP detector in Cartesian (left) and angular (right) coordinates with coincidence with the focal plane detector MWPPAC.

4.1.2 MWPPAC calibration

The MWPPAC detector consists of 10 sections and each of them provides six raw signals, 4 signals for the position (left x_l, right x_r, top y_u and bottom y_d), a signal from the cathode x_c and a timing signal (for the TOF).

From the combination of the signals x_l and x_r the position x_{fp} of the detected ions in the focal plane can be determined:

$$x_{fp} = x_r - x_l. \tag{4.1}$$

If either signal is completely or partially missing, it can be reconstructed from the cathode signal. Thus, in an ideal detector, the matrix of the sum of signals $x_l + x_r$ vs. the signal x_c shows a simple point structure, but in a real detector, the two anodes may collect less charge than the cathode and the matrix shows vertical structures extending towards lower values of $x_l + x_r$. The associated events were not rejected, but recovered by a simple calibration procedure in which the cathode signal is related to the right and left signals, respectively. The focal plane position x_{fp} for each section could then be calibrated to

millimeters using a first order polynomial of the ADC signals in channels. Also, the two central wires of each section are short-circuited for calibration purposes. Therefore, the two central channels of each pad should be about twice or half the counts of the other channel, which can be observed in Fig. 4.3. The final spectrum of the calibrated focal plane position is shown in Fig. 4.3. One can see the full length (100 mm) of the detector constructed from different sections.

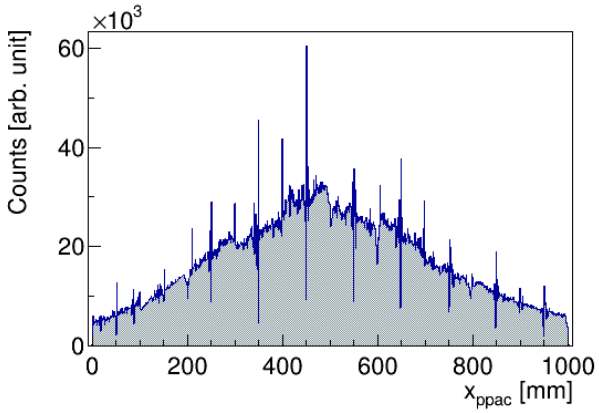

Figure 4.3: Calibrated spectrum of the position in the MWPPAC detector.

4.1.3 TOF calibration

The time interval between the start (at MWPPAC) and stop (at MCP) signals, TOF, is measured using a time-to-digital converter (TDC), which converts the time intervals into a digital value. The TDC is calibrated using a known time interval, in order to accurately measure the TOF of the particle.

The ten separated TOF signals need to be aligned with respect to each other. Therefore, an alignment procedure is required to use the entire MWPPAC as a single detector. The final calibrated and aligned matrix of TOF vs. x_fp is given on the left side of Fig.4.4.

Once the sections were aligned, a global TOF offset had to be set to determine the velocity distributions of the ions. In many previous experiments, PRISMA was coupled with gamma arrays such as CLARA and AGATA, which allowed the offset to be determined with good accuracy from the Doppler shift of gamma rays emitted in flight. In this experiment, no gamma detector was coupled to PRISMA, so the offset was calculated as the ratio between the length of the trajectory in PRISMA ($L \approx 6$ m) and the estimated velocity of the elastically scattered Sn-like ions, e.g., for a beam energy of 1200 MeV and

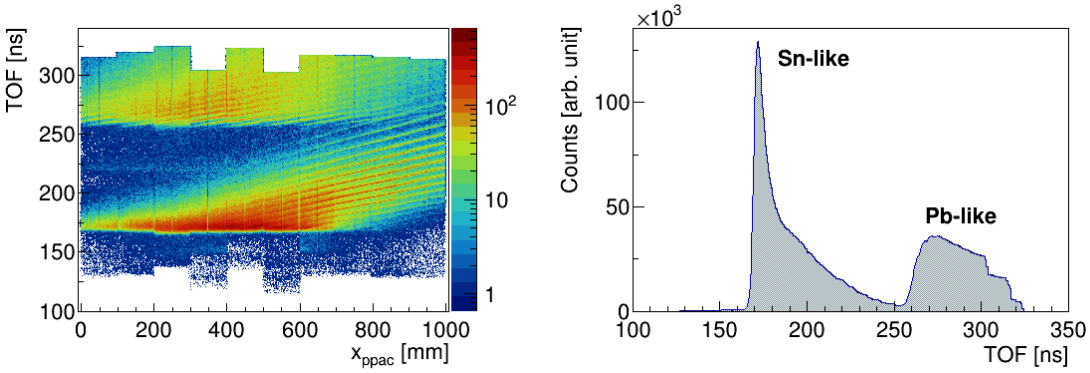

Figure 4.4: Calibrated matrix of the TOF vs. position in the MWPPAC detector (left) and TOF projection.

PRISMA angle 35° the velocity is $v \approx$3.47 cm/ns, so that TOF(^{118}Sn) $\approx L/v \approx$ 173 ns. This is than used as a reference point for the global TOF alignment. On the right side of Fig. 4.4 is the projection of TOF with the global offset included. As can be seen, there is a clear separation between target-like and projectile-like ions.

After this rough estimation, which included all Sn-like ions, the analysis was continued to obtain mass distributions. Following that, this procedure was iteratively performed with a gate solely on the elastic channel.

4.2 Nuclear charge identification

The ionization chamber (described in Section 3.1.4), is used as a $\Delta E - E$ telescope for nuclear charge (Z) identification.

As already described, the anode of the IC is divided into 10 sections which follow the ones in the MWPPAC and each of them is divided in 4 sections in depth, as shown in Fig. 4.5. Each of these 40 sections act as an independent ΔE detector. In addition, side detectors are used to reject events with highly bent trajectories. In more details, if an ion releases an energy higher than a certain threshold inside one of these pads, the event is rejected. Also, events in which the energy loss is not consistent with the reconstructed trajectory are rejected as well. Due to optimization of Z resolution the gas pressure inside IC need to be adjusted for every experiment. Also, adjustment of gas pressure is essential to completely stop the ions in the detector, and to obtain correct energy (E).

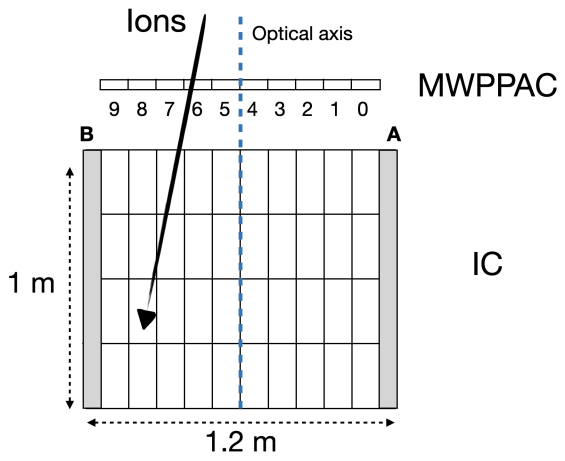

Figure 4.5: Shematic layout of the focal plane detectors of PRISMA. The side pads of the IC are in grey.

The signals from IC are not calibrated to MeV by ADC units. Instead, they are aligned to ensure that the gains of the different sections match. This alignment is usually performed before the experiment. The signals are sent to the 40 pads of the IC with a pulse generator and then the output spectra are analyzed to derive the corresponding coefficients for a linear calibration. The calibration must be performed very precisely, as the Z-resolution must be maintained even after summing the different sections.

The rate of energy loss of a particle passing through a medium is described by the Bethe-

Bloch formula:

$$-\frac{dE}{dx} = 2\pi N_a r_e^2 m_e c^2 \rho \frac{Z}{A}\frac{z^2}{\beta^2}\left[\ln\left(\frac{2m_e\gamma^2 v^2 W_{\max}}{I^2} - 2\beta^2\right)\right], \tag{4.2}$$

where r_e is the classical electron radius $\left(2.817 \cdot 10^{-13}\ \text{cm}\right)$, m_e is the electron mass $\left(9.11 \cdot 10^{-31}\ \text{kg}\right)$, N_a is the Avogadro number $\left(6.022 \cdot 10^{23}\text{mol}^{-1}\right)$, I is the excitation potential, Z is the nuclear charge of absorbing material, A is the atomic mass of absorbing material, ρ is the density of the absorbing material, z is the charge of the incident particle in units of $e, \beta = v/c$ velocity of the incident particle, $\gamma = 1/\sqrt{1-\beta^2}$ and $W_{\max}$ is the maximum energy transfer in a single collision. In the non-relativistic approximation, this formula can be written in the following form:

$$\frac{dE}{dx} \sim \frac{MZ^2}{E}, \tag{4.3}$$

where M is the atomic mass, Z is the nuclear charge of an ion, and E is the energy. Thus, from the above equation it can be concluded that different Z states are distinguished in the matrix dE vs. E, as can be observed in the experimental data.

In Fig. 4.6, the energy ΔE lost by the ions in the first two sections of the IC is plotted against the total energy E released in the IC, for a beam energy of 1200, 1090 and 1035 MeV and PRISMA angles of 25° and 35°. The most intense band corresponds to Sn-like ions. The Pb-like ions can be observed as the straight line ($\Delta E \sim E$). For an angle smaller than the grazing angle (25°), the ions seen at Z $<$ 45 probably correspond to transfer induced fission fragments.

One can observe from 4.6 that in all cases the proton-stripping channels are more populated than the proton-picking channels. Moreover, it can be observed that the strong component of Sn ions (with elastic+inelastic transfer channels) overlap with various proton transfer channels, especially in cases where the beam energy is below the barrier. After analysing these spectra, in this experiment, a Z resolution of about $\Delta Z/Z \sim 1/68$ was achieved [89].

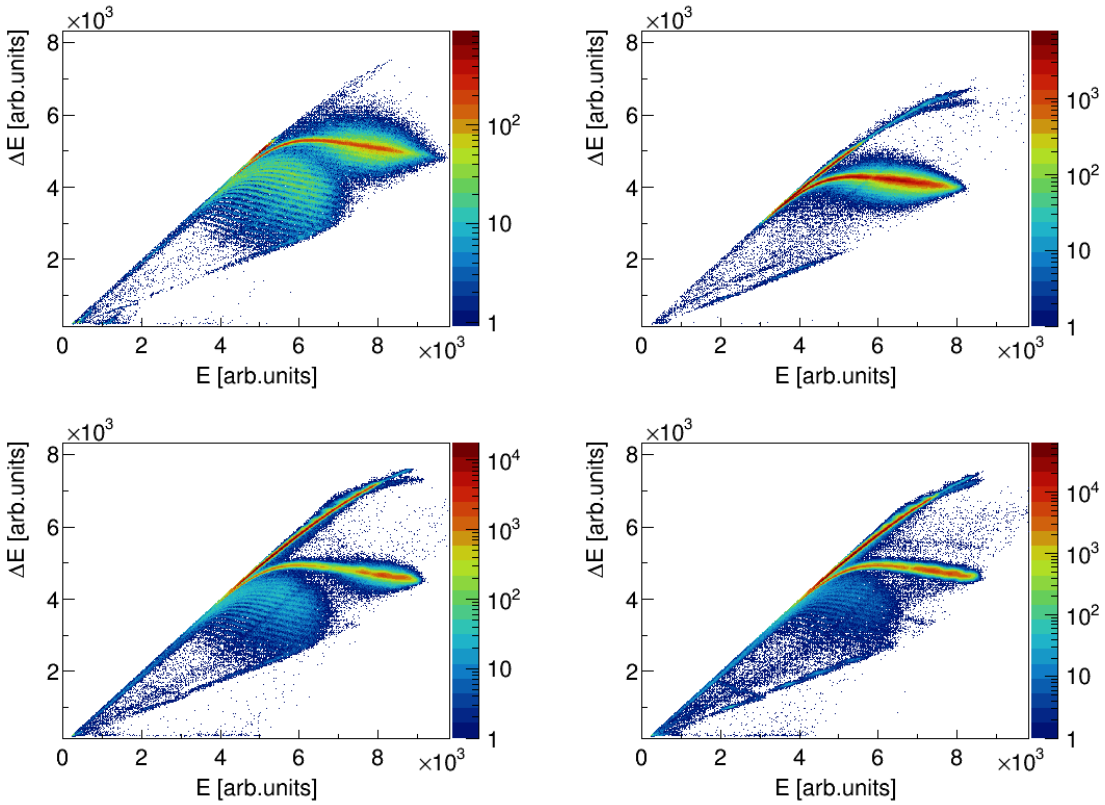

Figure 4.6: Matrices of dE vs. E used for the Z- selection, for beam energy of 1200 MeV (25°) (left-top), 1200 MeV (35°) (right-top),1090 MeV (25°) (left-bottom), 1035 MeV (25°) (right-bottom).

4.3 Trajectory reconstruction

The correct reconstruction of the trajectory is crucial for the complete identification of the ions in terms of atomic charge and mass. The trajectories are calculated by combining the time and position information from the PRISMA detectors with the equations of motion of a charged particle in a magnetic field [90]. After the trajectory reconstruction we are able to calculate the total path length L and the range R of the ions in the IC.

Since we will not use the detailed map of the quadruple and dipole magnetic fields, some approximations must be made. The first is that the magnetic elements are considered to be ideal. The next is that the trajectories are considered planar in the xz plane (see Fig. 4.5) of the PRISMA reference frame. The final approximation is that the ions are emitted from the center of the target, but the reaction can occur anywhere within the target.

Motion of the ions in a quadruple magnetic field is defined by the Lorentz equation:

$$\vec{F} = q\vec{v} \times \vec{B}. \tag{4.4}$$

The magnetic field of the quadruple magnet is define as:

$$\vec{B} = -\vec{\nabla}U, \tag{4.5}$$

where

$$U = \frac{B_{max}}{\rho} xy. \tag{4.6}$$

Since we assumed a planar trajectory the force has components only along the xy plane, in particular:

$$\begin{aligned} F_x &\simeq q v_z B_x(x,y), \\ F_y &\simeq -q v_z B_y(x,y). \end{aligned} \tag{4.7}$$

By adjusting the field components B_x and B_y the final effect of the quadruple magnetic field is to focus the ions in the vertical (X) direction and defocus them in the horizontal (Y) direction.

Motion of the ions in a dipole magnetic field is defined by magnetic field $\vec{B}$, which, due to Lorentz force, makes the ions travel a circular path of radius ρ.

$$\begin{aligned} q\vec{v} \times \vec{B} &= \frac{mv^2}{\rho}\hat{r}, \\ \rho &= \frac{mv}{qB}. \end{aligned} \tag{4.8}$$

Thus, the final effect of the dipole is that the incoming ions are distributed on the focal plane according to their magnetic rigidity ρB, or the p/q ratio.
Since the maximum magnetic field and bending radius of PRISMA are fixed ($\rho B = 1.2$ Tm), we can check a limit on the maximum mass and energy an ion can have to be properly detected.

The total path of the ions in the magnetic spectrometer is obtain by summing different path:

$$L = L_{MCP} + L_Q + L_{Q-D} + L_D + L_{PPAC}. \tag{4.9}$$

The L_{MCP} is considered as the straight line from the center of the target to the quadruple entrance, the L_Q as the hyperbolic path inside the quadruple magnet while L_{Q-D} as the straight line between two magnets. The circular trajectory inside the dipole magnet is labeled as L_D. Finally, the straight line from the exit of the dipole to the focal plane is labeled as L_{PPAC}. For central trajectory $L \approx 6$m.
The **Solver** routine is an iterative software procedure used to reconstruct the trajectory. It starts from the known position of the ion in the MCP and guessed initial value of $\rho =$ 120 cm, which corresponds to the central trajectory. It follows the path described above, provides a position of the ion on the focal plane, and compares it with the measured one. If the difference between these two positions is less than 1 mm, the iteration ends. Otherwise, the procedure is repeated and the value of ρ is slightly changed until a good agreement with the measured value is obtained.

The range of ions in the IC can be calculated after a complete reconstruction of the trajectory.
The first step is to reject all events for which the path in IC is not compatible with the reconstructed trajectory in PRISMA. The second step is to construct total energy E

released in the IC, as a sum of ΔE_i.

Afterwards, a weighted distance L_w between the MWPPAC and each IC section can be constructed by using ΔE_i as a weight:

$$L_w = \frac{\Sigma_i L_i \Delta E_i}{E}. \tag{4.10}$$

Finally for an estimate of the range of ions in the IC, R, the MWPPAC-IC distance $L_{PPAC-IC}$ need to be subtracted from the a weighted distance L_w:

$$R = L_w - L_{PPAC-IC}. \tag{4.11}$$

4.3.1 Empirical corrections

The mass separation of the reaction products detected in PRISMA becomes increasingly important for very heavy ions, particularly because mass resolution is affected by optical aberrations. In this work, a suitable analysis was performed to separate different isotopes at a sufficient level to determine absolute yields. As a result, the mass resolution was improved and transfer channels were more clearly identified.

Effective quadrupole length and distance from target

In order to take into account the presence of fringe fields and higher-order magnetic fields, the nominal values of the quadruple length L_Q and the target-quadruple distance L_{Q-T} are slightly modified.

The optimization was performed by changing iteratively the two values in an interval around the nominal ones (L_Q = 420 mm; L_{Q-T}= 500 mm), looking for the values that maximize the A/q resolution. The new values were then kept fixed for the following analysis. This has to be performed for all energy-angle configurations.

Correction of optical aberrations

The procedure described above improved the straightness (i.e. reduces the curvature) of the A/q lines vs. the entrance vertical and horizontal position on the MCP. However, we found that there was still room for improvement. To further refine the straightness of the lines, we performed an alignment of the A/q lines with a polynomial. This additional

step allowed us to achieve even better mass results.

The procedure is illustrated on the left side of Fig. 4.7 where A/q (where q represents the atomic charge state) spectrum is enlarged and shown with respect to the x axis in the micro-channel plate (MCP) detector. The red curve represents the fit to the mean value for each ten bins of A/q projection. These were used to correct the A/q lines, i.e to straighten the lines. After being applied on the horizontal axis the same procedure was also applied to the vertical axis of MCP (see right side of Fig. 4.7).

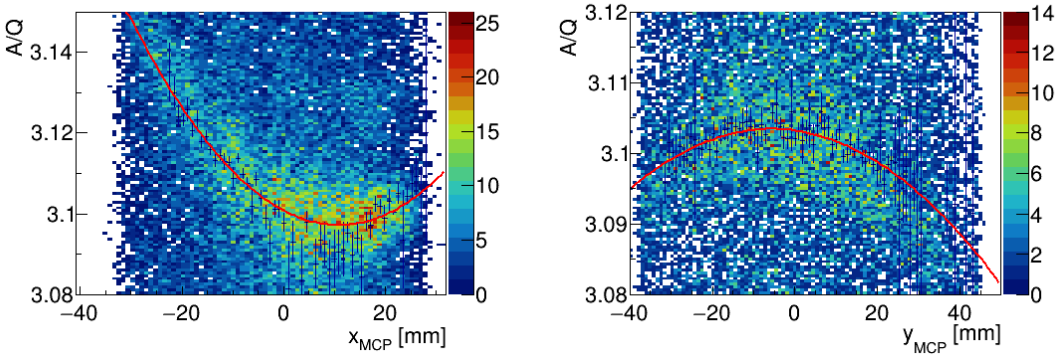

Figure 4.7: Enlargement of a part of the A/q spectra vs. horizontal x (left) and vertical y (right) axis in the MCP detector. The red curve is the fit to corresponding mean value for every tenth bin of A/q projection in this matrix.

The final result of this correction procedure is shown in Fig. 4.8. On the left side of figure is the uncorrected matrix of A/Q versus positions at the MCP detector, while on the right side is the same spectra after the corrections. It is clearly visible that the spectra on the right-hand side are straight, as one would expect from a physical standpoint.

In Fig. 4.9 the projection of A/q is shown for the (-2p) channel for the 1200 MeV beam energy and the PRISMA angle 25°, on the left before and on the right after correction. It can be observed that the resolution of the A/q has been much improved. As can be observed in the figure, before corrections, the peaks were difficult to distinguish, especially the less intense ones, whereas after corrections, they are clearly separated.

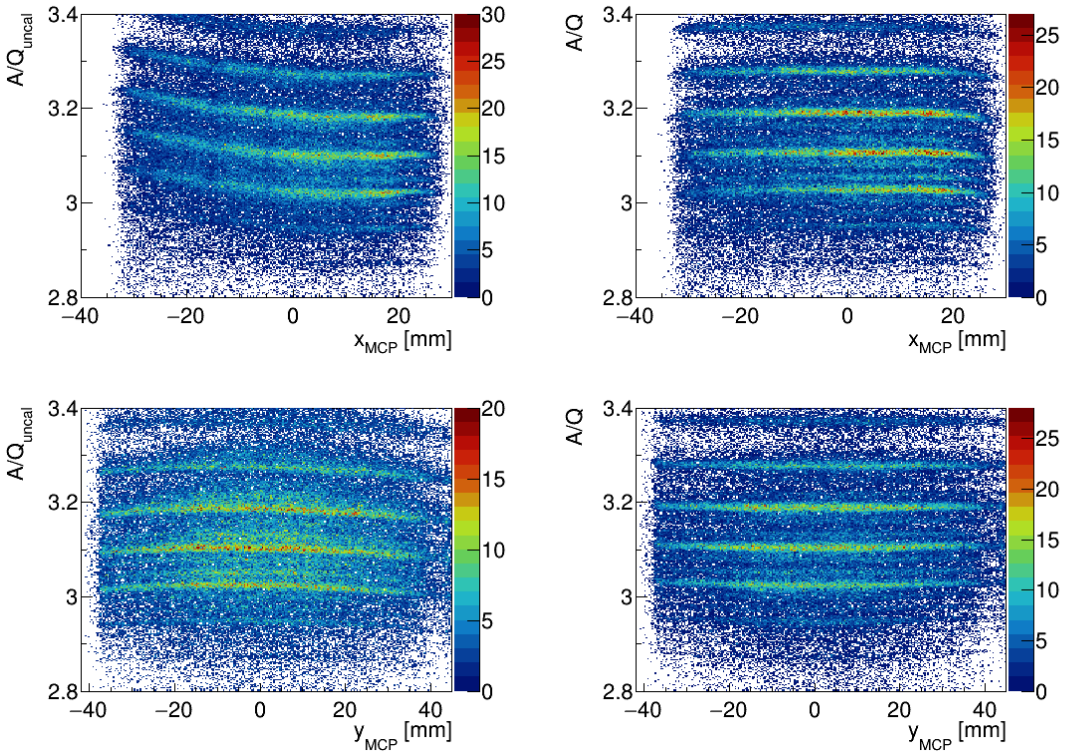

Figure 4.8: The A/q spectra vs. x (top), and vs. y (bottom) axis in the MCP detector, before (left) and after (right) corrections.

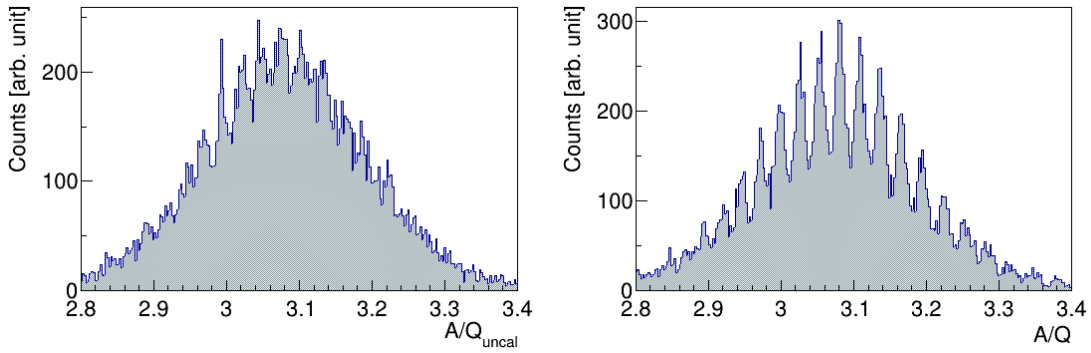

Figure 4.9: The A/q spectra, before (left) and after (right) correction, for (-2p) channel for E =1200 MeV and $\theta_{lab} = 25°$.

4.4 Atomic charge state identification

After selecting a particular atomic number, the atomic charge state (q) need to be constructed. Because of the influence of the Lorentz force on the ion trajectory, different charge states can be selected from the matrix E versus $\rho\beta$.

$$\frac{Av^2}{\rho} = qvB = \frac{2E_{kin}}{\rho} \implies q = \frac{2E_{kin}}{Bv\rho}. \tag{4.12}$$

The curvature radius ρ and velocity β are reconstructed event by event as described in 4.3. An example of E vs. $\rho\beta$ matrix is shown in Fig. 4.11 for Sn isotopes (Z=50), E_{lab} =1200 MeV and θ_{lab} =25° configuration.

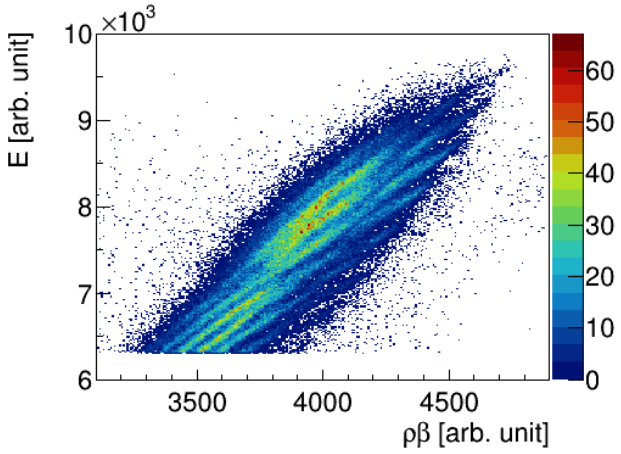

Figure 4.10: Energy vs. $\rho\beta$ matrix of Sn ions for E_{lab} =1200 Mev and θ_{lab} =25°.

The probability of a given charge state can be calculated using Shimas' empirical formula [91]. In Fig. 4.11 the comparison between the experimental result and the theory is shown. The distributions are shifted by 2, or more, charge states compared to the calculated ones. This implies that there are more energy losses than what is predicted by theory as will be discussed in Chapter 5.1. Also, the beam energy can be overestimated or underestimated due to uncertainty in ALPI energy of ±1.5%.

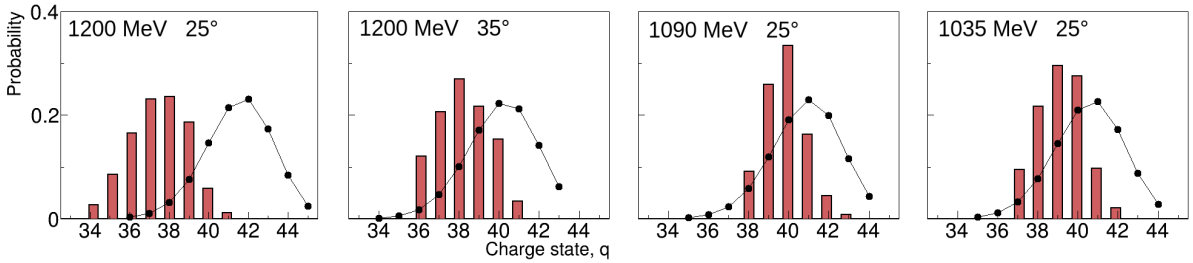

Figure 4.11: Experimental (bars) and charge state distributions by Shimas empirical formula (dots) for ^{118}Sn ions for different beam and angle configurations (from the left to right: E_{lab} =1200 MeV, θ_{lab} =25°; E_{lab} =1200 MeV, θ_{lab} =35°; E_{lab} =1090 MeV, θ_{lab} =25°; E_{lab} =1035 MeV, θ_{lab} =25°).

4.5 Mass spectra

The A/q is calculated from the TOF and the length L (see equation 4.9), taking into account the relativistic correction for the TOF.

$$\frac{A}{q} = B\rho\frac{TOF\sqrt{1-\beta^2}}{L}. \tag{4.13}$$

Mass spectra are constructed for each Z-state by summing the $(A/q)_i$ spectra selected by a particular gate in the E vs. $\rho\beta$ matrix for each q_i:

$$M_z = \sum_i \left(\frac{A}{q}\right)_i q_i. \tag{4.14}$$

After obtaining mass spectra, the centroid of the mass peak should be on the exact mass number in atomic mass units (integer). So, it is necessary to verify that the experimental A/q ratios agree with the calculated values. Therefore, the A/q axis must be recalibrated until the exact value is obtained. A second-order polynomial parameterization is used for the elastic channel. The same corrections are then applied for all Z, for each PRISMA setting. Moreover, a wrong q assignment can be excluded, since any error in the q assignment leads to a large shift in a mass spectrum, which is easy to recognize.

The final obtained mass spectra are shown in Fig. 4.12 and 4.13 where the achieved resolution was $\Delta A/A \approx \frac{1}{210}$. In all angle and energy configurations, the peaks around mass unit 115 and around 121 can be observed. These correspond to repetitions of the elastic channel due to the inability to distinguish charge states accurately. Such peaks are more pronounced at lower energies. Such repetitions will not be of great importance in our case, as we only want to observe the transfer channels ($\pm$1n) and ($\pm$2n).

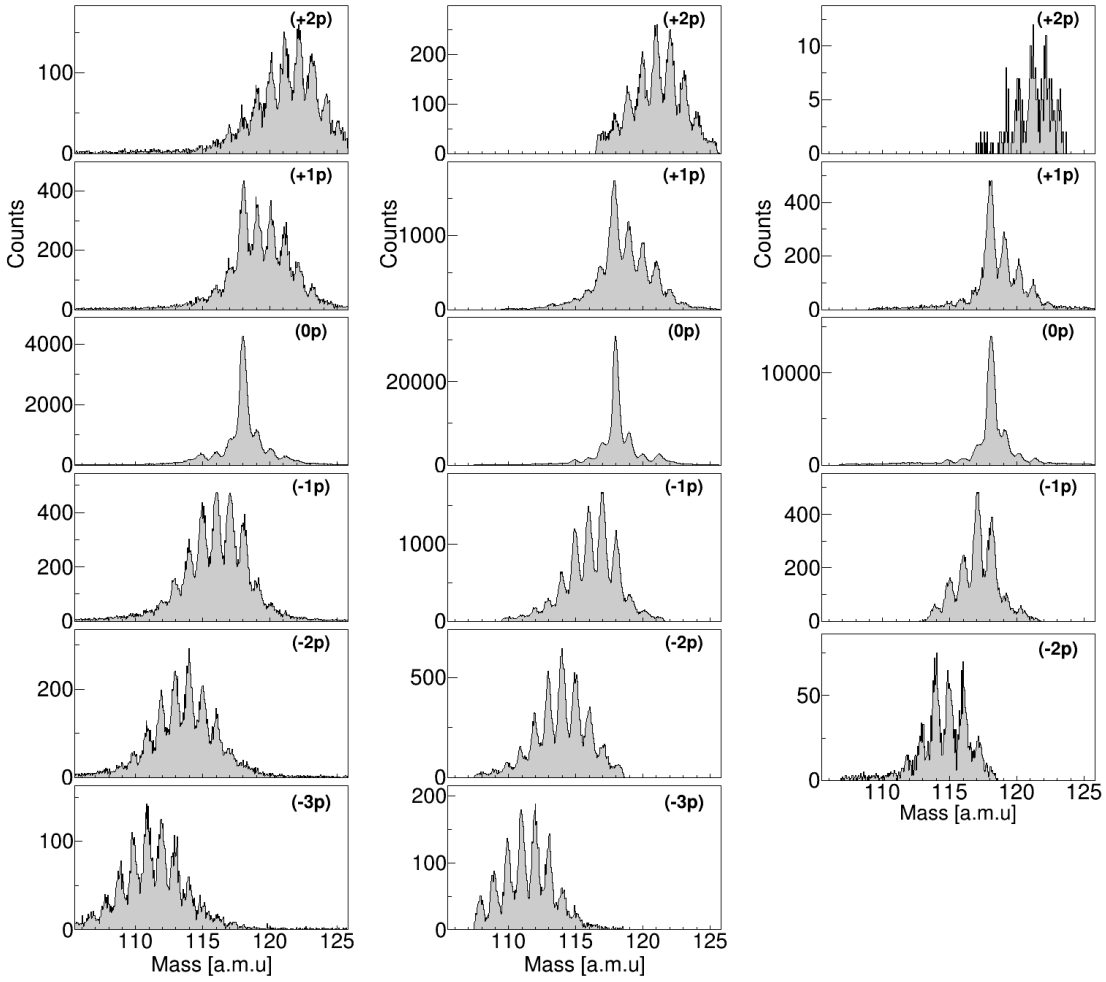

Figure 4.12: Mass spectra, for different beam energy E_{lab} = 1200 MeV (25°), 1200 MeV (35°) and 1090 MeV(25°), from left to right, respectively.

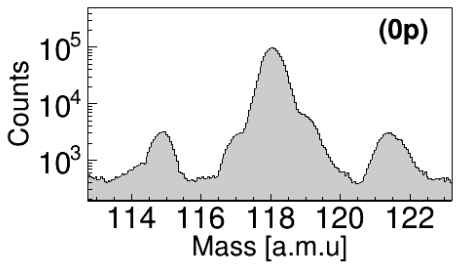

Figure 4.13: Mass spectra, for beam energy E_{lab} = 1035 MeV(25°)

4.5.1 Q-value calculation

Once the mass spectra are obtained, the energy distribution can be attributed to each mass. The Q-value distribution was calculated for each transfer product, event-by-event, assuming a pure binary process and taking into account the conservation of energy and momentum. Each ion's mass was determined by applying a graphical cut to the two-dimensional spectra, which plotted mass against position at the focal plane. Subsequently, every event within a certain cut was assigned a corresponding mass number. The exact expression is (see Fig. 4.14):

$$Q_{value} = \frac{M_3 + M_4}{2M_3M_4}P_4^2 - \frac{M_3 - M_1}{M_3}E_1 - \frac{1}{M_3}\sqrt{2M_1E_4}P_4\cos\theta, \tag{4.15}$$

where M_i is the mass, P_i is the momentum, E_i is the energy, and θ is the PRISMA angle. The target (^{118}Sn) is denoted by the number 2, the beam (^{206}Pb) by 1, target-like products by 4, and beam-like by 3.

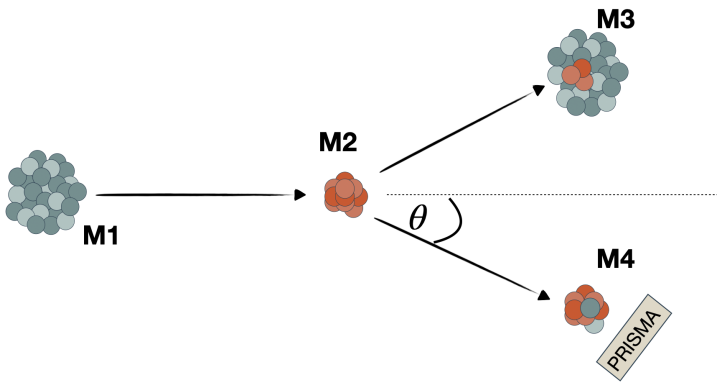

Figure 4.14: Outline of binary kinematics of heavy ion reaction M1+M2→M3+M4.

The final distributions for the neutron transfer channels are shown in Fig. 4.15, ranging from (+2n) to (-2n), and displayed in a sequence from top to bottom. These channels are presented for different energy-angle configurations, arranged from left to right.

It can be observed that as the beam energy decreases, the distributions become narrower, with their centroids moving closer to the ground-to-ground Q-value. At the lowest energy, the FWHM for the neutron transfer channels is about 12 MeV, which is less than 2% of the beam energy.

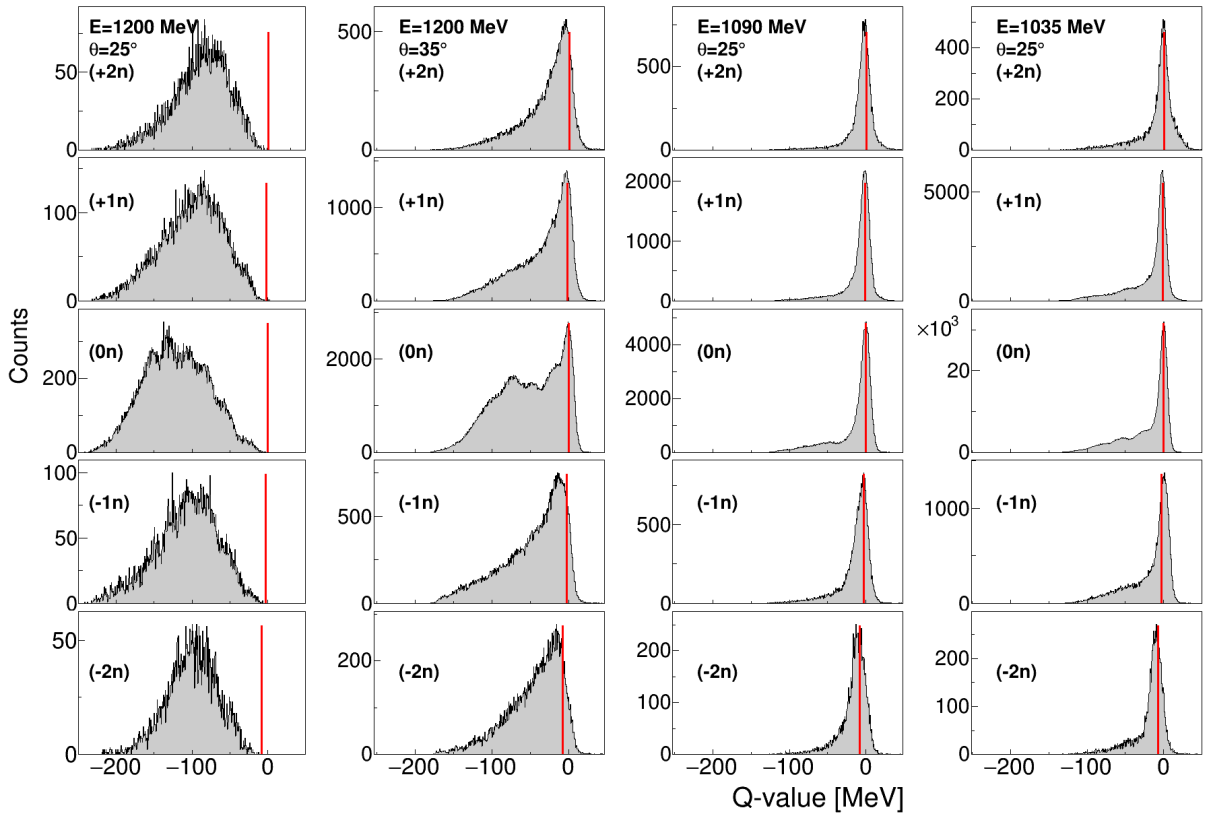

Figure 4.15: Q-value distributions for neutron transfer channels, from (+2n), at the top, to (-2n), at the bottom, for different PRISMA configurations (from the left to right: E_{lab} =1200 MeV, θ_{lab} =25°; E_{lab} =1200 MeV, θ_{lab} =35°; E_{lab} =1090 MeV, θ_{lab} =25°; E_{lab} =1035 MeV, θ_{lab} =25°).

Alignment of mass spectra

To improve the projection on the mass axis an additional procedure was applied. By plotting the two-dimensional mass vs. Q-value spectra, one can observe that by rotating the spectra the improved projections has been achieved. This is evident when we compare the original spectra on the left side of Fig. 4.16 with the corrected spectra on the right side. To do so, we use an empirical correction of mass spectra with a second order polynomial fit of elastic channel. We use the following formula :

$$\text{Mass}_{\ rot} = \text{Mass} - p_0 - p_1 \cdot Q_{value} - p_2 \cdot Q_{value}^2. \tag{4.16}$$

As an example, the final results of the corrections can be found on the right side of Fig. 4.16 for data taken at E_{lab} =1090 MeV and θ_{lab} =25°.

This procedure was performed for Sn ions (+0p) for each PRISMA setting. Subsequently, the same parameters were used for other proton transfer channels. Finally, the projections

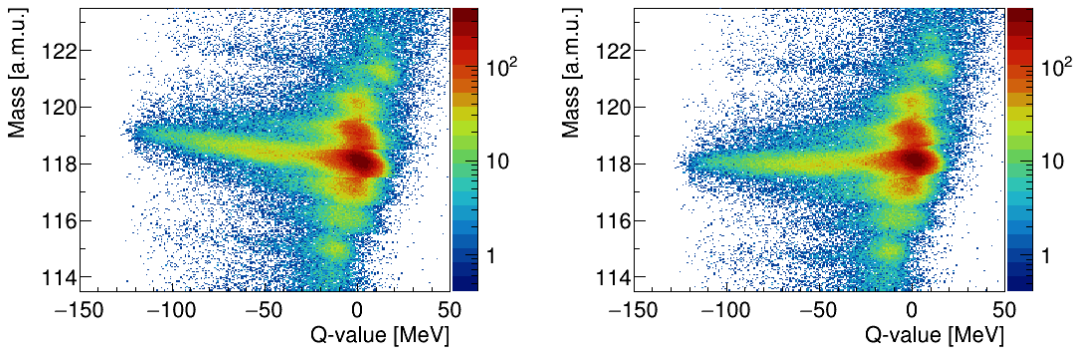

Figure 4.16: Mass vs. Q-value matrix, for Sn ions, before and after the correction, for E =1090 MeV and θ_{lab} =25°.

of the corrected matrices are used as the final mass spectra (Fig. 4.12 and 4.13). The obtained mass resolution was $\approx \frac{1}{210}$.

Also, in the spectra in figures 4.16, 4.12 and 4.13 the repeating parts around atomic numbers 121 and 115, caused by the impossibility of perfect separation of the charge states, can be observed. Mass spectra are constructed from Eq. 4.14, so if the q is missed by one unit the mass will be missed by $\frac{A}{Q}$.

For the elastic channel we have identified the charge states from 34 to 42 which implies that we can expect repetitions around 115 and 121 ($M_i = 118 \pm [2.8 - 3.4]$). In a heavy system like this, it is very difficult to exclude these repetitions. For this reason, in neutron transfer channels (+0p) we can only extract yields up to the (±2n) channels. Estimation has been extracted by comparison of the numbers inside the graphical cuts, noted as $a115$, $a116$, $a117$, $a118$, $a119$, $a120$, $a121$ for each mass. The ratio of repetitions and the elastic channel are calculated as $r_{up} = a121/a118$, $r_{down} = a115/a118$.

Therefore, the maximum of events due to repetition for (±1n) can be estimate as $N_{r117} = r_{up} \cdot a117$, $N_{r119} = r_{down} \cdot a119$. Finally, the estimated errors can be calculated as error(for +2n) $= r_{up} \cdot a117/a120$, error(for -2n) $= r_{down} \cdot a119/a116$. The estimated error due to double counting, for (+2n) and (-2n), is up to +20%.

Now that a comprehensive analysis was conducted and mass spectra were obtained for each exit channel, we can interpret the physical results. As already demonstrated, we can examine neutron channels in more detail up to ±2n at all energies, as well as proton channels at energies of 1200 and 1090 MeV. In the next chapter, we will focus on interpreting the obtained results. We will trace the evolution of the reaction across an angular

range of over 20 degrees at the highest energies. Additionally, we will construct transfer probabilities for neutron and proton channels from these mass spectra and compare them with other systems.

5 Experimental results and discussion

5.1 From quasi-elastic to deep-inelastic processes

In this section, the results of measurements at the 1200 MeV beam energy and at PRISMA angles $\theta_{lab} = 25^\circ$ and 35° will be presented [92]. Since we have collected data using PRISMA at two different detecting angles, at the same energy, and the angular acceptance of PRISMA is approximately 10 degrees, the total angular range covered at the highest energy is around 20 degrees in laboratory system and around 40 degrees in center of mass system. The large angular range from $\sim$19° to $\sim$41° provided the opportunity to closely observe the energy distribution in the reactions and to gain a deeper understanding of the transition from the quasielastic to the deep inelastic regime.

In particular, results for the differential cross-section (DCS) from the (-2p) channel to the (+2p) channel, including additional neutron channels, will be presented. The total cross-section (TCS) for these channels, obtained by integrating the DCS, with different cuts in TKEL distributions, will also be provided. In addition, the energy distributions will be presented as a function of angle, for better visualization of the transition from the quasielastic to the deep inelastic region. This type of two-dimensional matrix, in our case the Q-value as a function of scattering angle, is known as a Wilczynski plot [1]. These plots were constructed by selecting the products of the transfer reactions by mass and charge. As already explained in 4.5.1, the Q-values were calculated assuming a binary reaction and taking into account conservation of energy and momentum.

An example of this two-dimensional spectrum, for ^{206}Pb+^{118}Sn system, can be seen in Fig. 5.1, in which the plot for the ($+1n$) channel is shown along with projections of the Q-value axis at specific center of mass angles. It can be observed that the distribution

at more forward scattering angles is dominated by a QE peak near the ground-to-ground state (Q_0), which becomes increasingly less populated as the angle moves further backward from the grazing angle ($\theta_{\rm cm} \simeq 109°$). At the same time, larger energy loss components become more significant and tend to take on a Gaussian-like shape. However, it should be noted that the energy and angular acceptance of the spectrometer can affect the final shape of data distribution at these large energy losses. The analysis of the calculated response revealed a slight variation in transmission, which is most notable at the outer edges of the angular acceptance of the spectrometer. This variation does not affect the general conclusions [93, 94].

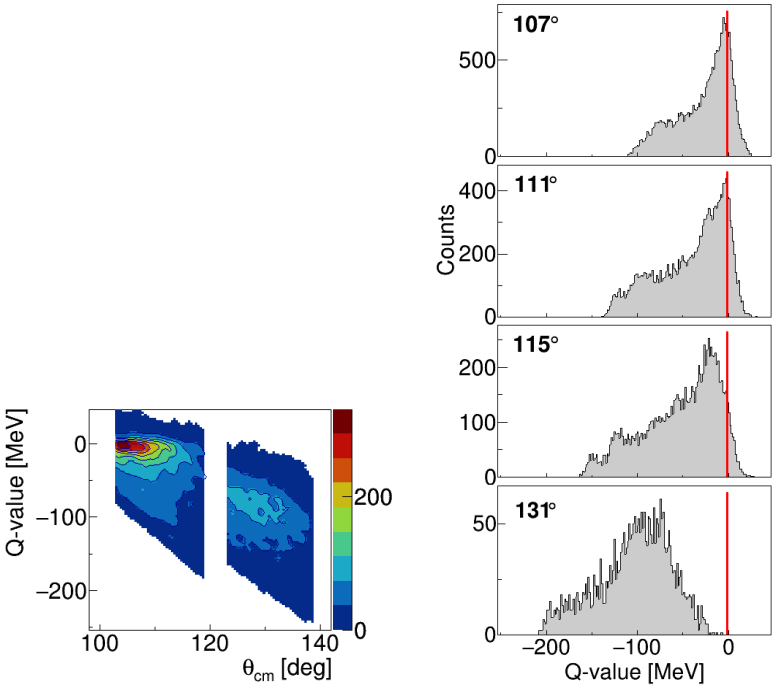

Figure 5.1: Matrix of Q-value vs center of mass angle $\theta_{\rm cm}$ for the ($+1n$) channel (left). The displayed matrix was obtained by matching the measured events at the two PRISMA angular and magnetic settings. The panels on the right show the projections on Q-value at the indicated center of mass angles (corresponding to $\theta_{\rm lab} = 36.5°$, $34.5°$, $32.5°$, and $24.5°$ from top to bottom panels, respectively, with $\Delta\theta_{\rm lab} \simeq 2°$). The vertical (red) lines represent the ground-to-ground state Q_0-value.

Wilczynski plots for the strongest channels in the vicinity of elastic channel are shown in Fig. 5.2, while their projections on the Q-value axis around the grazing angle (from θ_{cm} ~100° to θ_{cm} ~140°) are shown in Fig. 5.3. The (+1p-1n) channel is excluded because of the "leakage" from the elastic channel, which occurs due to the overlap between the (+0p) and (+1p) channels in the ΔE vs. E matrix.

The whole distributions can be well followed, from regions close to the Q_0 values to very

large energy losses. The dominance of the high Coulomb field in the reaction can be clearly observed in the Wilczynski plot due to bending of large energy loss events to more backward scattering angles (as discussed in Chapter 1). This means that for the more backward scattered angles there is an increase in the number of events that have a large loss of energy, which is indicative of deep inelastic collisions [5, 6]. However, angular focusing due to nuclear attraction can also be seen as there are quasi-elastic and deep elastic components focused on the same (grazing) angle.

This observation differs from the results obtained for similar reactions involving medium-mass projectiles on heavy targets [2–4]. Specifically, in the ^{64}Ni+^{238}U, ^{40}Ar+^{208}Pb, and ^{46,48,50}Ti+^{208}Pb systems. While in the ^{64}Ni+^{238}U, the events with large energy losses are focused on the same angles as QE components, around the grazing angle, in ^{48}Ti+^{208}Pb, one can notice larger energy losses at more forward angles. Although both systems were measured in a wide angular range of approximately $\Delta\theta_{cm} \approx 70^{\circ}$, the distribution appears to be more "banded" at the forward angle for the ^{48}Ti+^{208}Pb system. The ^{40}Ar+^{208}Pb system was measured at a smaller angular range of approximately $\Delta\theta_{cm} \approx 20^{\circ}$ with a beam energy 30% higher than the Coulomb barrier, and similar behavior as in the ^{64}Ni+^{238}U system is visible. For the few nucleon transfers and neutron transfers, most of the yield is concentrated close to the grazing angle, and the large energy loss tails do not strongly influence the measured cross section.

As can be seen in Fig. 5.3, for pure neutron transfers, the distributions peak near Q_0, with events extending to larger energy losses. However, only in the elastic+inelastic channel (0n), a narrow quasi-elastic peak is well separated from the large energy-loss components (the separation position is indicated by the arrow in Fig. 5.3.

For channels involving the stripping of protons with additional striping of neutrons, the distributions begin near the optimum Q-values. Each optimum Q-value is defined as Q-value with maximum probability for that transfer channel, which differs by a few MeV from Q_0, but peaks at large energy losses. This suggests that the evaporation of neutrons was likely to occur in these channels. It can be observed that channels involving a large number of transferred nucleons, such as isotopes belonging to two proton stripping, have similar Q-value shapes. For neutron stripping processes, this shape reflects one of the heaviest mass. This is expected as these channels receive contributions from evaporation of nearby higher mass channels with larger yields. This trend can also be seen in the

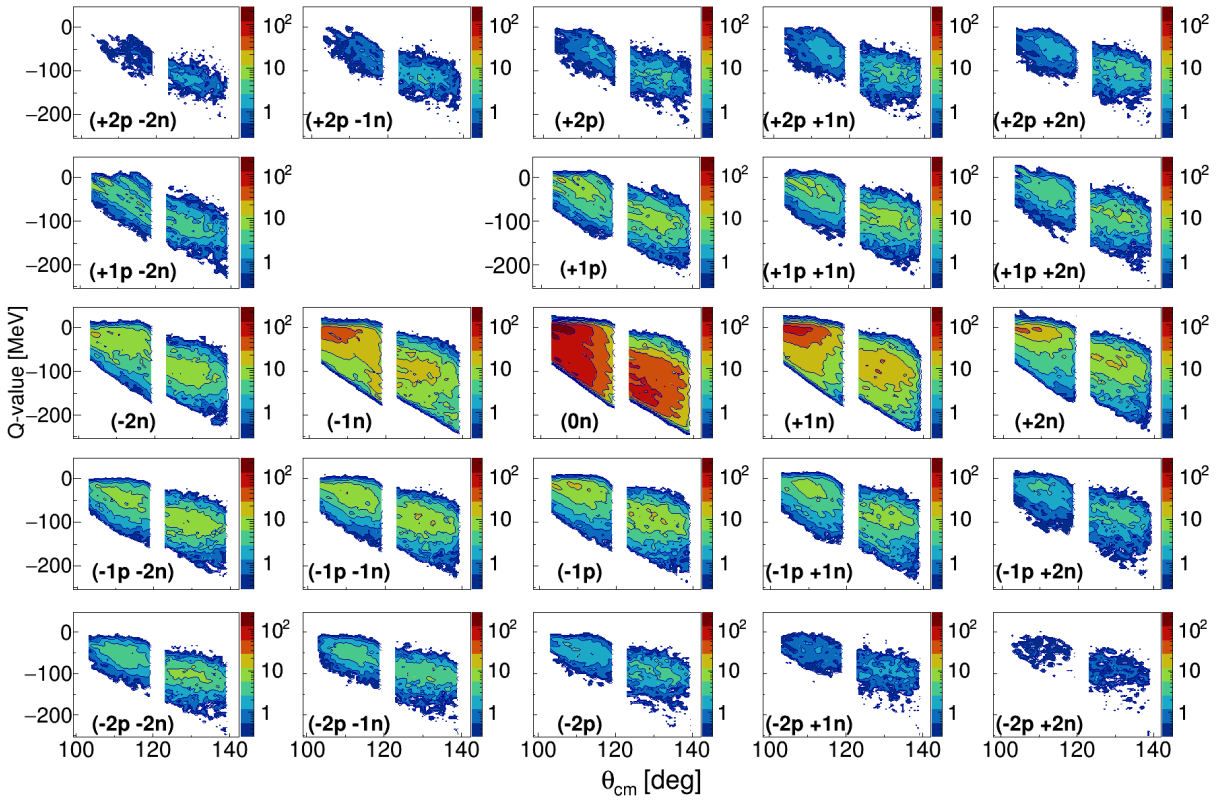

Figure 5.2: Wilczynski plots (Q-value vs θ_{cm}) measured at PRISMA angles $\theta_{\mathrm{lab}} = 25°$ and $35°$ for the labeled transfer channels. The contours represent the double-differential cross sections, $\frac{d^2\sigma}{d\Omega dQ}$.

neutron pick-up side for the two proton stripping. However, it should be noted that the overall effect of evaporation on the integrated yields of each channel is much less significant, as higher mass channels have progressively lower primary cross sections. One proton transfer channels exhibit a behavior that falls between pure neutron transfers and two-proton stripping channels in terms of energy losses and evaporation effects. The specific details of the shapes depend on nuclear structure or dynamics.

If we compare these spectra measured at 1200 MeV with those measured at the lower beam energy 1090 MeV, shown in figure 5.4, one can see slightly different behavior. As we go lower in energy, the distributions become narrower. Also lower energy distributions are more centered around Q_0, which is particularly visible in proton striping channels. For the lowest measured beam energy (1035 MeV), the Q-value spectra for neutron transfer channels are shown in figure 5.5. Due to low statistics in proton transfer channels at the lowest energy, only neutron transfer channels were obtained. The position of the peaks compered to Q_0 and the width of the distributions are similar as ones at 1090 MeV. For

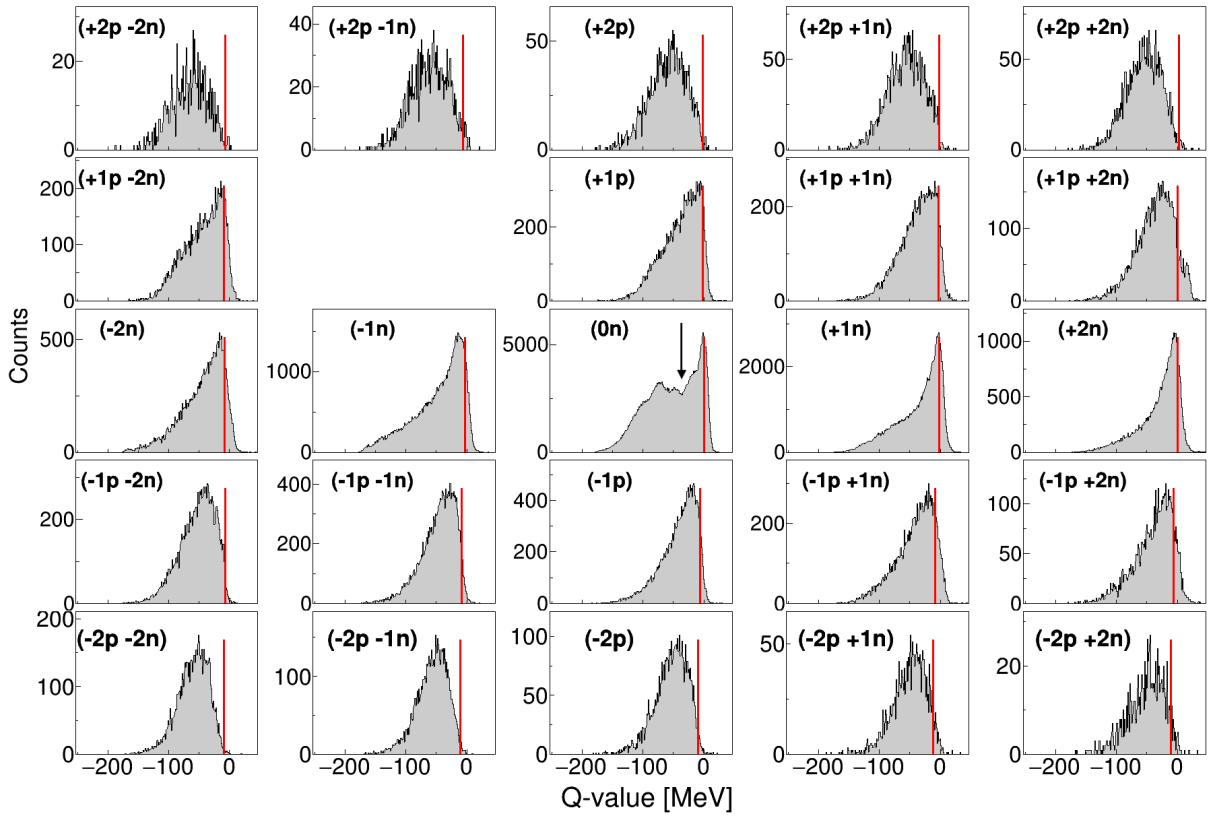

Figure 5.3: Q-value distributions measured at $E_{lab} = 1200$ MeV and $\theta_{\rm lab} = 35°$ for the labeled transfer channels. Vertical lines indicate the ground-to-ground state Q_0 values. The arrow represent position where the quasi-elastic and deep elastic components are separated.

better comparison of the width of the distributions at two lower energies, scaled Q-value distributions for the (+1n) transfer channel for both energies are shown in figure 5.6. It can be clearly seen that the distribution narrows as the beam energy decreases. In the case of neutron transfer channels, the peak width narrows, as the beam energy changes from 1090 to 1035 MeV, by approximately 15 percent.

Because few nucleon-transfer channels near the grazing angle are close to the quasi-elastic region, differential cross sections were extracted from the measurement performed with PRISMA at $\theta_{\rm lab} = 35°$. For the elastic+inelastic (0n) and pure neutron-transfer channels (-2n, -1n, +1n, +2n), the differential cross sections could also be extracted with PRISMA at $\theta_{\rm lab} = 25°$. At both angular settings, the quasi-elastic part was obtained by integrating the range of ~ 35 MeV around Q_0, close to the valley visible in the Q-value spectrum of the $(0n)$ channel. The method was tested by using different integration ranges in Q-value spectra. For the channels involving protons, where the deep-inelastic components could not be separated, an integration of the full Q-value distributions with PRISMA at

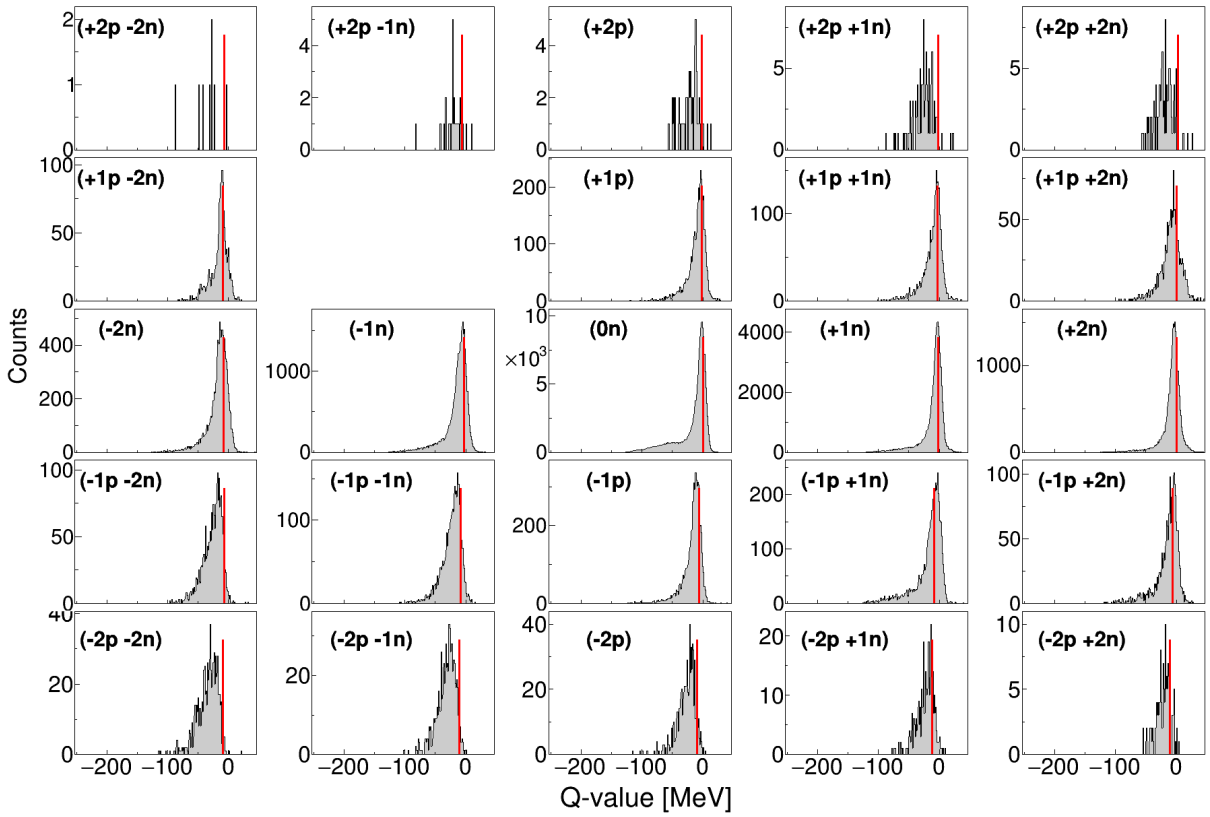

Figure 5.4: Q-value distributions measured at $E_{lab} = 1090$ MeV and $\theta_{\rm lab} = 25°$ for the labeled transfer channels. Vertical lines indicate the ground-to-ground state Q_0 values.

$\theta_{\rm lab} = 35°$ was applied.

Angular distributions obtained in the described way are shown for selected channels in Fig. 5.7. The filled circles represent the integration of the full Q-value range and the empty circles represent the integration of the quasi-elastic components only (integration from the Q_0-35 MeV, where the separation of components is visible, as shown in Fig. 5.3). Calculations performed with the GRAZING code were also included in the figure. The data was plotted in a restricted angular range, omitting the edges of the distribution which may be affected by the spectrometer's acceptance. The quasi-elastic distributions were obtained by matching the two PRISMA angular and magnetic settings. The elastic+inelastic data was presented as a ratio to the Rutherford cross sections. The absolute scale of cross sections was obtained by normalizing the quasielastic ^{118}Sn events to the Rutherford cross section. The normalization constant was found to be in agreement with the one obtained by normalizing the quasielastic yield to the GRAZING computed $(+1n)$ cross section. This constant was retained for all neutron and proton transfer channels.

The GRAZING code results are shown in Fig. 5.7 (green curve) describe well the elas-

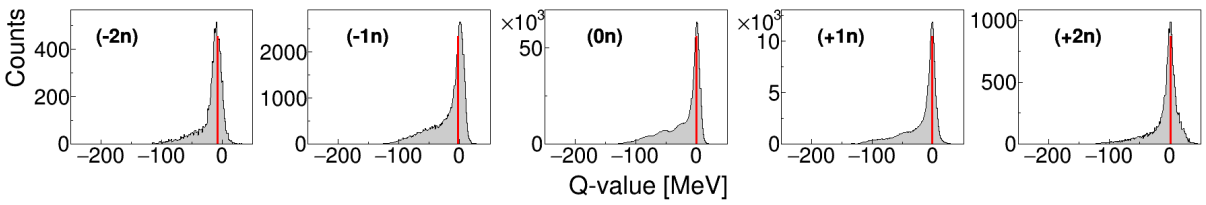

Figure 5.5: Q-value distributions measured at $E_{beam} = 1035$ MeV and $\theta_{\rm lab} = 25°$ for the labeled transfer channels. Vertical lines indicate the ground-to-ground state Q_0 values.

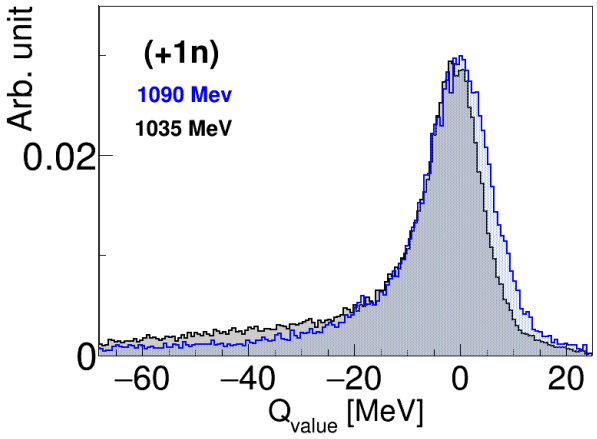

Figure 5.6: Comparison of Q-value distributions, normalized to each other, measured at $E_{lab} =$ 1035 MeV (black) and $E_{lab} = 1090$ MeV (blue) at $\theta_{\rm lab} = 25°$ for the (+1n) transfer channel.

tic+inelastic cross section over Rutherford cross section, in particular the fall-off at angles beyond the quarter point, at backward angles, indicating the correct treatment of the absorption. Calculations also reproduce well the one nucleon-transfer channels, demonstrating the correct treatment of form factors and the chosen range of partial waves. The fact that a quite good agreement holds also for the channels involving one-proton stripping and neutron pick-up indicates their direct nature. A similar agreement for the one-proton pick-up was not achieved. This underestimation propagates to other channels involving neutron pick-up, though the shapes are always well reproduced. Along the neutron stripping side, which is more influenced by neutron evaporation, calculations underestimate progressively the absolute values of the cross section.

The main observations made from the angular distributions can also be seen in the total cross sections presented in Fig. 5.9 for the different observed transfer channels.

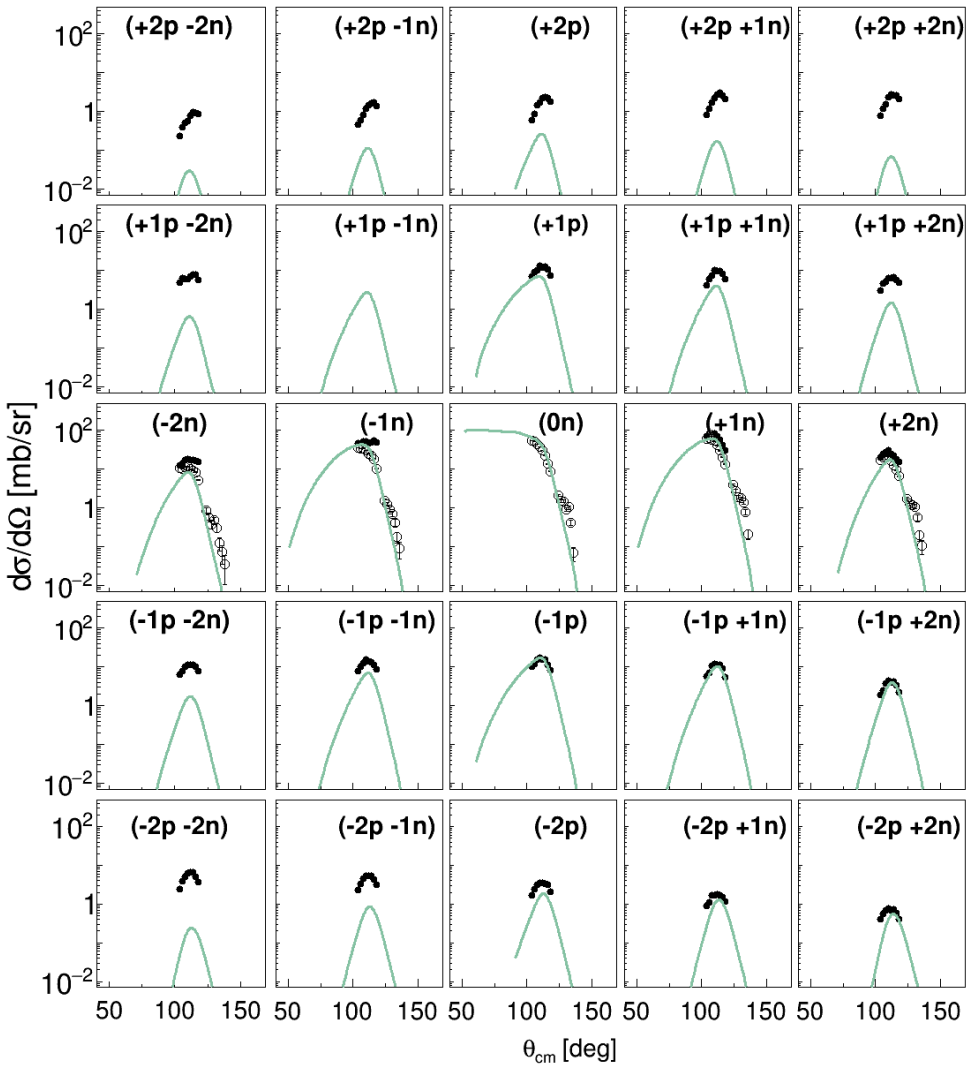

Figure 5.7: Experimental differential cross sections (points) compared with GRAZING calculations (lines) without including effects of neutron evaporation. Filled circles correspond to the integration of the full Q-values, while empty circles correspond to the quasi-elastic part only (integration of the Q-value > -35 MeV + Q_0). The elastic+inelastic channel is plotted as a ratio over the Rutherford cross section (multiplied by 100). The experimental cross section for the $(+1p-1n)$ channel could not be safely extracted due to partial overlap with the ^{118}Sn yield. Experimental errors are the statistical ones only. The relative normalization between the different PRISMA settings at $\theta_{\rm lab} = 25^\circ$ and 35° was obtained by using the elastically scattered ^{118}Sn ions in the monitor detector placed at 58°.

The experimental values were obtained by integrating the differential cross sections, assuming a Gaussian shape, with cuts in TKEL distributions for pure neutron transfer channels and fitting the whole distributions for channels which involves the transfer of protons. From the figure 5.7, it is clear that the pure neutron transfer channels are well reproduced by the calculations. The same can be concluded for the pure $(-1p)$ channel. However, as we move along the proton-stripping side, the experimental cross sections tend

to shift towards lower masses and are progressively underestimated by GRAZING calculations. It's important to take into account that the primary cross sections for channels involving neutron stripping may be significantly modified by neutron evaporation from the larger masses, leading to the reshuffling of the final mass distribution and affecting the lower mass region of the populated isotopes more significantly.

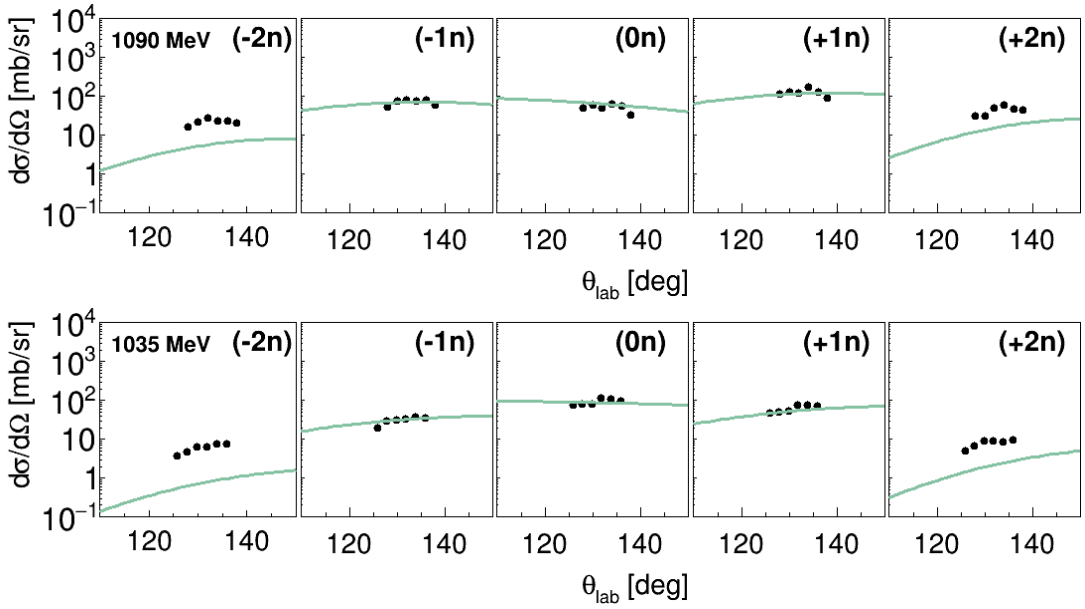

Figure 5.8: Experimental differential cross sections (points) for E_{lab} = 1090 MeV (top) and 1035 MeV (bottom) compared with GRAZING calculations (lines) without including effects of neutron evaporation. Filled circles correspond to the integration of the Q-values> -35 MeV+Q_0. The elastic+inelastic channel is plotted as a ratio over the Rutherford cross section (multiplied by 100). Experimental errors are only the statistical ones. The relative normalization between counts and [mb/sr] is done with the GRAZING (+1n) channel.

It was previously observed that there is a difference between proton and neutron transfers when comparing experimental and calculated cross sections in systems with medium-mass projectiles [2, 10, 18]. This is partly due to the larger energy loss of proton transfer channels and the effects on the trajectories of entrance and exit channels due to the charge transfer reactions [3] , which may not be fully accounted for by current theories. The discrepancies with theory for the two proton transfer channels may also indicate the presence of additional degrees of freedom, such as pair-transfer modes [10, 18]. However, it is still unclear to what extent these additional degrees of freedom contribute to the cross sections. In general, there may be a need for revisiting some theoretical prescriptions for proton transfer, particularly for the proton pick-up channel, since this is crucial for understanding the population of neutron-rich heavy nuclei.

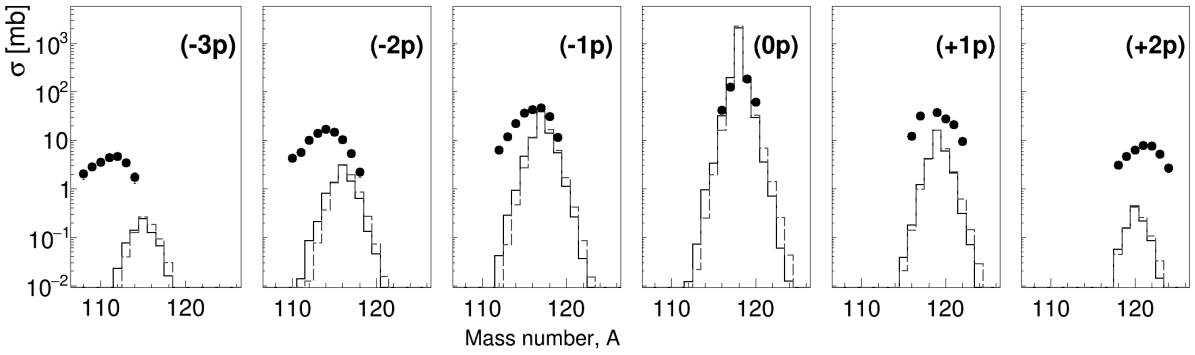

Figure 5.9: Experimental (points) and GRAZING calculated (histograms) total angle and Q-value integrated cross sections for the various transfer channels populated in the ^{206}Pb+^{118}Sn reaction at E_{lab}=1200 MeV. Experimental errors are statistical ones only, and are mostly within the size of symbols. The solid and dashed histograms are the calculations performed with and without evaporation, respectively. The experimental cross sections for the pure neutron transfers have been extracted only for the $(\pm 1n)$ and $(\pm 2n)$ channels and only for the quasi-elastic part of the Q values (see text for details). Due to the overwhelming elastic yield the cross section for $(+1p-1n)$, corresponding to ^{118}Sb, is not included.

If we examine the angular distributions for neutron transfer channels at energies below the barrier, specifically at $E_{lab} = 1090$ MeV and 1035 MeV, as depicted in Figure 5.8, we notice that the spectra exhibit a relatively flat behavior. This agrees well with theoretical calculations, as illustrated in Figure 2.2. Consequently, due to flat shape of distributions, it is challenging to perform the integration of spectra to determine the total cross sections for these lower energies. Additionally, when comparing the data and calculations for one-neutron stripping and pick-up processes as well as elastic+inelastic channel, there appears to be a good agreement between the data and theory. However, for the stripping and pick-up of a pair of neutrons, the GRAZING calculations tend to underestimate the total values. Furthermore, it's worth noting that the selected data points do not seem to be significantly influenced by variations in the acceptance at the edge of the MCP detector. This implies that the observed shape of the distributions remains relatively consistent despite potential limitations in detector coverage.

The selected point shown in angular distributions in figure 5.7 and 5.8 are used to construct the transfer probabilities for each transfer channel which will be described in next chapter.

5.2 Transfer probabilities

Transfer probabilities P_{tr} (equation 1.12) is defined as the ratio of the transfer yield over the elastic one :

$$P_{\mathrm{tr}} = \frac{d\sigma_{tr}}{d\sigma_{el}}.$$

To calculate P_{tr}, we used the quasi-elastic cross sections instead of pure elastic ones. The reason for this choice becomes evident when we examine the Q-value spectra for different energy-angle configurations in pure neutron and proton transfer channels (refer to Figures 5.10 and 5.11). One can notice that as we move to lower energies below the barrier (specifically at 1090 and 1035 MeV), the peaks in these spectra become very narrow. For these energy points, in proton transfer channels we decided to integrate the entire Q-value spectra, while for pure neutron transfer channels we use the same cut on Q-values as for the 1200 MeV.The quasi-elastic part at larger energies is much larger than for lower energies. Because of that, for the 1200 MeV energy, as mentioned previously for neutron transfer channels, the integration is carried out for only quasi-elastic part of distribution (where the separation in the (0n) channel becomes visible, represented by dashed lines in Fig. 5.10). In the case of proton transfer channels, due to not visible separation, the entire spectra was used in the integration.

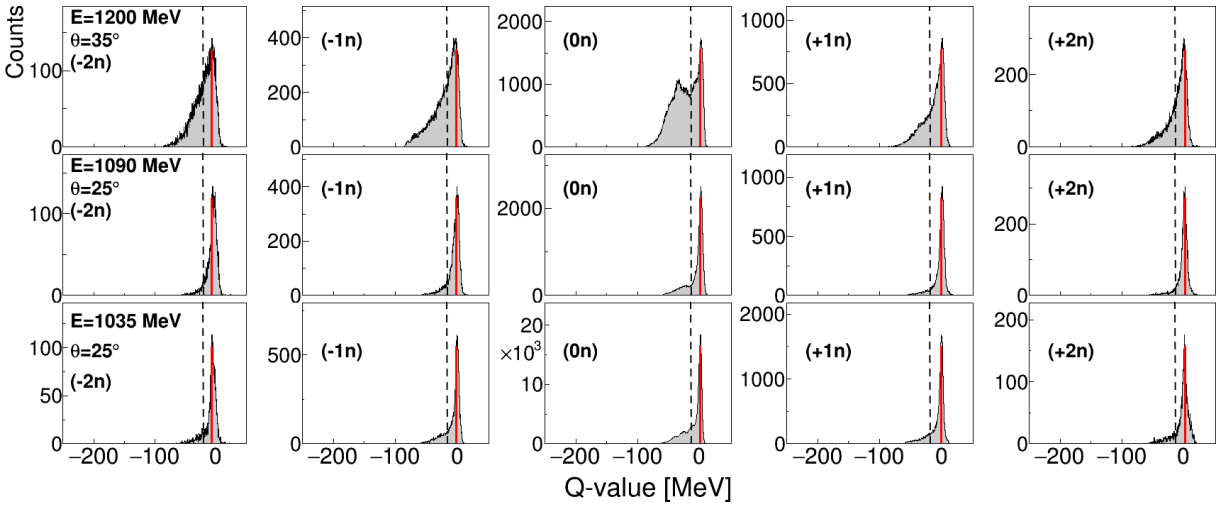

Figure 5.10: Q-value distributions for neutron transfer channels for labeled transfer channel and energy- angle configuration (divided by factor 2). The spectra were contracted from integration of the whole angular range. Dashed lines represent the position between the quasi-elastic and deep inelastic part of distribution.

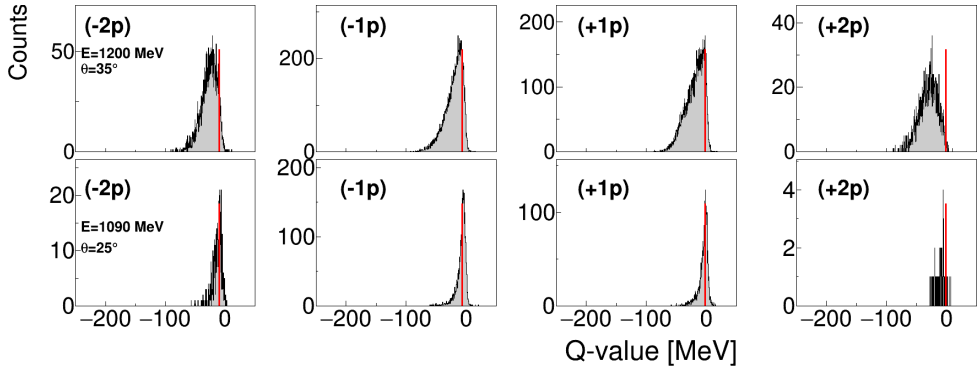

Figure 5.11: Q-value distributions for proton transfer channels for labeled transfer channel and energy- angle configuration (divided by factor 2). The spectra were contracted from integration of whole angular range.

It is convenient to present these probabilities as a function of the distance of closest approach for a Coulomb trajectory (d). Plotting P_{tr} against d is highly beneficial, as it allows for the superimposition of angular distributions from various bombarding energies into a unified view. The distance of closest approach, d, for a Coulomb trajectory is related to the center of mass scattering angle, θ_{cm}, and beam energy, E_{cm}, via the expression 1.13:

$$d = \frac{Z_t Z_p e^2}{2E_{cm}} \left(1 + \frac{1}{\sin(\theta_{cm}/2)}\right).$$

The Z_t and Z_p are the atomic numbers of target and projectile, respectively, and e is the charge of the proton, with $e^2 = 1.44$. The energy of the beam in the center of mass system is calculated from the energy in the laboratory system using the following equation:

$$E_{cm} = \frac{M_t}{M_p + M_t} E_{lab}. \tag{5.1}$$

By combining data from different measured energies and different PRISMA angles and by taking the advantage of PRISMA's angular acceptance (up to $\theta_{lab} \approx 11°$), the transfer probabilities (P_{tr}) for neutron transfer channels within the range of $d = 14.86 - 16.63$ fm were successfully obtained. Similarly, for transfer channels involving the transfer of protons, due to low statistics for the lowest energy, the range was $d = 14.86 - 15.71$ fm. To construct each point we performed the summation using one-degree steps.

The differential cross section for a particular transition is given by the quantum mechan-

ically defined transition amplitude T_{ab} [56]:

$$\left(\frac{\mathrm{d}\sigma(\theta)}{\mathrm{d}\Omega}\right)_{\mathrm{tr}} = \left|T_{\mathrm{ab}}(\theta)\right|^2 . \tag{5.2}$$

The integral, due to the short-range nature of the nuclear interaction, can be factorized into a scattering component, denoted as $f_{\mathrm{sc}}(\theta)$, and another component associated with the value of the form factor at the distance of closest approach:

$$T_{\mathrm{ab}}(\theta) \approx F\left(d_{\mathrm{min}}\right) f_{\mathrm{sc}}(\theta) \tag{5.3}$$

The semi-classical expression previously provided can now be obtained, with a factorization into a 'scattering' cross section and transfer probability:

$$\left(\frac{\mathrm{d}\sigma(\theta)}{\mathrm{d}\Omega}\right)_{\mathrm{tr}} \approx \left|F\left(d_{\mathrm{min}}(\theta)\right)\right|^2 \left(\frac{\mathrm{d}\sigma(\theta)}{\mathrm{d}\Omega}\right)_{\mathrm{el}} . \tag{5.4}$$

This factorization approach, extensively employed in the semi-classical treatment of Coulomb excitation, simplifies the discussion of data systematics. By taking the ratio of the measured transfer cross section to the elastic cross section, we can directly plot the relevant experimental transfer probability:

$$P_{\mathrm{tr}}(\theta) \approx \left|F\left(d_{\mathrm{min}}(\theta)\right)\right|^2 \tag{5.5}$$

Consequently, it is anticipated that the transfer probability will exhibit the same functional dependence as the squared form factor. In terms of the radial coordinate, the form factor is expected to exhibit an exponential behavior determined by the wavefunctions' tails at sufficiently large distances. For neutrons, the asymptotic behavior can be described simply by the function:

$$F(d) \sim \mathrm{e}^{-\alpha d} \tag{5.6}$$

The decay constant α is, determined by the binding energy B:

$$\alpha = \sqrt{2mB/\hbar^2} \tag{5.7}$$

The transfer probabilities are hence very well described by an exponential function with a decay length that gets smaller as the number of transferred neutrons increases. This

behavior of the transfer probabilities suggests a simple phenomenological interpretation of the data:

$$P_{tr} \sim e^{-2\alpha d}. \tag{5.8}$$

The binding energy of the donor or acceptor nucleus before or after the reaction is the binding energy taken in the initial or final system. For the neutron transfer channel the binding energy is approximately the energy needed to remove one neutron $B \approx -S_n$.

The experimental slopes should align with those calculated from the binding energy for 1n (one neutron transfer) processes. In an independent particle description, for the two-particle channel a probability is proportional to the square of the single-particle probability, where EF is used as a measure of enhancement $P_{tr}(2n) = EF \times P_{tr}(1n)^2$.

To determine the slope α, the separation energies from both partner nuclei are taken into consideration, as in Ref. [95]. For example, in the case of the (-1n) channel, in the ^{206}Pb+^{118}Sn reaction, resulting in ^{207}Pb+^{117}Sn the α is calculated as the average of the α calculated with different B, the α from the binding energy for one neutron added to ^{206}Pb (forming ^{206}Pb+1n) and the α calculated with the binding energy for one neutron removed from ^{118}Sn (to yield ^{117}Sn+1n). Consequently, the α values for ^{207}Pb and ^{118}Sn are derived from available data for the binding energies (S_n) which are listed in the table 5.1. In the context of neutron pickup where ^{205}Pb+^{119}Sn is formed, we calculate the average α of different binding energies. This involves adding one neutron to ^{118}Sn to form ^{118}Sn+1n and simultaneously removing one neutron from ^{206}Pb to yield ^{205}Pb+1n. To determine α for the (+1n) we need the average α values of ^{206}Pb and ^{119}Sn. In table, 5.1 α is calculated for the target, projectile and nuclei around them ($\pm$1n). In the last rows the average α is calculated for the ($\pm$1n) channel.

In figure 5.12 experimental data (points) for ($\pm$1n) and ($\pm$2n) channels are shown together with P_{tr} calculated from the binding energy for ($\pm$1n), from which the slopes are defined. In the same figure the square root of these one-nucleon transfer probabilities are also plotted in top-left and bottom panel. The calculated transfer probabilities for ($\pm$2n) are plotted with dashed red lines. For the neutron stripping channels in the top right panel in Figure 5.12, the $P_{tr}^2(1n)$ is plotted with red solid line while the red dashed line represent the root of it. In addition, the experimental points for the one-neutron transfer channel have been fitted with the exponential function $A \cdot \exp(-2\alpha_{\text{fit}} \cdot d)$. The results are plotted with solid black lines. The square of the fitted functions are shown with black dashed

channel	S_n(MeV)	$\alpha(\mathrm{fm}^{-1})$
$^{206}_{82}$Pb	8.09	0.625
$^{205}_{82}$Pb	6.73	0.570
$^{207}_{82}$Pb	6.74	0.570
$^{118}_{50}$Sn	9.33	0.671
$^{117}_{50}$Sn	6.94	0.579
$^{119}_{50}$Sn	6.48	0.559
(-1n)	$\frac{1}{2}\left(\alpha(^{207}\mathrm{Pb})+\alpha(^{118}\mathrm{Sn})\right)$	0.621
(+1n)	$\frac{1}{2}\left(\alpha(^{206}\mathrm{Pb})+\alpha(^{119}\mathrm{Sn})\right)$	0.592

Table 5.1: Calculations of α for neutron transfer channels.

lines. The vertical line represents the position of d, where the energy was calculated from the Bass formula and the angle is set to be 35° in the laboratory system. The distance of closest approach calculated here represents "the barrier" in order to better understand the position of the measured points.

We observe a good agreement between the calculated slope and the one obtained from the fit for both (+1n) and (+2n) channels. It appears that EF is around 1. In the case of neutron stripping channels, (-1n) and (-2n), the slopes from the fit and calculation differ more then in neutron pick-up channels.

Determining the necessity of introducing the EF for describing neutron stripping channels is challenging. This is due to the discrepancy observed in these channels: the slopes derived from a defined α and a fitted one for the (-1n) channel do not align well with the slope of the (-2n) channel. Hence, if we look at the left and right panels in the upper part of Figure 5.12, we cannot clearly conclude whether there EF is greater than 1. What can be observed is that when comparing $P_{tr}(-1n)$ obtained from the fit and $P^2_{tr}(-1n)$, the points at higher d values deviate more strongly than those at lower values.

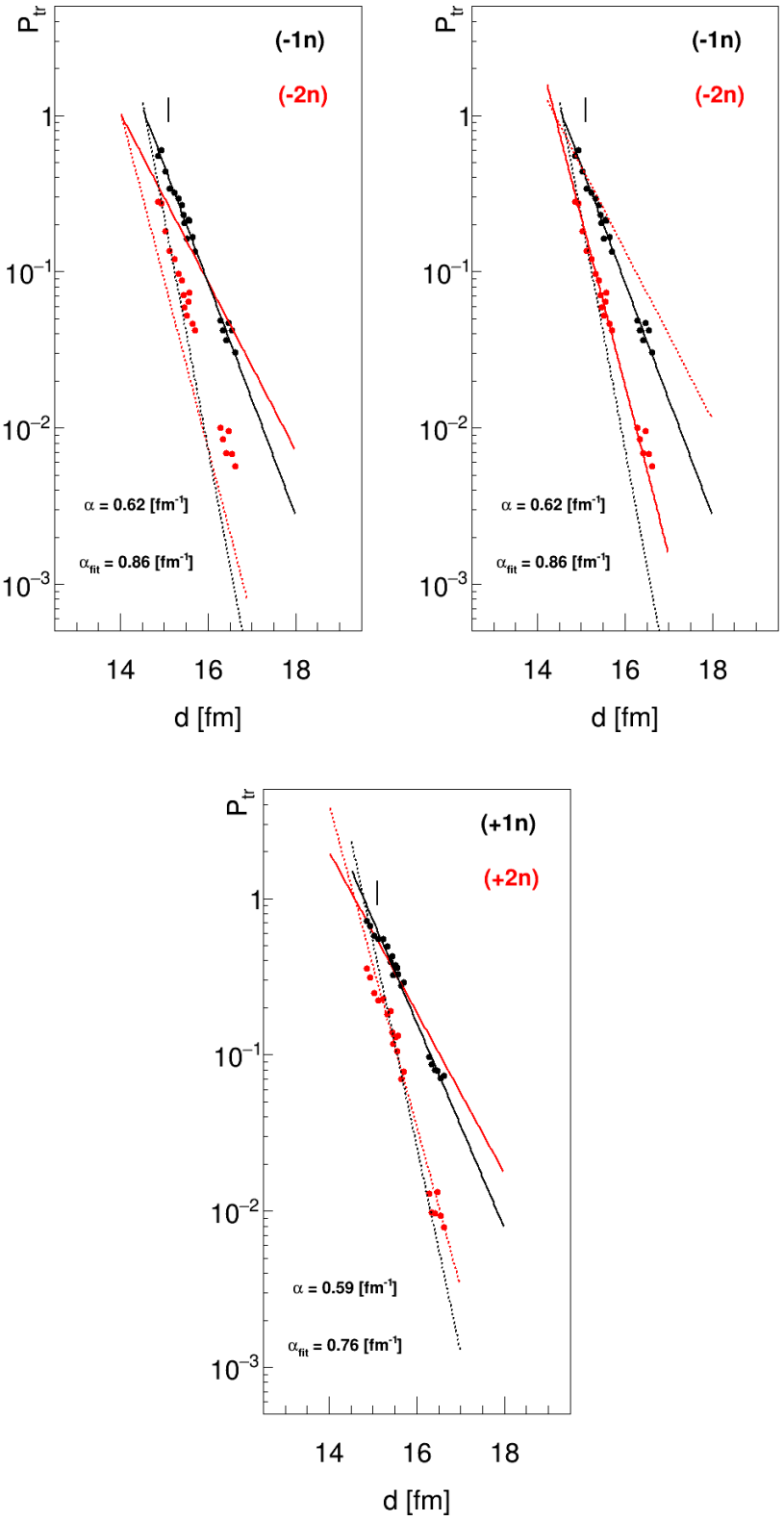

Figure 5.12: Experimental transfer probabilities (points) for (±1n) and (±2n) and ones calculated from the binding energy of (1n) channel (red solid lines) as well as ones obtain by fitting (1n) data (black solid lines). Dashed lines represent the square root of the calculated (red dash line) or fitted ones (black dash lines). The vertical line represent the position d which correspond to the energy calculated according to the Bass formula.

A similar analysis was conducted for proton transfer channels. Given that the Coulomb field varies between the entrance and exit channels due to charge transfer in these channels, we followed the methodology outlined in Ref. [95]. In this context, when calculating α, it is important to employ a modified equation which accounts for variations in the Coulomb field:

$$\alpha^2 = \frac{2m}{\hbar^2}\left(-B + \frac{Z_p Z_A e^2}{R(A)}\right). \tag{5.9}$$

In the formula above, the radius of the nuclei is calculated from the following equation:

$$R(A) = 1.07\left(1 + A^{1/3}\right) + 2.72. \tag{5.10}$$

Similar to the neutron transfer channels, when calculating α for a specific channel, the average value of the donor and receptor must be used. For example, for the (+1p) channel, the mean value of α for ^{206}Pb and ^{119}Sb should be considered, while for the (-1p) channel, the value of α for ^{207}Bi and ^{118}Sn must be taken into account. Calculated values for the projectile and target, as well as ions with one proton more or less, are presented in table 5.2. In the last two rows of the table, the values of α for the (+1p) and (-1p) channels have been calculated.

channel	R(fm)	S_p(MeV)	Ze^2/R (MeV)	$B + \left(Ze^2/R\right)$ (MeV)	α(fm^{-1})
$^{206}_{82}$Pb	10.1	7.25	11.7	21.7	1.02
$^{205}_{81}$Tl	10.0	6.42	11.6	17.7	0.931
$^{207}_{82}$Bi	10.1	3.56	11.8	15.4	0.861
$^{118}_{50}$Sn	9.04	10.0	7.97	15.2	0.857
$^{117}_{49}$In	9.02	7.52	7.82	15.3	0.860
$^{119}_{51}$Sb	9.05	5.11	8.11	13.22	0.799
		(-1p)	$\frac{1}{2}\left(\alpha(^{207}\text{Bi}) + \alpha(^{118}\text{Sn})\right)$		0.910
		(+1p)	$\frac{1}{2}\left(\alpha(^{206}\text{Pb}) + \alpha(^{119}\text{Sb})\right)$		0.859

Table 5.2: Calculations of α for proton transfer channels.

In figure 5.13 experimental data (points) for ($\pm$1p) and ($\pm$2p) channels are shown together with P_{tr} calculated from the binding energy for ($\pm$1p) with red lines, and the square of it

with red dash lines, as well as one obtain by fitting experimental (±1p) data (black solid lines) and the square of it (black dash lines).

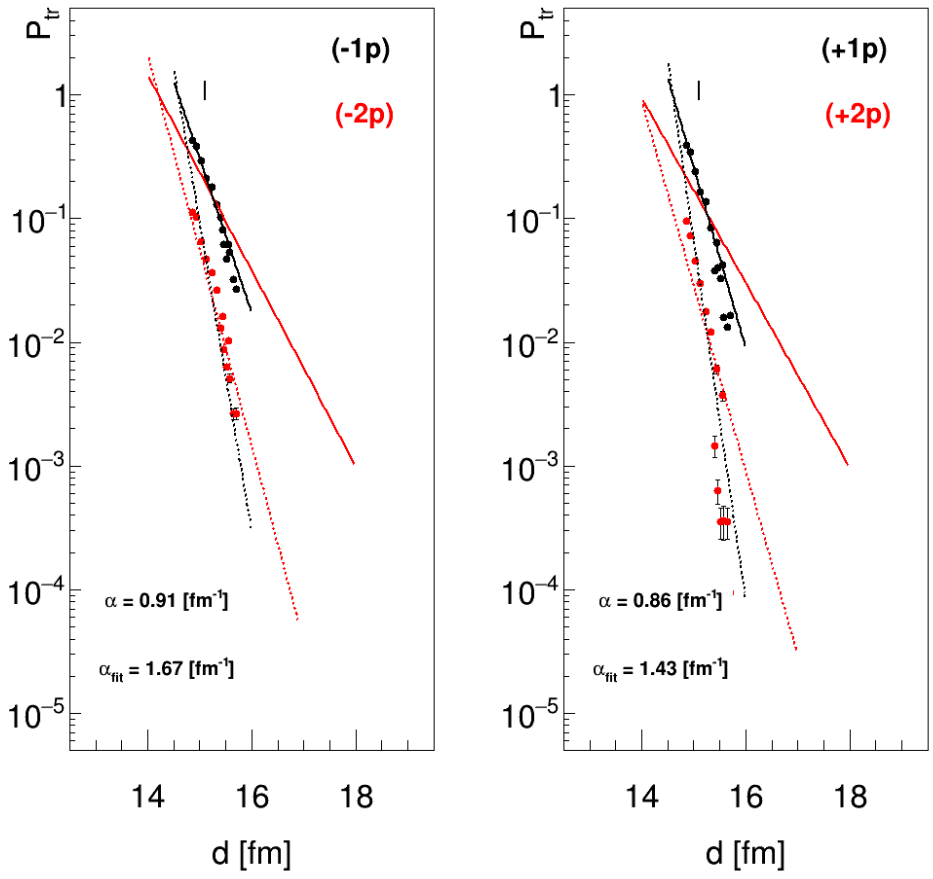

Figure 5.13: Experimental transfer probabilities (points) for (±1p) and (±2p) and ones calculated from the binding energy (red lines) as well as ones obtained by fitting (±1p) data (dashed lines). The vertical line represent the position of the barrier.

In the proton transfer channels, a difference between the calculated α and the one obtained through fitting ($A\exp(-2\alpha_{fit}d)$), for both pickup and stripping proton channels, is observed. These differences are larger than the ones for neutron transfer channels, while for neutron transfer channels they differ by 30-40 %, for proton transfer channels they differ 70-80 % from the calculated values. This could be because this "prescription" (as in Ref. [95]) does not fully account for the Coulomb field correction. In addition, in proton transfer channels, we have a TKEL with much higher energy loss, and we have included the entire Q-value spectra in P_{tr}. This can lead to a slope that significantly differs from the one obtained from the binding energy. Integrating large energy losses may lead to an apparent increase in cross-section, suggesting the need for a substantial EF to accurately

describe the data. However, this discrepancy between the experimental data and theoretical calculations is more likely attributable to the large Q-value tail within the range of significant energy losses, rather than to pairing correlations.
Regardless of the slope, it's evident that when we fit the function P_{tr} for (+1p) and (-1p) channels and square it (dashed lines), we observe a very good agreement with experimental data. From this, we can conclude that we do not need any enhancement factor (EF≈1) to describe the two-proton transfer channels.

Over the last few decades four-nucleon correlations forming an α-particle and the observation of the α-particle decay have triggered a number of publications which deal with the questions of the possible α-particle condensation in nuclei. Due to this it will be interesting to look into the $(\pm 2p \pm 2n)$ channels. We applied systematic approach, as described above, to analyze channels corresponding to the $(\pm 2p \pm 2n)$, which can be considered as "alpha" pick-up or stripping. The results are shown in Figure 5.14. The the red line presents tabulated slopes for the transfer of one proton and one neutron, while the amplitudes are obtained from the fits of the one-particle transfers (shown in Figures 5.12 and 5.13). Specifically, we used the formula:

$$P_{tr}(-2n-2p) = P_{tr}^2(-1n)P_{tr}^2(-1p). \tag{5.11}$$

The same procedure was performed with one-particle probabilities obtained from the fit, as indicated by the black lines.
It can be observed that such curves do not describe the results well, especially in the case of the (-2p-2n) channel. Therefore, it is necessary to introduce EFs. The dashed curves were obtained by fixing the slope (as in table 5.1 and 5.2) and amplitude parameters to those obtained for one-particle transfers, while leaving the EF factor free. The estimated EFs using this method are EF≈30 for (-2p-2n) and around EF≈3 for (+1p+1n). The calculations multiplied by EF are shown in figure 5.14 with red dashed lines.
We can also observe that data corresponding to lower energies has a slightly higher α compared to those at higher energies. In other words, the points at higher energies have a slope similar to the one calculated from the binding energy, while the points at lower energies have a slope closer to the fitted values.
If we examine the Q-value spectra for these channels (see Fig. 5.15), we can see that

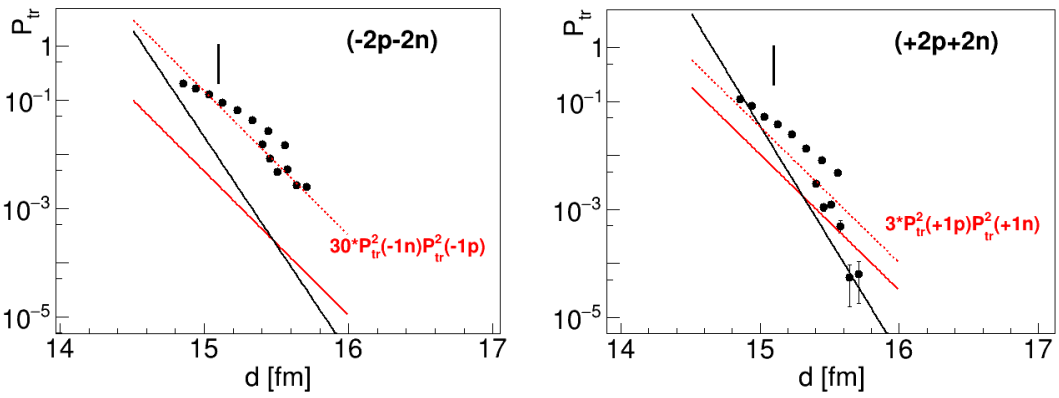

Figure 5.14: Experimental transfer probabilities (points) for (-2p-2n) and (+2p+2n) and ones calculated from the binding energy for one-particle transfers (red solid lines) as well as ones obtain by fitting data from one-particle transfers (black solid lines). The dashed red lines represent the red solid line multiplied by the factor 30 (-2p-2n) and 3 (+2p+2n). The vertical line represent position d which correspond to the energy calculated according to the Bass formula.

the peak positions are more centered around the ground-to-ground Q_0-value position for the lower beam energy, which is 1090 MeV in ($\pm$2p$\pm$2n) transfer channels, due to low statistics in 1035 MeV (which corresponds to larger distances of closest approach).

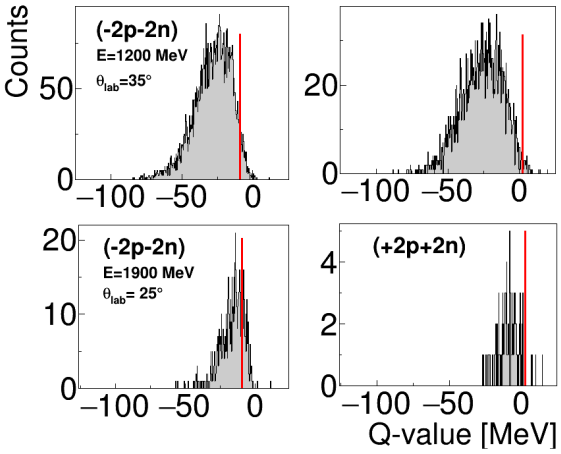

Figure 5.15: Q-value distributions for ($\pm$2p$\pm$2n) transfer channels for labeled transfer channel and energy- angle configuration (divided by factor 2). The spectra were contracted from integration of whole angular range.

In contrast, for lower d, the peaks are shifted towards higher energy losses, and they are significantly wider. What can be concluded is that points corresponding to narrow, and centered around Q_0, Q-value distributions, should have "more accurate" P_{tr} values. However, for the (+2p+2n) channel, where the slopes of points from the two beam energies differ significantly, there are also considerable statistical errors for the larger d, which

complicates and increases the error in slope determination.

5.2.1 Comparison to other systems

To gain further insights, we compare our results with those from different systems. Particularly, in reference [56], a systematic comparison of experimentally obtained EFs was presented for various systems. The P_{tr} from the systematic comparison, at Ref.[56], are constructed at the same value of d_0 for easier comparison of different systems. For neutron transfer channels values d_0 =1.5 and 1.6 fm are used, and for proton transfer channels value d_0 =1.45 fm is used. However, d_0 =1.45 fm is not the value at which the maximum probability for charged particle transfer is observed. These absolute probabilities for the transfer were compared with values for neutron transfer in the region with d_0 =1.6, where the same internal barrier height are observed. The EF for (2n) channel ranges from 1 to 10, while for (2p) the spread of EF is larger, it ranges from 3 to 40.

In Ref. [56], the cross sections used in P_{tr} construction, are expected to exhibit variations of up to a factor of 2 due to their definition, which includes a summation of the cross-sections measured for individual states at lower excitation energy levels.

Enhanced two-neutron transfers (EF $\approx$ 3–4) are particularly noticeable in systems with $Q_0 \approx 0$ or $Q_0 < 0$, where a kinematic restriction to low-lying states is enforced. Notably, EF = 1 is consistently observed for cases with closed shells.

Results for "cold transfer" reactions, where measurements use the multiplicity filter (like the ^{206}Pb+ ^{118}Sn system discussed in chapter 1), are excluded from their compilation as they used the microscopic definition of enhancement, considering only single states.

In the ^{208}Pb+ ^{144}Sm [96] and ^{144}Sm + ^{88}Sr [97] systems, where both systems were measured at the UNILAC at GSI with the magnetic spectrometer, the EF for (+2n) channel were found to be 1 and for (+2p) 8 an 10 respectably. The system ^{208}Pb+ ^{144}Sm involves a double magic nuclei (^{208}Pb) and one with closed neutron but open proton shells (^{144}Sm). In the ^{144}Sm + ^{88}Sr system, both nuclei have a closed neutron shell, but open proton shells. However, it's important to note that nuclear structure can be more complex than traditional magic numbers suggest, and additional factors beyond magic numbers can define the shape of the nuclei as well as the collectivity and excitations.

In figures 5.16, 5.17 and 5.18 our results are compared with these systems, together with the more recently measured systems, the ^{116}Sn+ ^{60}Ni and ^{96}Zr+ ^{40}Ca, where EF was found to be 5.5, and 3 for neutron transfer channels. The behavior of all studied channels within all systems, especially at the ^{206}Pb+ ^{118}Sn, ^{208}Pb+ ^{144}Sm and ^{144}Sm + ^{88}Sr

systems which have similar mass, are in agreement.

In table 5.3, 5.4 and 5.5 expected slopes $\alpha \cdot (A_1^{1/3} + A_2^{1/3})$ for the one-particle transfer channels are calculated for each compared system. For example, in the case of the (+1n) channel, we can see that the ^{96}Zr + ^{40}Ca system exhibits the smallest slope, as we would expect based on the calculation. In the (+2n) channel, one expects that the slope will follow the trend $\alpha_{2n} \approx 2 * \alpha_{1n}$.

system	$\alpha(\mathrm{fm}^{-1})$	$\alpha \cdot (A_1^{1/3} + A_2^{1/3})$
^{206}Pb+ ^{118}Sn	0.592	6.40
^{116}Sn+ ^{60}Ni	0.646	5.68
^{96}Zr+ ^{40}Ca	0.625	5.00
^{208}Pb+ ^{144}Sm	0.583	6.51

Table 5.3: Calculations of α for (+1n) transfer channel for different systems.

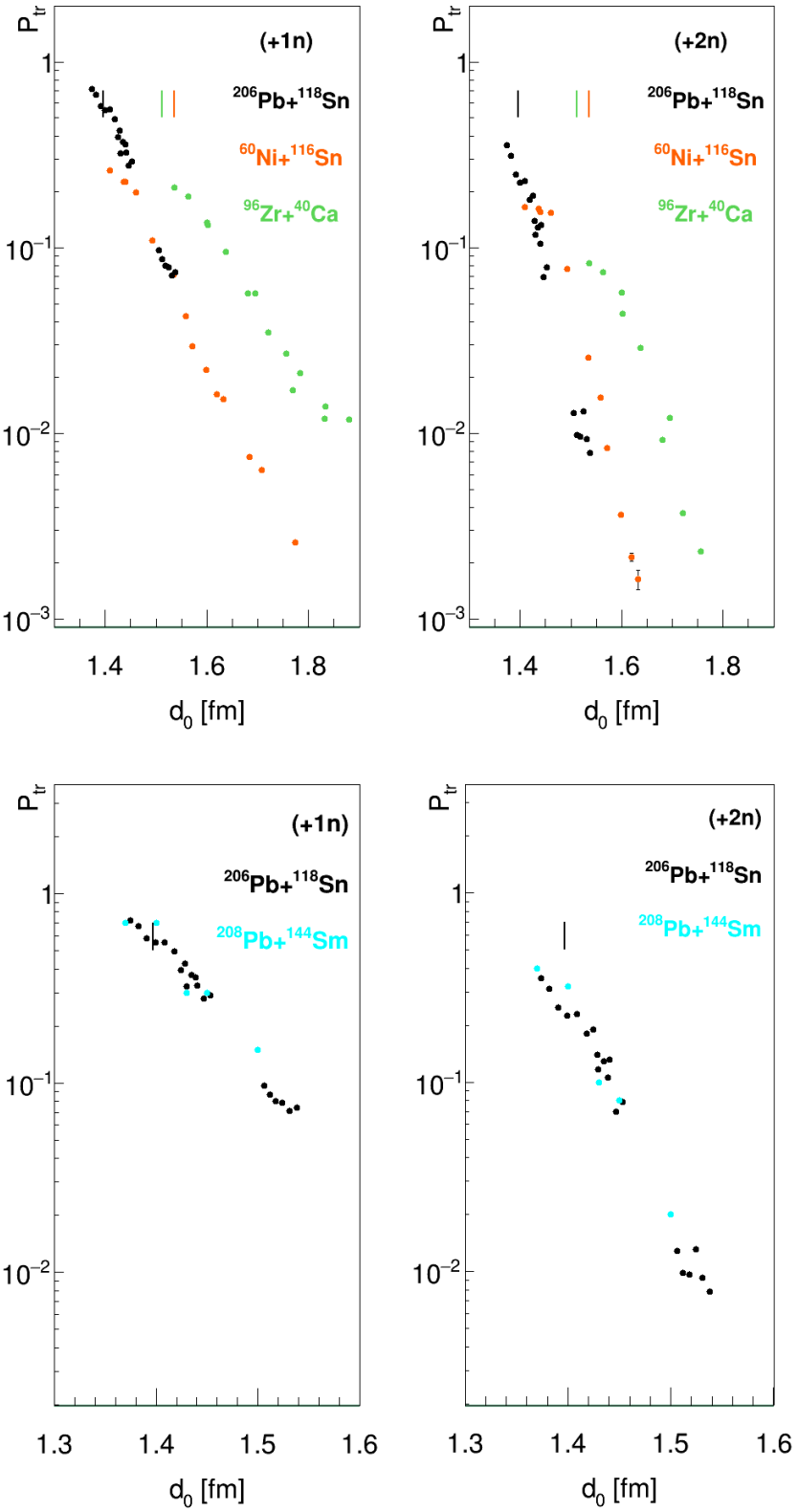

Figure 5.16: Experimental transfer probabilities for (+1n) and (+2n) channels in ^{206}Pb+ ^{118}Sn (black), ^{116}Sn+ ^{60}Ni (orange), ^{96}Zr+ ^{40}Ca (green), and ^{208}Pb+ ^{144}Sm (blue) plotted as a function of the reduced distance of closest approach, $d_0 = d/(A_1^{1/3} + A_2^{1/3})$. The vertical line represents the position d which corresponds to the energy calculated according to the Bass formula.

Similar situation can be observed in (-1p) and (+1p) channels where one can observe a good agreement in the results between systems where we expect to have a similar slope. Such comparisons provide additional confirmation of our results.

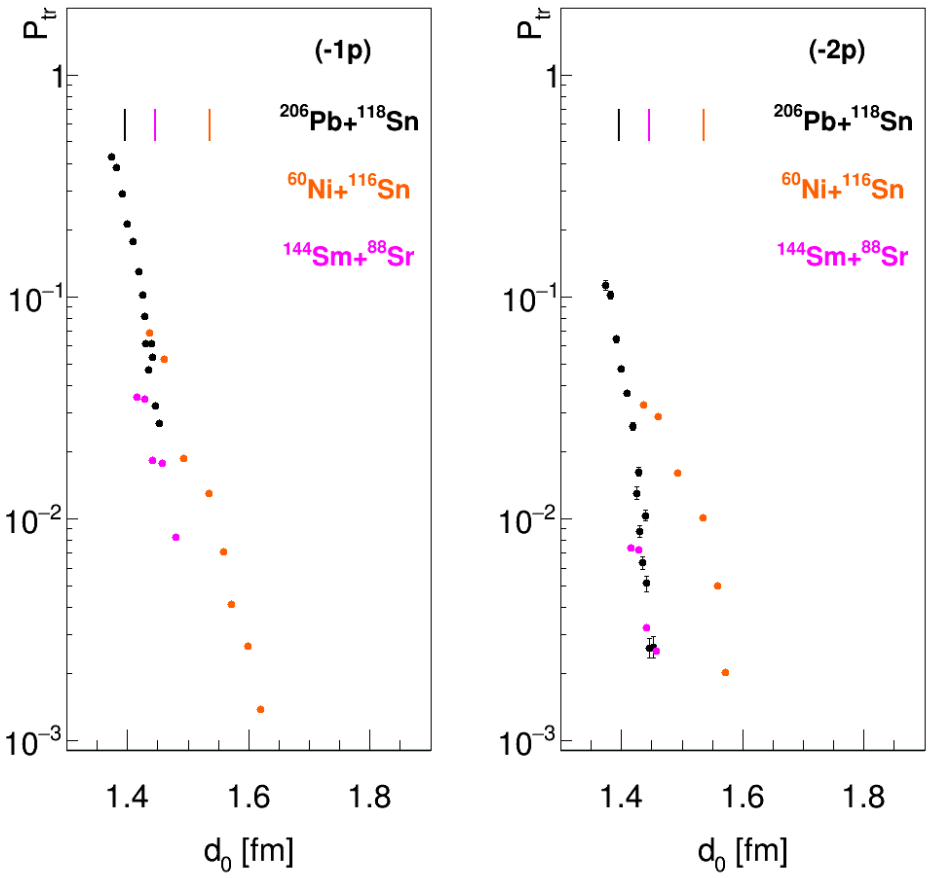

Figure 5.17: Experimental transfer probabilities for (-1p) and (-2p) channels in ^{206}Pb+ ^{118}Sn (black), ^{116}Sn+ ^{60}Ni (orange), and ^{144}Sm + ^{88}Sr (pink) plotted as a function of the reduce distanced of the closest approach, $d_0 = d/(A_1^{1/3} + A_2^{1/3})$. The vertical line represents the position d which corresponds to the energy calculated according to the Bass formula.

system	$\alpha(\mathrm{fm}^{-1})$	$\alpha \cdot (A_1^{1/3} + A_2^{1/3})$
^{206}Pb+ ^{118}Sn	0.910	9.84
^{116}Sn+ ^{60}Ni	0.765	6.55
^{144}Sm+ ^{88}Sr	0.896	8.51

Table 5.4: Calculations of α for (-1p) transfer channel for different systems.

system	$\alpha(\mathrm{fm}^{-1})$	$\alpha \cdot (A_1^{1/3} + A_2^{1/3})$
^{206}Pb+ ^{118}Sn	0.859	9.49
^{208}Pb+ ^{144}Sm	0.809	9.03
^{144}Sm+ ^{88}Sr	0.781	7.56

Table 5.5: Calculations of α for (+1p) transfer channel for different systems.

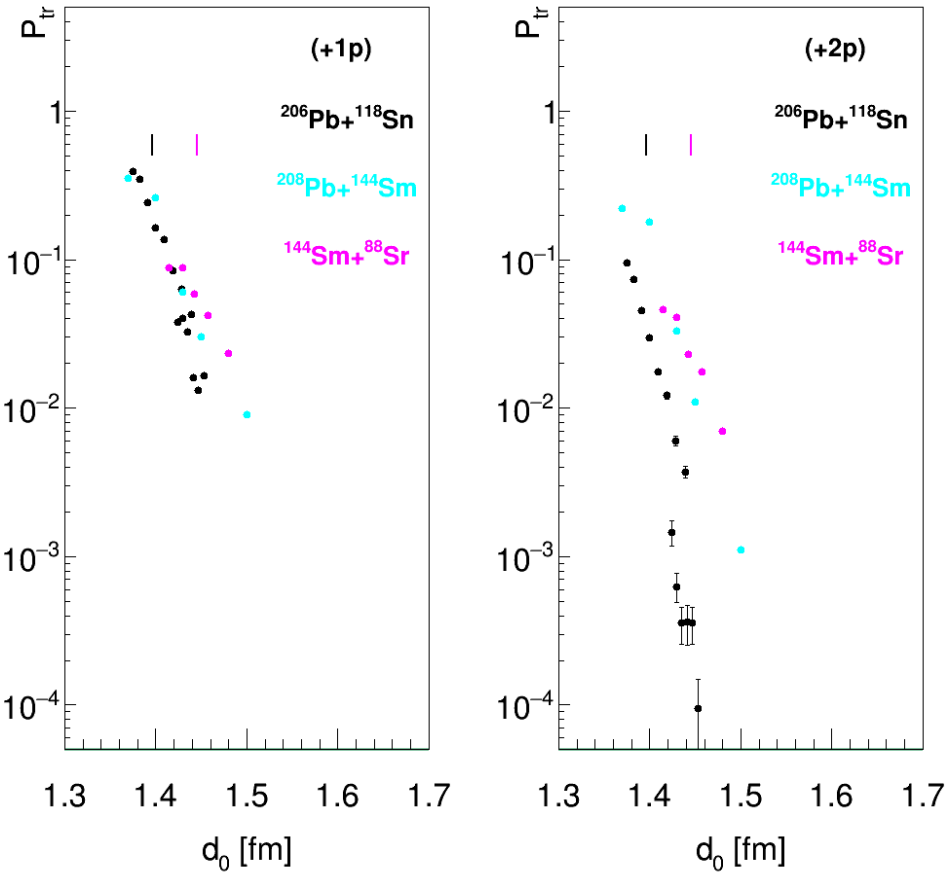

Figure 5.18: Experimental transfer probabilities for (+1p) and (+2p) channels in ^{206}Pb+ ^{118}Sn (black), ^{144}Sm + ^{88}Sr (pink) and ^{208}Pb+ ^{144}Sm (blue) plotted as a function of the reduce distance of the closest approach, $d_0 = d/(A_1^{1/3} + A_2^{1/3})$. The vertical line represents the position d which corresponds to the energy calculated according to the Bass formula.

5.2.2 Comparison to the GRAZING calculations

In this section, we will compare the GRAZING calculations with experimental data for neutron and proton transfer channels.

In figures 5.19, 5.20, 5.22 the comparison of P_{tr} for elastic+inelastic (0n), neutron transfers ($\pm$1n) and ($\pm$2n), and proton transfer ($\pm$1p) and ($\pm$2p) channels, is given together with GRAZING calculations. The light green lines represent the GRAZING calculations for P_{tr}, which is by definition the cross section of a certain channel over the Rutherford cross section, while the dark green lines represent the ratio of the GRAZING calculation for P_{tr}, for a certain channel, over the (0n) channel.

GRAZING calculations agree well with the elastic+inleastic channel, measured for different bombarding energies and angular and magnetic setting.

For small distances of closest approach, and for experimental points extracted only for small energy losses, GRAZING describes well the fall-off. Furthermore, for energies close to the turning point, the experimental points extracted from the two measured energies, 1182 and 1090 , overlap well. At the lowest measured energy of 1035 MeV, at the largest measured distances of closest approach one can observe that almost all measured yields correspond to the Rutherford cross section.

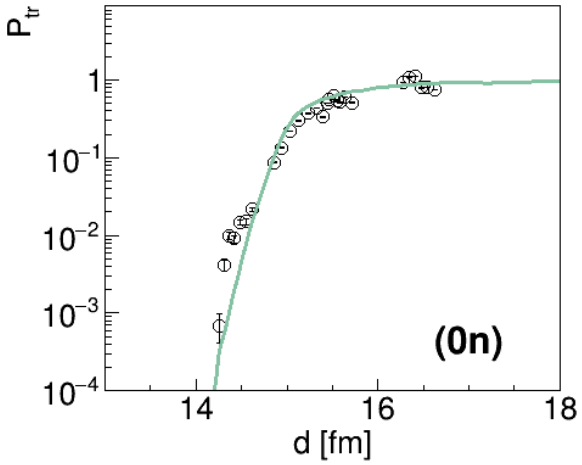

Figure 5.19: Experimental transfer probabilities as a ratio over Rutherford cross section (empty circles) for the elastic+inelastic channel are plotted together with GRAZING calculations (lines).

A similar conclusion can be drawn when looking at the neutron transfer channels (Figure 5.20), where for the lowest energy (corresponding to points at large d values), ones can observe that the points corresponding to the P_{tr} data and those obtained as the ratio over

Rutherford cross section are in good agreement. However, this is not the case for higher energies where the differences become evident. This region where they begin to differ can be characterized as the region where absorption starts. Thus, we would like to underline the importance of measurements at low energies. This region of the distances of closest approach will be very important in the correct definition of the EF.

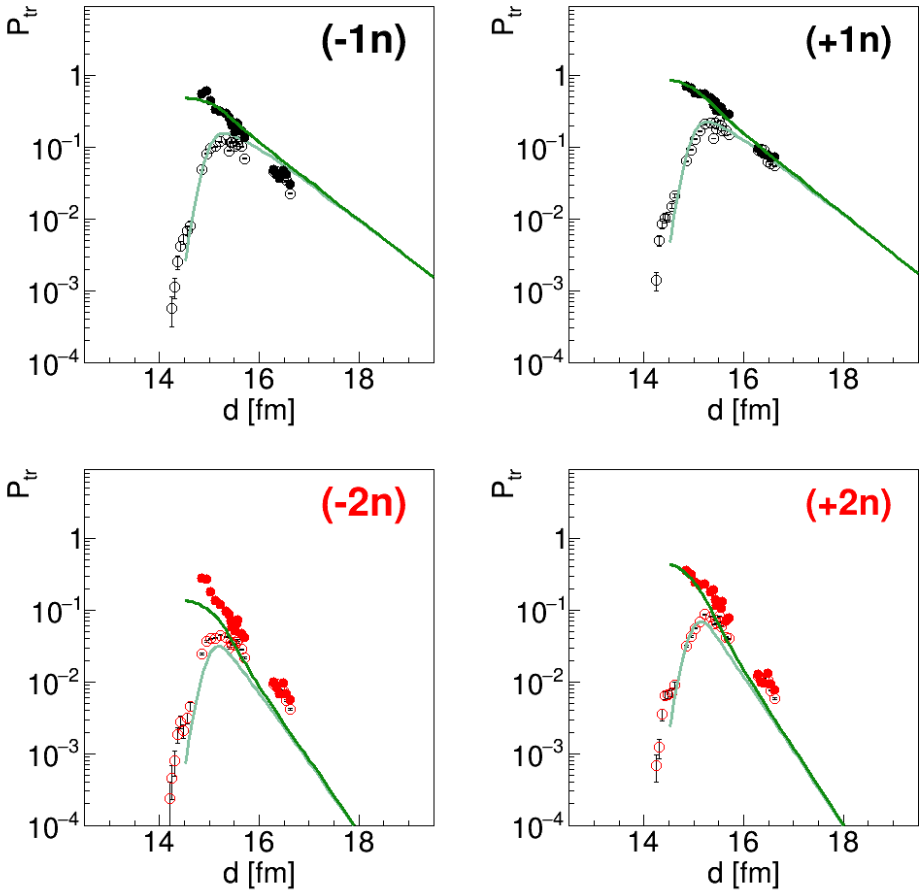

Figure 5.20: Experimental transfer probabilities (full points) for neutron transfer channels, and ones plotted as a ratio over Rutherford cross section (empty circles) compared with GRAZING calculations (lines). The light green lines represent the GRAZING calculations for P_{tr} while the dark green lines represent the ratio of the GRAZING calculation for P_{tr} over the ones for (0n) channel.

In the case of all neutron transfer channels (Figure 5.20), a very good agreement with theory was observed. It's interesting to note that both the peak position and shape match the calculations. For all neutron transfer channels the GRAZING describes well the absolute values of transfer probabilities. Taking into account that the two-nucleon transfer channels are treated as an independent nucleon transfer in GRAZING, the good agreement between the calculations and data suggests that we do not need any additional

enhancement factors.

It has already been mentioned, for neutron channels, the integration was done only for a part of the Q-value distribution corresponding to the quasi-elastic part. In Figure 5.21, a comparison of experimental (empty histograms) and GRAZING calculation (filled histograms) of total kinetic energy loss TKEL (TKEL=-Q-value) distributions for neutron transfer channels at E_{lab} =1090 MeV is given. A good agreement can be noticed in the widths of the distributions as well as in the position of the peaks for most neutron channels. Dashed lines indicate the position in the distribution up to which we integrated the quasi-elastic part.

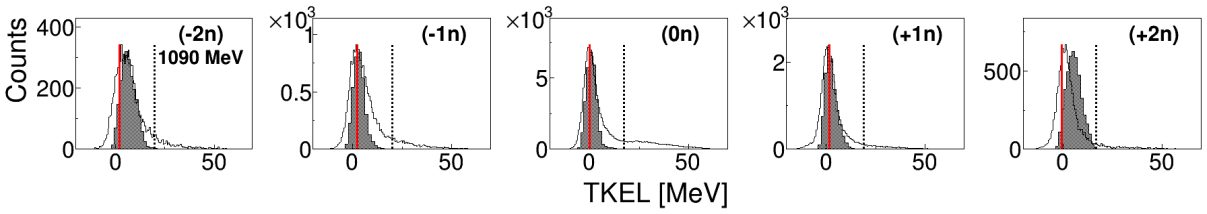

Figure 5.21: Experimental (empty histograms) and GRAZING (filled histograms) TKEL distributions for neutron transfer channels for $E_{lab} = 1090$ MeV. Dashed lines indicate the position in the distribution up to which we integrated the quasi-elastic part. Red lines indicate the ground-to-ground state TKEL values.

A slightly different scenario, in terms of transfer probabilities, can be seen in the case of proton transfer channels. In proton stripping channels, (-1p) and (-2p) (Fig. 5.22), one can observe a good agreement in terms of peak shape and peak position, while the absolute value for the two-proton stripping is underestimated. In the case of proton pick-up channels, alignment in the peak position is visible, but the data shape corresponding to lower energy (1090 MeV) displays a different slope. It's noticeable that in these channels, GRAZING underestimates the transfer probability for both one and two proton pick-up.

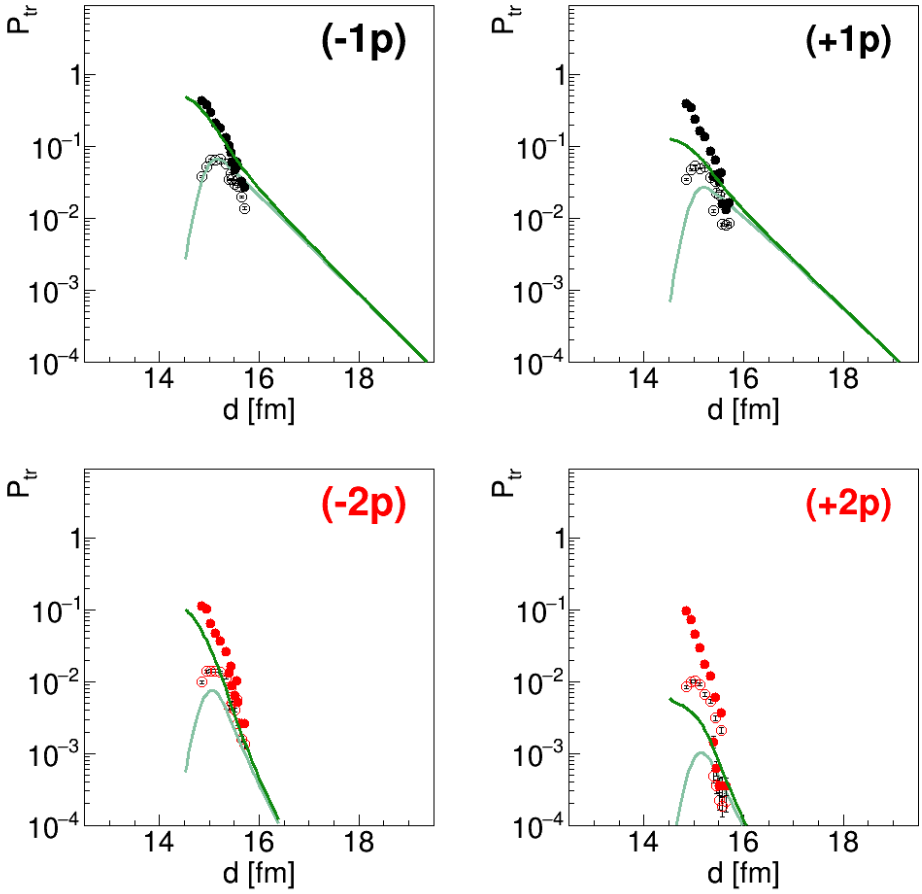

Figure 5.22: Experimental transfer probabilities (full points) for proton transfer channels, and ones plotted as a ratio over Rutherford cross section (empty circles) compared with GRAZING calculations (lines). The light green lines represent the GRAZING calculations for P_{tr} while the dark green lines represent the ratio of the GRAZING calculation for P_{tr} over the ones for (0n) channel.

The slope is not well described by GRAZING, which is an indicator that direct transfers are not observed, i.e., that significant energy losses are encountered in the measured Ptr. In addition, the absolute value is also not well described, which can give the misleading impression that EF>1 is required. On the other hand, for proton transfers, points at large distances of closest approach (well outside of the absorption region) are not available, so definitive conclusions cannot yet be drawn. In order to do so, future measurements at lower energies are required.

Conclusion

Multineutron transfer channels have been successfully measured with high resolution in the ^{206}Pb+^{118}Sn system at E_{lab}=1200 MeV, E_{lab}=1090 MeV and E_{lab}=1035 MeV for nuclei in the A $\sim$ 118 mass range. Additionally, for beam energies E_{lab}=1200 MeV and 1090 MeV, multiproton-transfer channels were also studied. Such conditions correspond to the region from above to below the barrier. The light Sn-like fragments were detected in PRISMA where they were identified in their nuclear charge, mass and kinetic energy. After completing the analysis, where the final goal was to obtain ion identification, we were able to make several conclusions from the obtained results.

The most significant contributions of this dissertation can be categorized into two main groups. The first important contribution shows how the dynamics of the reaction evolves across the wide range of angles. The Wilczynski plots we obtained allow visualization of the transition from quasi-elastic to deep inelastic regimes [92]. The second important contribution relates to the study of pairing correlations in multi-nucleon transfer reactions, mainly of neutrons.

The dynamics were studied from the dependence of the Q-value distributions on the scattering angle, of certain transfer channels. This evolution of Q-value distributions can be related to the behavior of the extracted differential and total cross sections. At least for few nucleon transfer channels the main observables such as Q-values and cross sections, retain the main characteristics of direct processes. For the transfer channels involving many nucleons, the large energy loss unavoidably leads to a reshuffling in the final yield distributions. By comparing the experimental cross-sections with calculations performed using the GRAZING code, a good agreement was found for most of the few nucleon transfer channels. This high level of agreement confirms the accuracy of both the employed nuclear potential and the selected range of partial waves contributing to the

cross-sections, even in the context of the heavy system under investigation. Contrariwise, the consistent trend of underestimating yields as additional nucleon transfers come into play suggests the involvement of more complex processes. These processes might not be well taken into account by the applied theoretical model. In addition, there is an urgent need for further research on the proton transfers, with a specific focus on enhancing their theoretical representation and understanding. This, in particular, will be very important for the proton pick-up channels, which leads to the population of heavy neutron rich nuclei.

Pairing correlations were examined by studying the transfer probabilities as a function of the distance of the closest approach. Transfer probabilities were constructed for each transfer channel as the ratio of the yields in the transfer channel and the elastic+inelastic channel.

In neutron pick up channels we obtained a rather good agreement between the calculated slope α, via binding energy, and the one obtained from the fitting procedure, for both (+1n) and (+2n) channels, while for (-1n) and (-2n) the slopes differ more. By comparison of transfer probabilities of two-neutron transfers with probabilities of one-neutron transfers, we concluded that the probabilities for two-neutron transfers can be explained by the transfer of independent neutrons. In other words, there was no need for the enhancement factors, at least for the quasi-elastic part. A similar conclusion was reached for the channels which involved the transfer of protons. However, the presence of large kinetic energy loss may blur this conclusion.

By comparing experimental data with the GRAZING code prediction, a very good agreement was observed both in shapes, as well as in absolute values. As the GRAZING code calculates only the independent nucleon transfer, this finding may suggest that the transfer of correlated neutrons do not participate significantly to the cross sections of the two-neutron transfer channels.

In future research, it would be interesting to compare data with different models and calculations, in particular with ones which include the large energy loss contributions. This will be very important in order to understand how the secondary processes (like neutron evaporation or fission) change the differential and total cross sections. This, in turn, will be important to correctly predict the expected production of the neutron rich

nuclei, and in particular for heavy neutron rich ones.

Concerning the transfer of correlated nucleons and the study of pairing correlations in general, it would be interesting to perform additional measurements where the cross section of different states can be evaluated, as is the case in particle-gamma coincident measurements. For example, such an experiment can be performed by using the PRISMA+AGATA configuration [98]. In that way it would be possible to study the distribution of transfer strength over the different excited states as well as ground state, and also how such strenght distribution changes with energy from above to below the Coulomb barrier.

A Appendix

In this appendix, tables of results are listed. The differential cross-sections (DCS) for channels ranging from (-2p-2n) to (+2p+2n) at beam energy of 1200 MeV are provided, as well as the DCS for neutron channels, (-2n) to (+2n), at lower energies (1090 and 1035 MeV) (in A.1). Additionally, a table of total cross-sections (TCS) at 1200 MeV is included (in A.2). Probabilities for neutron transfer channels ($\pm$1n) and ($\pm$2n), along with those for protons transfer channels ($\pm$1p) and ($\pm$2p), are also listed (in A.3).

A.1 Differential cross sections (DCS)

Z	A	θ_{cm}	DCS (mb/sr)	error (mb/sr)
48	114	118.542	3.8	0.1
48	114	116.564	5	0.2
48	114	114.586	6.6	0.2
48	114	112.608	6.5	0.2
48	114	110.631	6.3	0.2
48	114	108.655	5.1	0.2
48	114	106.679	3.9	0.1
48	114	104.704	2.4	0.1
48	115	118.253	3.1	0.1
48	115	116.263	4.2	0.1
48	115	114.273	5.4	0.2
48	115	112.284	5.3	0.2
48	115	110.295	5.3	0.2
48	115	108.306	4.6	0.2
48	115	106.317	3.3	0.1
48	115	104.329	2.3	0.1

Table A.1: Differential cross sections for $Z = 48$ for E_{lab} =1200 MeV.

Z	A	θ_{cm}	DCS (mb/sr)	error (mb/sr)
48	116	118.092	2.1	0.1
48	116	116.096	3.1	0.1
48	116	114.1	3.3	0.1
48	116	112.103	3.5	0.1
48	116	110.107	3.5	0.1
48	116	108.111	3.1	0.1
48	116	106.116	2.4	0.1
48	116	104.12	1.71	0.1
48	117	117.755	1.14	0.07
48	117	115.745	1.48	0.08
48	117	113.735	1.69	0.09
48	117	111.725	1.72	0.09
48	117	109.714	1.69	0.09
48	117	107.703	1.69	0.09
48	117	105.692	1.08	0.07
48	117	103.681	0.88	0.07
48	118	117.576	0.4	0.04
48	118	115.559	0.59	0.05
48	118	113.541	0.72	0.06
48	118	111.524	0.67	0.06
48	118	109.505	0.75	0.06
48	118	107.487	0.7	0.06
48	118	105.467	0.56	0.05
48	118	103.448	0.41	0.05

Table A.2: Differential cross sections for $Z = 48$ for E_{lab} =1200 MeV.

Z	A	θ_{cm}	DCS (mb/sr)	error (mb/sr)
49	115	118.386	8.0	0.2
49	115	116.401	10.3	0.2
49	115	114.417	11	0.2
49	115	112.433	11.5	0.2
49	115	110.449	11.5	0.2
49	115	108.466	10	0.2
49	115	106.483	7.7	0.2
49	115	104.501	6.4	0.2
49	116	118.129	8.7	0.2
49	116	116.135	11.4	0.2
49	116	114.14	13.2	0.3
49	116	112.145	14.2	0.3
49	116	110.151	15.3	0.3
49	116	108.156	12.6	0.3
49	116	106.162	10.1	0.2
49	116	104.168	7.9	0.2
49	117	117.974	8	0.2
49	117	115.973	11.5	0.2
49	117	113.972	15	0.3
49	117	111.971	15.6	0.3
49	117	109.97	17.1	0.3
49	117	107.969	15.4	0.3
49	117	105.968	11.8	0.2
49	117	103.967	10.1	0.2
49	119	117.501	2.3	0.1
49	119	115.481	3.4	0.1
49	119	113.46	4.1	0.1
49	119	111.439	4 .0	0.1
49	119	109.418	4.3	0.1
49	119	107.396	3.8	0.1
49	119	105.373	2.4	0.1
49	119	103.35	1.8	0.1

Table A.3: Differential cross sections for $Z = 49$ for E_{lab} =1200 MeV.

Z	A	θ_{cm}	DCS_{cut} (mb/sr)	error (mb/sr)	DCS (mb/sr)	error (mb/sr)
50	116	138.096	0.04	0.03		
50	116	136.101	0.07	0.04		
50	116	134.106	0.14	0.05		
50	116	132.111	0.29	0.07		
50	116	130.117	0.46	0.09		
50	116	128.122	0.37	0.08		
50	116	126.127	0.52	0.1		
50	116	124.133	0.8	0.1		
50	116	118.15	5.2	0.2	15.1	0.3
50	116	116.156	8.3	0.2	16.3	0.3
50	116	114.162	9.3	0.2	17.0	0.3
50	116	112.168	10.0	0.2	16.7	0.3
50	116	110.175	11.6	0.2	17.9	0.3
50	116	108.181	11.4	0.2	16.9	0.3
50	116	106.188	10.3	0.2	13.9	0.3
50	116	104.195	10.7	0.2	12.6	0.3

Table A.4: Differential cross sections for $Z = 50$ for E_{lab} =1200 MeV, also with integration of elastic part of Q-value.

Z	A	θ_{cm}	DCS$_{cut}$ (mb/sr)	error (mb/sr)	DCS (mb/sr)	error (mb/sr)
50	117	136.085	0.09	0.04		
50	117	134.09	0.16	0.05		
50	117	132.094	0.4	0.09		
50	117	130.098	0.7	0.1		
50	117	128.103	0.9	0.1		
50	117	126.108	1.2	0.1		
50	117	124.112	1.4	0.2		
50	117	118.127	10.4	0.2	48.1	0.5
50	117	116.132	18.2	0.3	54.9	0.5
50	117	114.137	22.7	0.3	48.6	0.5
50	117	112.142	25.0	0.4	45.9	0.5
50	117	110.148	30.6	0.4	51.6	0.5
50	117	108.153	34.5	0.4	52.3	0.5
50	117	106.159	33.4	0.4	46.9	0.5
50	117	104.165	35.7	0.4	46.4	0.5

Table A.5: Differential cross sections for $Z = 50$ for E_{lab} =1200 MeV, also with integration of elastic part of Q-value.

Z	A	θ_{cm}	DCS$_{cut}$ (mb/sr)	error (mb/sr)	DCS (mb/sr)	error (mb/sr)
50	119	135.803	0.2	0.06		
50	119	133.793	0.7	0.1		
50	119	131.782	1.4	0.2		
50	119	129.772	1.8	0.2		
50	119	127.762	1.8	0.2		
50	119	125.751	2.7	0.2		
50	119	123.74	4.0	0.3		
50	119	117.706	13.4	0.3	29.7	0.4
50	119	115.694	20.2	0.3	41.8	0.5
50	119	113.682	29.7	0.4	57.5	0.5
50	119	111.67	40.5	0.4	69.4	0.6
50	119	109.657	53.0	0.5	84.0	0.6
50	119	107.644	58.1	0.5	84.0	0.7
50	119	105.631	61.8	0.6	80.3	0.6
50	119	103.617	59.4	0.6	71.4	0.6

Table A.6: Differential cross sections for $Z = 50$ for E_{lab} =1200 MeV, also with integration of elastic part of Q-value.

Z	A	θ_{cm}	DCS$_{cut}$ (mb/sr)	error (mb/sr)	DCS (mb/sr)	error (mb/sr)
50	120	135.711	0.09	0.04		
50	120	133.696	0.21	0.06		
50	120	131.681	0.5	0.1		
50	120	129.666	1.0	0.1		
50	120	127.651	1.1	0.1		
50	120	125.635	1.3	0.2		
50	120	123.619	1.7	0.2		
50	120	117.569	6.7	0.2	15.1	0.3
50	120	115.552	9.4	0.2	17.7	0.3
50	120	113.534	12.8	0.2	21.7	0.3
50	120	111.516	16.4	0.3	24.6	0.3
50	120	109.498	21.9	0.3	29.7	0.4
50	120	107.479	21.4	0.3	27.8	0.4
50	120	105.459	20.2	0.3	24.4	0.4
50	120	103.439	17.4	0.3	19.9	0.3

Table A.7: Differential cross sections for $Z = 50$ for E_{lab} =1200 MeV, also with integration of elastic part of Q-value.

Z	A	θ_{cm}	DCS (mb/sr)	error (mb/sr)
51	117	118.024	5.7	0.2
51	117	116.025	7.7	0.2
51	117	114.026	7.8	0.2
51	117	112.027	6.9	0.2
51	117	110.028	5.9	0.2
51	117	108.029	6.0	0.2
51	117	106.03	6.4	0.2
51	117	104.031	4.8	0.2
51	118	117.915	10.9	0.2
51	118	115.912	15.5	0.3
51	118	113.908	17.7	0.3
51	118	111.905	16.9	0.3
51	118	109.901	17.7	0.3
51	118	107.897	12.7	0.3
51	118	105.893	12.6	0.3
51	118	103.889	10.5	0.2
51	119	117.663	7.3	0.2
51	119	115.65	10.5	0.2
51	119	113.636	12.4	0.2
51	119	111.622	12.0	0.2
51	119	109.607	13.1	0.3
51	119	107.592	9.9	0.2
51	119	105.577	9.2	0.2
51	119	103.562	7.0	0.2

Table A.8: Differential cross sections for $Z = 51$ for E_{lab} =1200 MeV.

Z	A	θ_{cm}	DCS (mb/sr)	error (mb/sr)
51	120	117.535	6.1	0.2
51	120	115.516	8.4	0.2
51	120	113.497	9.7	0.2
51	120	111.478	9.5	0.2
51	120	109.458	9.9	0.2
51	120	107.437	7.5	0.2
51	120	105.416	5.9	0.2
51	120	103.394	4.2	0.1
51	121	117.26	4.7	0.1
51	121	115.23	5.6	0.2
51	121	113.2	6.8	0.2
51	121	111.169	6.3	0.2
51	121	109.137	6.5	0.2
51	121	107.104	5.0	0.2
51	121	105.07	4.6	0.2
51	121	103.035	3.1	0.1

Table A.9: Differential cross sections for $Z = 51$ for E_{lab} =1200 MeV.

Z	A	θ_{cm}	DCS (mb/sr)	error (mb/sr)
52	118	117.729	0.88	0.06
52	118	115.719	0.91	0.07
52	118	113.707	0.95	0.07
52	118	111.696	0.77	0.06
52	118	109.685	0.57	0.05
52	118	107.673	0.5	0.05
52	118	105.66	0.4	0.05
52	118	103.648	0.23	0.03
52	119	117.53	1.35	0.08
52	119	115.511	1.67	0.09
52	119	113.492	1.66	0.09
52	119	111.472	1.44	0.08
52	119	109.452	1.16	0.08
52	119	107.431	0.82	0.06
52	119	105.41	0.61	0.06
52	119	103.388	0.46	0.05
52	120	117.484	1.78	0.09
52	120	115.464	2.2	0.1
52	120	113.442	2.3	0.1
52	120	111.421	2.2	0.1
52	120	109.398	1.69	0.09
52	120	107.376	1.44	0.09
52	120	105.352	0.88	0.07
52	120	103.328	0.61	0.06

Table A.10: Differential cross sections for $Z = 52$ for E_{lab} =1200 MeV.

Z	A	θ_{cm}	DCS (mb/sr)	error (mb/sr)
52	121	117.24	2.1	0.1
52	121	115.21	2.6	0.1
52	121	113.178	3	0.1
52	121	111.146	2.7	0.1
52	121	109.113	2.2	0.1
52	121	107.079	1.68	0.09
52	121	105.045	1.19	0.08
52	121	103.009	0.82	0.06
52	122	117.162	2.09	0.1
52	122	115.128	2.5	0.1
52	122	113.093	2.7	0.1
52	122	111.058	2.8	0.1
52	122	109.022	2.3	0.1
52	122	106.984	1.57	0.09
52	122	104.946	1.19	0.08
52	122	102.907	0.79	0.06

Table A.11: Differential cross sections for $Z = 52$ for E_{lab} =1200 MeV.

Z	θ_{lab}	A	d (fm)	CS/Ruth	error
1200	22	118	14.25	0.0007	0.0003
1200	23	118	14.31	0.0041	0.0007
1200	24	118	14.36	0.01	0.001
1200	25	118	14.42	0.0091	0.001
1200	26	118	14.49	0.015	0.001
1200	27	118	14.55	0.015	0.001
1200	28	118	14.62	0.022	0.001
1200	31	118	14.86	0.087	0.001
1200	32	118	14.94	0.135	0.002
1200	33	118	15.03	0.22	0.002
1200	34	118	15.13	0.3	0.002
1200	35	118	15.23	0.373	0.003
1200	36	118	15.33	0.436	0.003
1200	37	118	15.44	0.51	0.003
1200	38	118	15.56	0.551	0.003
1090	21	118	15.4	0.335	0.002
1090	22	118	15.46	0.564	0.003
1090	23	118	15.51	0.633	0.003
1090	24	118	15.58	0.517	0.003
1090	25	118	15.64	0.607	0.003
1090	26	118	15.71	0.514	0.003
1035	22.1	118	16.28	0.937	0.002
1035	23.1	118	16.35	1.099	0.003
1035	24.1	118	16.41	1.136	0.003
1035	25.1	118	16.48	0.796	0.002
1035	26.1	118	16.55	0.821	0.002
1035	27.1	118	16.63	0.741	0.002

Table A.12: Ratio of cross section over Rutherford cross section for (0n) channel.

Z	A	θ_{lab}	DCS (mb/sr)	error (mb/sr)
50	116	21	20.3	0.5
50	116	22	23.4	0.5
50	116	23	23.7	0.5
50	116	24	28.1	0.6
50	116	25	21.3	0.5
50	116	26	16.7	0.5
50	117	21	61.4	0.9
50	117	22	81	1
50	117	23	74.6	1
50	117	24	81	1
50	117	25	76.4	1
50	117	26	53.4	0.8
50	119	21	91	1
50	119	22	129	1
50	119	23	170	1
50	119	24	124	1
50	119	25	127	1
50	119	26	115	1
50	120	21	43.8	0.7
50	120	22	46.4	0.8
50	120	23	58.7	0.9
50	120	24	50.3	0.8
50	120	25	31.9	0.6
50	120	26	31.1	0.6

Table A.13: Differential cross sections for $Z = 50$ for E_{lab} =1090 MeV.

Z	A	θ_{cm}	DCS (mb/sr)	error (mb/sr)
50	116	22.1	7.4	0.2
50	116	23.1	7.5	0.2
50	116	24.1	6.4	0.2
50	116	25.1	6.4	0.2
50	116	26.1	4.8	0.2
50	116	27.1	3.7	0.1
50	117	22.1	35.7	0.4
50	117	23.1	37	0.4
50	117	24.1	33.8	0.4
50	117	25.1	31.5	0.4
50	117	26.1	29.6	0.4
50	117	27.1	19.8	0.3
50	119	22.1	70.9	0.6
50	119	23.1	76.1	0.6
50	119	24.1	74.6	0.6
50	119	25.1	52.6	0.5
50	119	26.1	50.2	0.5
50	119	27.1	48.3	0.5
50	120	22.1	9.5	0.2
50	120	23.1	8.6	0.2
50	120	24.1	8.9	0.2
50	120	25.1	8.8	0.2
50	120	26.1	6.6	0.2
50	120	27.1	5.1	0.2

Table A.14: Differential cross sections for $Z = 50$ for E_{lab} =1035 MeV.

A.2 Total cross sections (TCS)

Z	A	TCS (mb)	error (mb)	Z	A	TCS (mb)	error (mb)
47	108	2.0	0.5	49	117	47	2
47	109	2.8	0.6	49	118	31	2
47	110	3.6	0.6	49	119	11	1
47	111	4.4	0.7	50	116	42	4
47	112	4.6	0.7	50	117	130	20
47	113	3.4	0.6	50	119	190	50
47	114	1.7	0.4	50	120	60	10
48	110	4.2	0.7	51	116	12	1
48	111	5.6	0.8	51	117	32	2
48	112	10	1	51	119	38	2
48	113	14	1	51	120	28	2
48	114	17	1	51	121	21	2
48	115	15	1	51	122	9	1
48	116	10	1	51	123	4.5	0.7
48	117	5.4	0.8	52	118	3.0	0.6
48	118	2.2	0.5	52	119	4.6	0.7
49	112	6.4	0.8	52	120	6.3	0.8
49	113	12	1	52	121	7.8	0.9
49	114	22	2	52	122	7.6	0.9
49	115	37	2	52	123	5.3	0.8
49	116	43	2	52	124	2.7	0.5

Table A.15: TCS for E_{lab} =1200 MeV.

A.3 Transfer probabilities

Z	A	E_{lab}	θ_{lab} (°)	d	P_{tr}	error
50	116	1200	31	14.86	0.28	0.01
50	116	1200	32	14.94	0.274	0.008
50	116	1200	33	15.03	0.181	0.005
50	116	1200	34	15.13	0.136	0.003
50	116	1200	35	15.23	0.121	0.003
50	116	1200	36	15.33	0.097	0.002
50	116	1200	37	15.44	0.071	0.002
50	116	1200	38	15.56	0.064	0.001
50	116	1090	21	15.40	0.088	0.002
50	116	1090	22	15.46	0.059	0.001
50	116	1090	23	15.51	0.052	0.001
50	116	1090	24	15.58	0.074	0.002
50	116	1090	25	15.64	0.047	0.001
50	116	1090	26	15.71	0.042	0.001
50	116	1035	22.1	16.28	0.01	0.0003
50	116	1035	23.1	16.35	0.0085	0.0002
50	116	1035	24.1	16.41	0.0069	0.0002
50	116	1035	25.1	16.48	0.0095	0.0003
50	116	1035	26.1	16.55	0.0068	0.0002
50	116	1035	27.1	16.63	0.0057	0.0002

Table A.16: Transfer probabilities for (-2n).

Z	A	E_{lab}	θ_{lab} (°)	d	P_{tr}	error
50	117	1200	31	14.86	0.55	0.01
50	117	1200	32	14.94	0.6	0.01
50	117	1200	33	15.03	0.44	0.008
50	117	1200	34	15.13	0.34	0.006
50	117	1200	35	15.23	0.32	0.005
50	117	1200	36	15.33	0.293	0.004
50	117	1200	37	15.44	0.23	0.003
50	117	1200	38	15.56	0.216	0.003
50	117	1090	21	15.40	0.266	0.004
50	117	1090	22	15.46	0.204	0.003
50	117	1090	23	15.51	0.164	0.002
50	117	1090	24	15.58	0.213	0.003
50	117	1090	25	15.64	0.167	0.002
50	117	1090	26	15.71	0.134	0.002
50	117	1035	22.1	16.28	0.0486	0.0006
50	117	1035	23.1	16.35	0.042	0.0005
50	117	1035	24.1	16.41	0.0363	0.0004
50	117	1035	25.1	16.48	0.0471	0.0006
50	117	1035	26.1	16.55	0.0419	0.0006
50	117	1035	27.1	16.63	0.0303	0.0005

Table A.17: Transfer probabilities for (-1n).

Z	A	E_{lab}	θ_{lab} (°)	d	P_{tr}	error
50	119	1200	31	14.86	0.72	0.02
50	119	1200	32	14.94	0.67	0.01
50	119	1200	33	15.03	0.577	0.009
50	119	1200	34	15.13	0.552	0.008
50	119	1200	35	15.23	0.554	0.007
50	119	1200	36	15.33	0.494	0.006
50	119	1200	37	15.44	0.426	0.005
50	119	1200	38	15.56	0.359	0.004
50	119	1090	21	15.40	0.395	0.005
50	119	1090	22	15.46	0.323	0.004
50	119	1090	23	15.51	0.372	0.004
50	119	1090	24	15.58	0.326	0.004
50	119	1090	25	15.64	0.277	0.003
50	119	1090	26	15.71	0.29	0.003
50	119	1035	22.1	16.28	0.0966	0.0008
50	119	1035	23.1	16.35	0.0865	0.0007
50	119	1035	24.1	16.41	0.0802	0.0007
50	119	1035	25.1	16.48	0.0787	0.0008
50	119	1035	26.1	16.55	0.0711	0.0007
50	119	1035	27.1	16.63	0.0738	0.0008

Table A.18: Transfer probabilities for (+1n).

Z	A	E_{lab}	θ_{lab} (°)	d	P_{tr}	error
50	120	1200	31	14.86	0.36	0.01
50	120	1200	32	14.94	0.311	0.008
50	120	1200	33	15.03	0.248	0.005
50	120	1200	34	15.13	0.224	0.004
50	120	1200	35	15.23	0.229	0.004
50	120	1200	36	15.33	0.181	0.003
50	120	1200	37	15.44	0.139	0.002
50	120	1200	38	15.56	0.105	0.002
50	120	1200	24.5	14.39	0.44	0.07
50	120	1090	21	15.4	0.19	0.003
50	120	1090	22	15.46	0.117	0.002
50	120	1090	23	15.51	0.129	0.002
50	120	1090	24	15.58	0.132	0.002
50	120	1090	25	15.64	0.07	0.001
50	120	1090	26	15.71	0.078	0.002
50	120	1035	22.1	16.28	0.0129	0.0003
50	120	1035	23.1	16.35	0.0098	0.0002
50	120	1035	24.1	16.41	0.0096	0.0002
50	120	1035	25.1	16.48	0.0132	0.0003
50	120	1035	26.1	16.55	0.0093	0.0003
50	120	1035	27.1	16.63	0.0078	0.0002

Table A.19: Transfer probabilities for (+2n).

Z	A	E_{lab}	θ_{lab} (°)	d	P_{tr}	error
48	116	1090	21	15.4015	0.013	0.0008
48	116	1090	22	15.4565	0.0088	0.0005
48	116	1090	23	15.5147	0.0063	0.0004
48	116	1090	24	15.5762	0.0051	0.0004
48	116	1090	25	15.6412	0.0026	0.0003
48	116	1090	26	15.7098	0.0026	0.0003
48	116	1200	31	14.8576	0.113	0.006
48	116	1200	32	14.9436	0.102	0.004
48	116	1200	33	15.034	0.065	0.003
48	116	1200	34	15.129	0.047	0.002
48	116	1200	35	15.2288	0.037	0.001
48	116	1200	36	15.3337	0.026	0.001
48	116	1200	37	15.4439	0.0163	0.0008
48	116	1200	38	15.5597	0.0104	0.0006

Table A.20: Transfer probabilities for (-2p).

Z	A	E_{lab}	θ_{lab} (°)	d	P_{tr}	error
49	117	1090	21	15.4015	0.102	0.002
49	117	1090	22	15.4565	0.061	0.001
49	117	1090	23	15.5147	0.047	0.001
49	117	1090	24	15.5762	0.054	0.001
49	117	1090	25	15.6412	0.0322	0.001
49	117	1090	26	15.7098	0.0268	0.0009
49	117	1200	31	14.8576	0.43	0.01
49	117	1200	32	14.9436	0.382	0.009
49	117	1200	33	15.034	0.292	0.006
49	117	1200	34	15.129	0.212	0.004
49	117	1200	35	15.2288	0.178	0.003
49	117	1200	36	15.3337	0.13	0.003
49	117	1200	37	15.4439	0.082	0.002
49	117	1200	38	15.5597	0.061	0.001

Table A.21: Transfer probabilities for (-1p).

Z	A	E_{lab}	θ_{lab} (°)	d	P_{tr}	error
51	119	1090	21	15.4015	0.038	0.001
51	119	1090	22	15.4565	0.04	0.001
51	119	1090	23	15.5147	0.0327	0.001
51	119	1090	24	15.5762	0.0159	0.0007
51	119	1090	25	15.6412	0.0132	0.0006
51	119	1090	26	15.7098	0.0165	0.0007
51	119	1200	31	14.8576	0.39	0.01
51	119	1200	32	14.9436	0.346	0.009
51	119	1200	33	15.034	0.241	0.005
51	119	1200	34	15.129	0.163	0.004
51	119	1200	35	15.2288	0.137	0.003
51	119	1200	36	15.3337	0.084	0.002
51	119	1200	37	15.4439	0.064	0.002
51	119	1200	38	15.5597	0.042	0.001

Table A.22: Transfer probabilities for (+1p).

Z	A	E_{lab}	θ_{lab} (°)	d	P_{tr}	error
52	120	1090	21	15.4015	0.0015	0.0003
52	120	1090	22	15.4565	0.0006	0.0001
52	120	1090	23	15.5147	0.00036	0.0001
52	120	1090	24	15.5762	0.0004	0.0001
52	120	1090	25	15.6412	0.00035	0.0001
52	120	1090	26	15.7098	9e-05	5e-05
52	120	1200	31	14.8576	0.095	0.005
52	120	1200	32	14.9436	0.073	0.004
52	120	1200	33	15.034	0.045	0.002
52	120	1200	34	15.129	0.03	0.001
52	120	1200	35	15.2288	0.0176	0.001
52	120	1200	36	15.3337	0.0122	0.0007
52	120	1200	37	15.4439	0.006	0.0005
52	120	1200	38	15.5597	0.0037	0.0003

Table A.23: Transfer probabilities for (+2p).

Bibliography

[1] J. Wilczyński. Nuclear molecules and nuclear friction. *Physics Letters B*, 47:448, 1973.

[2] L. Corradi et al. Multinucleon transfer processes in ^{64}Ni+^{238}U. *Physical Review C*, 59:261, 1999.

[3] T. Mijatović et. al. Multinucleon transfer reactions in the ^{40}Ar+^{208}Pb system. *Physical Review C*, 94:064616, 2016.

[4] KE Rehm, AM van den Berg, JJ Kolata, DG Kovar, W Kutschera, G Rosner, GSF Stephans, and JL Yntema. Transition from quasi-elastic to deep-inelastic reactions in the ^{48}Ti+ ^{208} Pb system. *Physical Review C*, 37(6):2629, 1988.

[5] A Gobbi and W Nörenberg. Heavy ion collisions, 1980.

[6] WU Schroder and JR Huizenga. Damped heavy-ion collisions. *Annual Review of Nuclear Science*, 27(1):465–547, 1977.

[7] F. Galtarossa et al. Mass correlation between light and heavy reaction products in multinucleon transfer ^{197}Au+^{130}Te collisions. *Physical Review C*, 97:054606, 2018.

[8] P. Čolović et al. Stretched configuration of states as inferred from γ-ray angular distributions in ^{40}Ar+^{208}Pb neutron transfer reactions. *European Physical Journal A*, 53:166, 2017.

[9] G. Pollarolo. Personal pages. `http://personalpages.to.infn.it/~nanni/grazing/`.

[10] L. Corradi et al. Light and heavy transfer products in ^{58}Ni+^{208}Pb at the coulomb barrier. *Physical Review C*, 66:024606, 2002.

[11] Lorenzo Corradi and Giovanni Pollarolo. Facilities and methods: Recent achievements in multinucleon transfer reaction studies at lnl. *Nuclear Physics News*, 15(4): 23–27, 2005.

[12] L. Corradi, G. Pollarolo and S. Szilner. Multinucleon transfer processes in heavy-ion reactions. *Journal of Physics G: Nuclear and Particle Physics*, 36(11):113101, 2009.

[13] A. Winther. Dissipation, polarization and fluctuation in grazing heavy-ion collisions and the boundary to the chaotic regime. *Nuclear Physics A*, 594 (2):pg.203–245, 1995.

[14] A. Winther. Grazing reactions in collisions between heavy nuclei. *Nuclear Physics A*, 572 (1):pg.191–235, 1994.

[15] H. Esbensen, C. L. Jiang, and K. E. Rehm. Coupled-channels analysis of ^{58}Ni+^{124}Sn reactions. *Physical Review C*, 57(5):2401, May 1998.

[16] C. L. Jiang and et al. Multineutron transfer in ^{58}Ni+^{124}Sn collisions at sub-barrier energies. *Physical Review C*, 57(5):2393, May 1998.

[17] J. Knoll and R. Schaeffer. Extended seminar on nuclear physics. ICTP, Heavy-Ion, High-Spin States and Nuclear Structure, 1973.

[18] S. Szilner et al. Multinucleon transfer processes in ^{40}Ca+^{208}Pb. *Physical Review C*, 71: 044610, 2009.

[19] L. Corradi, A. M. Stefanini, D. Ackermann, S. Beghini, G. Montagnoli, C. Petrache, F. Scarlassara, C. H. Dasso, G. Pollarolo, and A. Winther. Multinucleon transfer reactions in ^{32}S+^{208}Pb close to the coulomb barrier. *Physical Review C*, 49(6):R2875, 1994.

[20] Enrico Vigezzi and Aage Winther. On the application of complex trajectories to direct heavy-ion reactions. *Annals of Physics*, 192(2):432–486, 1989. ISSN 0003-4916. doi: https://doi.org/10.1016/0003-4916(89)90145-0. URL `https://www.sciencedirect.com/science/article/pii/0003491689901450`.

[21] Ricardo A. Broglia and Aage Winther. *Heavy ion reactions*. Addison-Wesley Publishing Company, 1991.

[22] R. A. Broglia, G. Pollarolo, and A. Winther. On the absorptive potential in heavy ion scattering. *Nuclear Physics A*, 361(1):307–325, 1981.

[23] G. Pollarolo, R. A. Broglia, and A. Winther. Calculation of the imaginary part of the heavy ion potential. *Nuclear Physics A*, 406(2):369–389, 1983.

[24] C. Simenel. Particle transfer reactions with the time-dependent hartree-fock theory using a particle number projection technique. *Physical Review Letters*, 105(19): 192701, 2010. doi: 10.1103/PhysRevLett.105.192701.

[25] K. Sekizawa and K. Yabana. Time-dependent hartree-fock calculations for multinucleon transfer processes in ^{40,48} Ca + ^{124} Sn, ^{40} Ca + ^{208} Pb, and ^{58} Ni + ^{208} Pb reactions. *Physical Review C*, 88(1):014614, 2013. doi: 10.1103/PhysRevC.88.014614.

[26] G. Scamps and D. Lacroix. Effect of pairing on one- and two-nucleon transfer below the coulomb barrier: a time-dependent microscopic description. *Physical Review C*, 87(1):014605, 2013. doi: 10.1103/PhysRevC.87.014605.

[27] Z. Wu and L. Guo. Microscopic studies of production cross sections in multinucleon transfer reaction ^{58}Ni + ^{124}Sn. *Physical Review C*, 100(1):014612, 2019. doi: 10.1103/PhysRevC.100.014612.

[28] Kazuyuki Sekizawa. Microscopic description of production cross sections including deexcitation effects. *Physical Review C*, 96:014615, 07 2017. doi: 10.1103/PhysRevC.96.014615.

[29] V. I. Zagrebaev and W. Greiner. Unified consideration of deep inelastic, quasi-fission and fusion–fission phenomena. *Journal of Physics G: Nuclear and Particle Physics*, 31(7):825, 2005.

[30] V. I. Zagrebaev, Yu. Ts. Oganessian, M. G. Itkis, and W. Greiner. Superheavy nuclei and quasi-atoms produced in collisions of transuranium ions. *Physical Review C*, 73 (3):031602, 2006.

[31] V. I. Zagrebaev and W. Greiner. Shell effects in damped collisions: a new way to superheavies. *Journal of Physics G: Nuclear and Particle Physics*, 34(11):2265, 2007.

[32] V. I. Zagrebaev and W. Greiner. Production of new heavy isotopes in low-energy multinucleon transfer reactions. *Physical Review Letters*, 101:122701, 2008.

[33] V. I. Zagrebaev and W. Greiner. Synthesis of superheavy nuclei: A search for new production reactions. *Physical Review C*, 78(3):034610, 2008.

[34] V. I. Zagrebaev and W. Greiner. Production of heavy and superheavy neutron-rich nuclei in transfer reactions. *Physical Review C*, 83(4):044618, 2011.

[35] J. Tian, X. Wu, K. Zhao, Y. Zhang, and Z. Li. Properties of the composite systems formed in the reactions of ^{238} U+ ^{238} U and 232 th+ 250 cf. *Physical Review C*, 77 (6):064603, 2008.

[36] K. Zhao, Z. Li, X. Wu, and Y. Zhang. Production probability of superheavy fragments at various initial deformations and orientations in the ^{238} U+ ^{238} U reaction. *Physical Review C*, 88(4):044605, 2013.

[37] K. Zhao, Z. Li, N. Wang, Y. Zhang, Q. Li, Y. Wang, and X. Wu. Production mechanism of neutron-rich transuranium nuclei in ^{238} U+ ^{238} U collisions at near-barrier energies. *Physical Review C*, 92(2):024613, 2015.

[38] V. V. Volkov. Deep inelastic transfers and complete fusion of complex nuclei. the new approach to the process of nuclear fusion. *Izv. Akad. Nauk SSSR, Ser. Fiz*, 50: 1879, 1986.

[39] Z.-Q. Feng, G.-M. Jin, and J.-Q. Li. Production of heavy isotopes in transfer reactions by collisions of ^{238} U+ ^{238} U. *Physical Review C*, 80(6):067601, 2009.

[40] L. Zhu, Z.-Q. Feng, and F.-S. Zhang. Production of heavy neutron-rich nuclei in transfer reactions within the dinuclear system model. *Journal of Physics G: Nuclear and Particle Physics*, 42(8):085102, 2015.

[41] M.-H. Mun, G. G. Adamian, N. V. Antonenko, Y. Oh, and Y. Kim. Production cross section of neutron-rich isotopes with radioactive and stable beams. *Physical Review C*, 89(3):034622, 2014.

[42] M.-H. Mun, G. G. Adamian, N. V. Antonenko, Y. Oh, and Y. Kim. Toward neutron-rich nuclei via transfer reactions with stable and radioactive beams. *Physical Review C*, 91(5):054610, 2015.

[43] N. V. Antonenko, E. A. Cherepanov, A. K. Nasirov, V. P. Permjakov, and V. V. Volkov. Compound nucleus formation in reactions between massive nuclei: Fusion barrier. *Physical Review C*, 51(5):2635, 1995.

[44] G. G. Adamian, N. V. Antonenko, and W. Scheid. Model of competition between fusion and quasifission in reactions with heavy nuclei. *Nuclear Physics A*, 618(1): 176–198, 1997.

[45] G. G. Adamian, N. V. Antonenko, W. Scheid, and V. V. Volkov. Treatment of competition between complete fusion and quasifission in collisions of heavy nuclei. *Nuclear Physics A*, 627(2):361–378, 1997.

[46] G. G. Adamian, N. V. Antonenko, W. Scheid, and V. V. Volkov. Fusion cross sections for superheavy nuclei in the dinuclear system concept. *Nuclear Physics A*, 633(3): 409–420, 1998.

[47] G. G. Adamian, N. V. Antonenko, and W. Scheid. Characteristics of quasifission products within the dinuclear system model. *Physical Review C*, 68(3):034601, 2003.

[48] C. Li, F. Zhang, J. Li, L. Zhu, J. Tian, and N. Wang. Multinucleon transfer in the ^{136}Xe+ ^{208}Pb reaction. *Physical Review C*, 93(1):014618, 2016. doi: 10.1103/PhysRevC.93.014618.

[49] C. Li, P. Wen, J. Li, G. Zhang, B. Li, and X. Xu. Production mechanism of new neutron-rich heavy nuclei in the ^{136}Xe+ ^{208}Pb reaction. *Physics Letters B*, 776: 278–283, 2018. doi: 10.1016/j.physletb.2017.11.060.

[50] C. Li, X. Xu, J. Li, G. Zhang, B. Li, and C. A. T. Sokhna. Production of new neutron-rich heavy nuclei with z = 56-80 in the multinucleon transfer reactions of ^{136}Xe+ ^{198}Pt. *Physical Review C*, 99(2):024602, 2019. doi: 10.1103/PhysRevC.99.024602.

[51] Y. X. Zhang, N. Wang, Q. F. Li, L. Ou, J. L. Tian, and M. Liu. Progress of quantum molecular dynamics model and its applications in heavy ion collisions. *Frontiers of Physics*, 15(5):54301, 2020. doi: 10.1007/s11467-020-0961-9.

[52] C. Li, J. Tian, and F. S. Zhang. Production mechanism of the neutron-rich nuclei in multinucleon transfer reactions: A reaction time scale analysis in energy dissipation process. *Physics Letters B*, 809:135697, 2020. doi: 10.1016/j.physletb.2020.135697.

[53] G. Audi, M. Wang, A. H. Wapstra, F. G. Kondev, M. MacCormick, X. Xu, and B. Pfeiffer. Nuclear data sheets for a = 252. *Chinese Physics C*, 36(12):1287–1603, 2012. doi: 10.1088/1674-1137/36/12/003.

[54] B. Ishkhanov, M. Stepanov, and Tatiana Tretyakova. Nucleon pairing in atomic nuclei. *Moscow University Physics Bulletin*, 69(1):10–19, 2013. doi: 10.3103/S0027134914010068.

[55] A. Richter. Personal pages. `http://www.phys.ens.fr/cours/Sandro/04-04-05/richter.pdf`.

[56] W. von Oertzen and A. Vitturi. Pairing correlations of nucleons and multi-nucleon transfer between heavy nuclei. *Reports on Progress in Physics*, 64:pg. 1247–1337, 2001.

[57] D.M. Brink and R.A. Broglia. *Nuclear superfluidity: pairing in finite systems*. Cambridge University Press, UK, 2005.

[58] R. Broglia and V. Zelevinsky. *Fifty years of nuclear BCS - pairing in finite systems*. World Scientific, USA, 2013.

[59] G. Potel Aguilar and R.A. Broglia. *The nuclear cooper pair: Structure and reactions*. Cambridge University Press, Cambridge, 2021. doi: 10.1017/9781108919036.

[60] R. A. Broglia and et al. Proc. 39th int. winter meeting, bormio. In I. Iori and A. Moroni, editors, *Supplemento 117*, page 390. Univ. di Milano, 2001.

[61] L. J. B. Goldfarb and W. von Oertzen. *Heavy Ion Collisions*, volume 1. North-Holland, Amsterdam, 1980.

[62] R. A. Broglia, O. Hansen, and C. Riedel. *Advances in Nuclear Physics*, volume 6, page 287. Plenum, New York, 1973.

[63] R.A. Broglia, G Pollarolo, and Aa Winther. On the absorptive potential in heavy ion scattering. *Nuclear Physics A*, 361(1):307–325, 1981.

[64] F. W. N. de Boer and et al. Nucleon transfer reactions to rotational states induced by ^{206,208}Pb projectiles. *Z. Phys. A*, 325:457, 1986.

[65] T. Haertlein and et al. Selecting cold 2n transfer in ^{162}Dy (^{116}Sn,^{118}Sn)^{160}Dy,. *Eur. Phys. J. A*, 4:41, 1999.

[66] K. G. Helmer and et al. Search for diabolical pair transfer in two-neutron transfer reactions. *Phys. Rev. C*, 48:1879, 1993.

[67] W. J. Kernan and et al. Heavy-ion induced transfer reactions with spherical and deformed nuclei. *Nucl. Phys. A*, 524:344, 1991.

[68] A. O. Machiavelli and et al. *Nucl. Phys. A*, 432:436, 1985.

[69] S. J. Sanders and et al. Quasielastic transfer in the ^{136}Xe + ^{64Ni} reaction. *Phys. Rev. C*, 55:2541, 1997.

[70] G. Himmele and et al. Measurement of nuclear reaction cross sections for ^{183}W, ^{184}W, ^{238}U near the interaction barrier. *Nucl. Phys. A*, 404:401, 1983.

[71] T. Tamura, T. Udagawa, and M. Mermaz. Direct reaction analyses of heavy-ion induced reactions leading to discrete states. *Phys. Rep. C*, 65:345, 1980.

[72] I. Peter and et al. Strong enhancement of two-neutron transfer in the system ^{206} Pb+ ^{118} Sn. *Eur. Phys. J. A*, 4:313, 1999.

[73] W. von Oertzen and et al. Quasi-elastic neutron transfer and pairing effects in the interaction of heavy nuclei. *Z. Phys. A*, 326:463, 1987.

[74] L. Corradi et al. Single and pair neutron transfers at sub-barrier energies. *Physical Review C*, 84:034603, 2011.

[75] D. Montanari et al. Neutron pair transfer in ^{60}Ni+^{116}Sn far below the coulomb barrier. *Physical Review Letters*, 113:052501, 2014.

[76] D. Montanari et al. Pair neutron transfer in ^{60}Ni+^{116}Sn probed via γ-particle coincidences. *Physical Review C*, 93:054623, 2016.

[77] G. Potel, F. Barranco, E. Vigezzi, and R.A. Broglia. Quantum entanglement in nuclear cooper-pair tunneling with γ rays. *Physical Review C*, 103:L021601, 2021. doi: 10.1103/PhysRevC.103.L021601.

[78] S. Szilner et al. Multinucleon transfer reactions in closed-shell nuclei. *Physical Review C*, 76:024604, 2007.

[79] I. Peter, W.von Oertzen, and H. Bohlen. Strong enhancement of two-neutron transfer in the system ^{206}Pb+^{118}Sn. *Eur. Phys. J. A*, 4:313–317, 1999. doi: 10.1007/s100500050236. URL `https://doi.org/10.1007/s100500050236`.

[80] I. Peter, W. von Oertzen, S. Thummerer, H.G. Bohlen, B. Gebauer, J. Gerl, M. Kaspar, I. Kozhoukharov, T. Kröll, M. Rejmund, H.J. Wollersheim, and I.J. Thompson. Enhanced neutron pair transfer and collective excitations in the system ^{206}Pb + ^{118}Sn at barrier energies. *Eur. Phys. J. A*, 16:509–525, 2003. doi: 10.1140/epja/i2002-10124-7.

[81] W. von Oertzen, I. Peter, and S. et al. Thummerer. Selection of cold transfer and enhanced neutron-pair transfer in the ^{206}Pb + ^{118}Sn reaction. *Eur. Phys. J. A*, 20: 153–156, 2003. doi: 10.1140/epja/i2002-10342-y. URL `https://doi.org/10.1140/epja/i2002-10342-y`.

[82] W. von Oertzen and J. Speer. Four-nucleon and alpha-particle transfer between heavy nuclei. *J. Phys. G: Nucl. Part. Phys.*, 18:1773, 1992.

[83] G. Potel et al. Cooper pair transfer in nuclei. *Reports on Progress in Physics*, 76 (10):106301, 2013.

[84] P. Ring and P. Schuck. *The Nuclear Many-Body Problem.* Springer, 2004.

[85] A. Ravlić. *Stellar weak interaction processes at finite temperature based on the relativistic energy density functional theory.* PhD thesis, University of Zagreb, 2023.

[86] A. Gadea et al. The CLARA-PRISMA setup installed at LNL: first results. *Journal of Physics G: Nuclear and Particle Physics*, 31:S1443, 2005.

[87] G. Montagnoli, A. M. Stefanini, M. Trotta, S. Beghini, M. Bettini, F. Scarlassara, V. Schiavon, L. Corradi, B. R. Behera, E. Fioretto, A. Gadea, A. Latina, S. Szilner, L. Donà, M. Rigato, N. A. Kondratiev, A. Yu. Chizhov, G. Kniajeva, E. M. Kozulin, I. V. Pokrovskiy, V. M. Voskressensky, and D. Ackermann. The large-area micro-channel plate entrance detector of the heavy-ion magnetic spectrometer

PRISMA. *Nuclear Instruments and Methods in Physics Research Section A: Accelerators, Spectrometers, Detectors and Associated Equipment*, 547(2):455–463, 2005. doi: 10.1016/j.nima.2005.05.080.

[88] S. Beghini, L. Corradi, E. Fioretto, A. Gadea, A. Latina, G. Montagnoli, F. Scarlassara, A. M. Stefanini, S. Szilner, M. Trotta, and A. M. Vinodkumar. The focal plane detector of the magnetic spectrometer PRISMA. *Nuclear Instruments and Methods in Physics Research Section A: Accelerators, Spectrometers, Detectors and Associated Equipment*, 551(2):364–374, 2005. doi: 10.1016/j.nima.2005.06.143.

[89] A. Utepov. Multinucleon transfer reactions in the ^{206}Pb+^{118}Sn system studied with the prisma spectrometer. Master's thesis, University of Padua, 2019.

[90] Andrea Latina. *Study of Heavy-Ion Reactions with the Magnetic Spectrometer PRISMA: On-line and Off-line Data Analysis*. PhD thesis, University of Turin, 2004.

[91] K. Shima et al. Empirical formula for the average equilibrium charge-state of heavy ions behind various foils. *Nuclear Instruments and Methods in Physics Research*, 200: 605–608, 1982.

[92] J. Diklić, S. Szilner, L. Corradi, T. Mijatović, G. Pollarolo, P. Čolović, G. Colucci, E. Fioretto, F. Galtarossa, A. Goasduff, A. Gottardo, J. Grebosz, A. Illana, G. Jaworski, M. Jurado Gomez, T. Marchi, D. Mengoni, G. Montagnoli, D. Nurkić, M. Siciliano, N. Soić, A. M. Stefanini, D. Testov, J. J. Valiente-Dobón, and N. Vukman. Transfer reactions in ^{206}Pb + ^{118} Sn: From quasielastic to deep-inelastic processes. *Phys. Rev. C*, 107:014619, Jan 2023. doi: 10.1103/PhysRevC.107.014619. URL `https://link.aps.org/doi/10.1103/PhysRevC.107.014619`.

[93] D. Montanari et al. Response function of the magnetic spectrometer prisma. *Eur. Phys. J. A*, 47 (4):, 2011.

[94] T.Mijatović et al. Study of the cross section determination with the PRISMA spectrometer: The ^{40}Ar + ^{208}Pb case. *Eur. Phys. J. A*, 52 (113):, 2016.

[95] L. Corradi, S.J. Skorka, U. Lenz, et al. Near-barrier transfer and fusion of the systems ^{33}S + ^{90,91,92} Zr. *Z. Physik A - Atomic Nuclei*, 335:55–72, 1990. doi: 10.1007/BF01289348.

[96] J. Speer, W. von Oertzen, D. Schüll, M. Wilpert, H.G. Bohlen, B. Gebauer, B. Kohlmeyer, and F. Pühlhofer. Cold multi-proton-pair transfer between ^{144}Sm and ^{208}Pb. *Phys. Lett. B*, 259:422, 1991.

[97] R Künkel, W von Oertzen, HG Bohlen, B Gebauer, HA Bösser, B Kohlmeyer, J Speer, F Pühlhofer, and D Schüll. Pairing effects in nucleon transfer reactions in the system ^{144}Sm + ^{88}Sr at 4.7 MeV/u. *Eur. Phys. J. A*, 336:71–89, 1991.

[98] JJ Valiente-Dobón, R Menegazzo, A Goasduff, D Agguiaro, P Aguilera, F Angelini, M Balogh, D Bazzacco, J Benito, G Benzoni, et al. Conceptual design of the agata 2π array at lnl. *Nuclear Instruments and Methods in Physics Research Section A: Accelerators, Spectrometers, Detectors and Associated Equipment*, 1049:168040, 2023.

List of Figures

List of Tables

Acknowledgements

I would like to express my deepest thanks to Dr. Suzana Szilner, my research supervisor, for her true dedication and invaluable guidance throughout our research work.
I am profoundly grateful to Dr. Lorenzo Corradi for all I have learned form him, and for his insightful suggestions and dedicated efforts in reviewing and enhancing this thesis.
My time at the Laboratori Nazionali di Legnaro was a unique experience, enriched by the inspiring environment and the warm welcome from the entire team. I am deeply appreciative of the opportunity to participate in numerous experiments, where I learned a lot but also had a great time.
I feel very grateful to my colleagues at of the Laboratory of nuclear physics at the Ruđer Bošković Institute, where I have met great physicists, and more importantly, great friends. Special thanks to Dr. Tea Mijatović and Dr. Petra Čolović for their assistance with ROOT and PRISMA data analysis, which significantly eased the start of my career. I am thankful to Prof. Matko Milin for his valuable discussions and advice on my thesis. My heartfelt appreciation goes to Nikola, Luka, Ivana, Margareta, Deša, and Igor for their personal support, kindness, and encouragement.
Lastly, I express my deepest gratitude to my fiancé, Neven, for his unwavering support and love.